

# Design and test of a 3D-printed horizontal axis wind turbine

Dissertation presented by  
**Pierrick IGOT, Charles SNYERS D'ATTENHOVEN**

for obtaining the Master's degree in  
**Electro-mechanical Engineering**

Supervisors  
**Philippe CHATELAIN, Bruno DEHEZ**

Reader(s)  
**Emmanuel DEJAEGER, Jeroen VAN BEECK**

Academic year 2015-2016



The von Karman Institute  
for Fluid Dynamics



# Contents

<b>List of Figures</b>	<b>7</b>
<b>List of Tables</b>	<b>9</b>
<b>List of Symbols</b>	<b>11</b>
<b>Abstract</b>	<b>15</b>
<b>1 Introduction</b>	<b>17</b>
1.1 Context . . . . .	17
1.2 Wind power . . . . .	18
1.3 State-of-the-art . . . . .	19
1.4 Objectives . . . . .	21
<b>2 From manufacturing constraints to specifications</b>	<b>23</b>
2.1 3D printing . . . . .	23
2.1.1 Printing process: fused deposition modeling . . . . .	23
2.1.2 Materials . . . . .	24
2.1.3 Printing parameters and limitations . . . . .	25
2.1.4 Available 3D printers . . . . .	26
2.2 Laser cutting . . . . .	27
2.3 Design specifications . . . . .	27
<b>3 Aerodynamical design</b>	<b>31</b>
3.1 Momentum theory . . . . .	31
3.1.1 Actuator disc (1-D analysis) . . . . .	31
3.1.2 Betz limit . . . . .	33
3.1.3 Breakdown of the momentum theory . . . . .	33
3.2 Blade Element Momentum method . . . . .	34
3.2.1 Definitions . . . . .	34
3.2.2 Rotor disc and blade elements (2-D analysis) . . . . .	34
3.2.3 Geometry of a blade element . . . . .	36
3.2.4 Aerodynamic forces and momentum conservation . . . . .	37
3.2.5 Tip and root losses . . . . .	37
3.2.6 High-thrust correction . . . . .	38
3.2.7 Residual function and guaranteed convergence algorithm . . . . .	39
3.2.8 Extension of the lift and drag coefficients' range . . . . .	40
3.2.9 Example of application . . . . .	40
3.3 Design of the blades . . . . .	42
3.3.1 Airfoil(s) . . . . .	42
3.3.2 Chord and twist distribution . . . . .	45

3.3.3	Number of blades optimization . . . . .	46
3.4	Numerical power prediction of the rotors . . . . .	48
3.4.1	Blade roots . . . . .	50
3.5	Yaw system: tail fin . . . . .	51
3.6	Diffuser augmented wind turbine . . . . .	51
<b>4</b>	<b>Generator design</b>	<b>53</b>
4.1	Off-the-shelf solution . . . . .	53
4.1.1	Characteristics . . . . .	54
4.1.2	Generator efficiency . . . . .	55
4.1.3	Generator thermal characteristic . . . . .	57
4.1.4	Planetary gearhead efficiency . . . . .	58
4.2	Ad-hoc solution . . . . .	58
4.2.1	Choice of generator type . . . . .	59
4.2.2	Number of windings/magnets . . . . .	63
4.2.3	Thermal model . . . . .	64
<b>5</b>	<b>Prototype design</b>	<b>73</b>
5.1	Main components . . . . .	73
5.2	Blades . . . . .	74
5.3	Hub . . . . .	77
5.3.1	F1: hub and blades . . . . .	77
5.3.2	F2: hub and generator . . . . .	80
5.3.3	F3: shape of the hub . . . . .	81
5.4	Nacelle . . . . .	82
5.4.1	F1 and F2: shape of the nacelle . . . . .	82
5.4.2	F3: nacelle and tower . . . . .	83
5.4.3	F4: nacelle and tail fin . . . . .	83
5.5	Power transmission system . . . . .	85
5.6	Duct . . . . .	85
5.7	Complete prototype . . . . .	85
<b>6</b>	<b>Tests</b>	<b>89</b>
6.1	Aerodynamical setup . . . . .	89
6.1.1	von Karman Institute: low speed wind tunnel L-1A . . . . .	90
6.1.2	Wind tunnel at Université Catholique de Louvain . . . . .	91
6.2	Electrical setup . . . . .	93
6.2.1	Rectifier . . . . .	93
6.2.2	Boost converter and load . . . . .	93
6.2.3	DSpace: PI regulator . . . . .	95
6.3	Methodology . . . . .	96
6.3.1	Wind velocity measurements . . . . .	96
6.3.2	Hub balancing . . . . .	96
6.4	Results . . . . .	97
6.4.1	Power coefficient . . . . .	97
6.4.2	Cut-in wind speed . . . . .	102
6.4.3	Generator temperature . . . . .	102
<b>7</b>	<b>Conclusion and perspectives</b>	<b>105</b>
7.1	Achievements . . . . .	105
7.2	Futur prospects . . . . .	106

**Appendices** **111**

**A Prototype design** **113**

    A.1 Nacelle and duct assembly . . . . . 113

**B Technical drawings** **115**

**C Tests** **131**

    C.1 Measuring instruments . . . . . 131

    C.2 Results at the von Karman Institute . . . . . 131

    C.3 Results at UCL LEFT . . . . . 133

    C.4 Wind speed measurements . . . . . 135



# List of Figures

- 1.1 Wind power capacity in the world [13] . . . . . 17
- 1.2 Example of power curve [49] . . . . . 19
  
- 2.1 Fused deposition modeling [53] . . . . . 24
- 2.2 Example of stress-strain diagram . . . . . 24
- 2.3 Fillings of 100%, 60% and 30% (from [50]) . . . . . 26
- 2.4 Wind power . . . . . 28
- 2.5 Wind distribution . . . . . 29
- 2.6 Power density . . . . . 30
  
- 3.1 Actuator disc and streamtube (from [10]) . . . . . 32
- 3.2 Rotor disc and tangential induced speed (seen in the  $e_x - e_\theta$  plane) . . . . . 34
- 3.3 Blade element (from [10]) . . . . . 35
- 3.4 Flow around a blade element . . . . . 36
- 3.5 Glauert and Buhl high thrust corrections . . . . . 39
- 3.6 Viterna and Corrigan lift and drag extrapolation . . . . . 41
- 3.7 BEM method: power, thrust and torque coefficients . . . . . 41
- 3.8 Laminar separation bubble (from [54]) . . . . . 43
- 3.9 NREL S833 airfoil family . . . . . 43
- 3.10 Selig and Giguere low Reynolds airfoil family . . . . . 44
- 3.11 Wortmann FX63-137 airfoil . . . . . 44
- 3.12 S834 lift-to-drag ratio and drag polar (data from [29]) . . . . . 45
- 3.13 SG6043 lift-to-drag ratio and drag polar (data from [44]) . . . . . 45
- 3.14 FX63 lift-to-drag ratio and drag polar (data from [29]) . . . . . 46
- 3.15 Optimal distribution of chord and twist: angle of attack and induction factor  
along the blade . . . . . 47
- 3.16 Twist and chord distributions . . . . . 47
- 3.17 S834: number of blades influence on power coefficient . . . . . 48
- 3.18 Designed rotors: prediction of power coefficient . . . . . 49
- 3.19 Designed rotors: prediction of power produced . . . . . 49
- 3.20 Shape of the blade roots (CAD file) . . . . . 50
- 3.21 Shape of the blade roots (prototype) . . . . . 50
- 3.22 Geometry of a delta wing tail fin [57] . . . . . 51
- 3.23 Diffuser augmented wind turbine (from [26]) . . . . . 52
  
- 4.1 Maxon BLDC motor: schematic representation . . . . . 54
- 4.2 Voltage in a BLDC motor [15] . . . . . 56
- 4.3 Approximation of the friction torque . . . . . 57
- 4.4 Thermal system . . . . . 58
- 4.5 Gearhead efficiency as a function of torque (schematic) [31] . . . . . 59
- 4.6 Types of PMSG . . . . . 60

4.7	Magnetic field for a given position . . . . .	61
4.8	Combinations slots-poles allowing balanced concentrated windings [37] . . . . .	64
4.9	Approximation by a cylinder (from [32]) . . . . .	65
4.10	Circuit of thermal resistances (from [32]) . . . . .	65
4.11	Simplified generator . . . . .	69
4.12	Circuit of thermal resistances . . . . .	70
5.1	Structure of a small wind turbine (from [1]) . . . . .	73
5.2	Blade assembly . . . . .	75
5.3	Rotation of the blade: <i>Solidworks</i> results . . . . .	77
5.4	Blade and hub assembly . . . . .	79
5.5	Assembly rule for bearings ([21]) . . . . .	81
5.6	Sketch of generator and hub assembly . . . . .	81
5.7	Shape of the hub . . . . .	82
5.8	Shape of the nacelle . . . . .	83
5.9	Tail fin and nacelle assembly . . . . .	84
5.10	Blade assembly . . . . .	86
5.11	Hub assembly (back view) . . . . .	86
5.12	Hub assembly (front view) . . . . .	86
5.13	Global assembly (lateral view) . . . . .	87
5.14	Global assembly (frontl view) . . . . .	87
6.1	Blockage effect in open and closed test sections (from [52]) . . . . .	89
6.2	Velocity profile in a wind tunnel (from [28]) . . . . .	90
6.3	Experimental setup at von Karman Institute . . . . .	92
6.4	Experimental setup at UCL LEFT . . . . .	92
6.5	Experimental setup diagram . . . . .	93
6.6	Three-phase passive rectifier [6] . . . . .	94
6.7	Influence of the capacitor [6] . . . . .	94
6.8	log-Tchebycheff method [34] . . . . .	96
6.9	Power coefficient of rotor 1 at UCL LEFT . . . . .	99
6.10	Power coefficient of rotor 2 at UCL LEFT . . . . .	99
6.11	Power coefficient of rotor 1 at VKI . . . . .	100
6.12	Power coefficient of rotor 2 at VKI . . . . .	100
A.1	Duct proposition #1 . . . . .	113
A.2	Duct proposition #2 . . . . .	114

# List of Tables

1.1	Examples of existing small wind turbines . . . . .	20
2.1	Properties of 3D printing materials . . . . .	25
2.2	3D printers at UCLouvain . . . . .	26
2.3	Wind turbine specifications . . . . .	30
3.1	Airfoil comparison . . . . .	45
4.1	Maxon BLDC EC-40 and planetary gearhead characteristics (from [14]) . . . . .	54
4.2	Rotors characteristics . . . . .	54
4.3	Comparison between slot and slotless generator . . . . .	62
4.4	Comparison between internal and external rotor . . . . .	62
4.5	Resolution of the windings sequence . . . . .	64
4.6	Thermal parameters . . . . .	69
4.7	Geometric parameters . . . . .	71
4.8	Simulation results . . . . .	71
5.1	Comparison of blades assemblies . . . . .	76
5.2	Rotation of the blade: <i>Solidworks</i> simulation parameters (partly from [11, 47]) . . . . .	76
5.3	Pros and cons of hub proposition #1 . . . . .	78
5.4	Pros and cons of hub proposition #2 . . . . .	78
5.5	Pros and cons of hub proposition #3 . . . . .	78
5.6	Comparison of 3 hub propositions . . . . .	79
5.7	Characteristics of planetary gearhead bearing . . . . .	80
5.8	Loads on tower bearing . . . . .	83
5.9	Comparison of power transmission devices . . . . .	85
6.1	VKI low speed wind tunnel L-1A: characteristics (from [23]) . . . . .	91
6.2	UCL LEFT wind tunnel: characteristics . . . . .	91
6.3	Position of measuring points for log-Tchebycheff method [34] . . . . .	96
6.4	Efficiency rotor1 . . . . .	98
6.5	Efficiency rotor2 . . . . .	101
6.6	Starting wind speed . . . . .	102
6.7	Results of temperature tests . . . . .	103
A.1	Comparison of duct designs . . . . .	114
C.1	Measuring instruments . . . . .	131



# List of Symbols

$a$	Axial induction factor	[-]
$a'$	Tangential induction factor	[-]
$A_R$	Rotor swept area	[ $m^2$ ]
$B_r$	Magnets remanence	[T]
$B$	Magnetic flux density	[T]
$BR$	Blockage ratio	[-]
$BF$	Blockage factor	[-]
$C$	Torque	[N]
$c$	Chord of the blade element; chord distribution	[-]
$c_p$	Mass heat capacity	[J/(kg K)]
$C_d$	Drag coefficient	[-]
$C_l$	Lift coefficient	[-]
$C_x$	Axial force coefficient	[-]
$C_y$	Tangential force coefficient	[-]
$C_P$	Power coefficient	[-]
$C_Q$	Torque coefficient	[-]
$C_T$	Thrust coefficient	[-]
$F$	Prandtl's loss factor	[-]
$h$	Heat transfer coefficient	[W/( $m^2$ )K]
$I$	Current	[A]

$J$	Current density	[A/m <sup>2</sup> ]
$k$	thermal conductivity	[W/(m K)]
$k_\phi$	Torque constant	[mNm/A]
$k(\phi)$ and $k'(\phi)$	Local blade element constants	[-]
$K_i$	Integral coefficient (PI regulator)	[-]
$K_p$	Proportional coefficient (PI regulator)	[-]
$L_{kj}$	Mutual inductance	[H]
$L_\delta$	Air gap axial length	[m]
$Nu$	Nusselt number	[-]
$p$	Number of poles pairs	[-]
$P_{cin}$	Available cinematic power of the wind	[-]
$P_{elec}$	Electrical Power	[W]
$P_{meca}$	Mechanical Power	[W]
$Q$	Mechanical torque of the rotor	[Nm]
$\dot{Q}$	Heat flux	[W]
$r$	Radius of the blade element	
$R$	Radius of the rotor	[m]
$\mathcal{R}$	Residual function	[-]
$Re$	Reynolds number	[-]
$R_{pp}$	Phase to phase resistance	[Ω]
$R_{th}$	Thermal resistance	[K/W]
$s$	Blade element solidity	[-]
$t$	Temperature	[°C]
$T$	Torque	[Nm]
$T$	Thrust at the rotor	[N]
$Ta$	Taylor number	[-]

$U$	Voltage	[V]
$v_x$	Axial induced speed	[m/s]
$V_0$	Free stream velocity	[m/s]
$V_F$	Wind speed in free stream conditions	[m/s]
$V_R$	Velocity at the rotor	[m/s]
$\vec{V}_t$	Total velocity at the blade element	[m/s]
$V_T$	Wind speed in wind tunnel conditions	[m/s]
$V_W$	Velocity of the wake	[m/s]
$W_{cmag}$	Magnetic co-energy	[W]
$W_{pp}$	Number of windings per pole and per phase	[-]
$\alpha$	Angle of attack of the blade element	[-]
$\beta$	Twist angle of the blade element; twist distribution	[-]
$\delta$	Air gap radial length	[m]
$\eta$	Efficiency	[-]
$\lambda$	Tip speed ratio	[-]
$\lambda_l$	Local tip speed ratio	[-]
$\mu$	Dynamic viscosity	[(Ns)/m <sup>2</sup> ]
$\nu$	Cinematic viscosity	[m <sup>2</sup> /s]
$\rho$	Air density	[kg/m <sup>3</sup> ]
$\Phi$	Magnetic flux	[Tm <sup>2</sup> ]
$\phi$	Inflow angle of the blade element	[-]
$\Omega$	Rotational speed of the rotor	[rpm]
$\omega$	Rotational speed	[rad/s]
$\omega_\theta$	Tangential induced rotational speed	[rad/s]



# Abstract

Rapid prototyping is becoming more and more available to everyone through the apparition of *fab labs* and *hackerspaces* in universities and big cities. Its main advantages are the speed of fabrication and the ease to share designs with other people. People have great expectations of 3D printing in particular. The main goal of our master's thesis was to prove that it can be used to build a whole working prototype such as a small wind turbine and to take advantage of this technology by designing parts differently. We achieved to build a 70cm rotor which produces up to 100W of power through a Maxon BLDC motor re-used as a generator. We developed a test bench with a variable load (through a Boost converter) to control the rotational speed of the wind turbine and study its aerodynamics. We found out that our design is quite efficient, with power coefficients up to 0,4. It was also very stable up to 900 rpm. Finally, we also theoretically developed tools to design a PMSG generator to be 3D printed, to replace the unadapted Maxon BLDC motor. However, we did not have the resources and the time to build it. The pre-design of this generator might be used in a future project about the 3D printing technology and the wind energy.



# Chapter 1

## Introduction

### 1.1 Context

Energy is a growing issue in the world. Most of the energy used in the world today comes from fossil fuels. The use of these resources has a huge impact on the environment through the gigantic production of carbon dioxide. Furthermore, they are not renewable and their cost will increase as they become rarer. Ideally, fossil energy sources should be replaced by energy sources both renewable and cost effective. Wind energy is a part of the solution to this issue. Indeed, since the 1970's and the first oil crisis, many research programs have studied wind turbines and developed the large three-bladed, horizontal axis wind turbine that we know today. This design has spread and the wind energy market is now booming (see Figure 1.1). However, most investments are made in very large scale projects, such as offshore wind farms. As a consequence the large diameter wind turbines are very efficient. Wind turbines of small diameter are not as technologically developed. For example, the shape of the blades of small wind turbines is often very simple (untwisted flat plate) compared to that of large wind turbines. Thus there is room for improvement. The main application of small scale wind power is off-grid electrification of rural areas. In Africa or India for instance, a large part of the population still lives in remote regions un-connected to the national grid. In those places, it is more economically interesting to produce power close to each load with several small machines than to produce a lot of power in one place and develop infrastructures to transmit energy over a very large distance. Small wind turbines can be a solution in this case. It is then useful to carry on research to improve the design of small wind turbines.

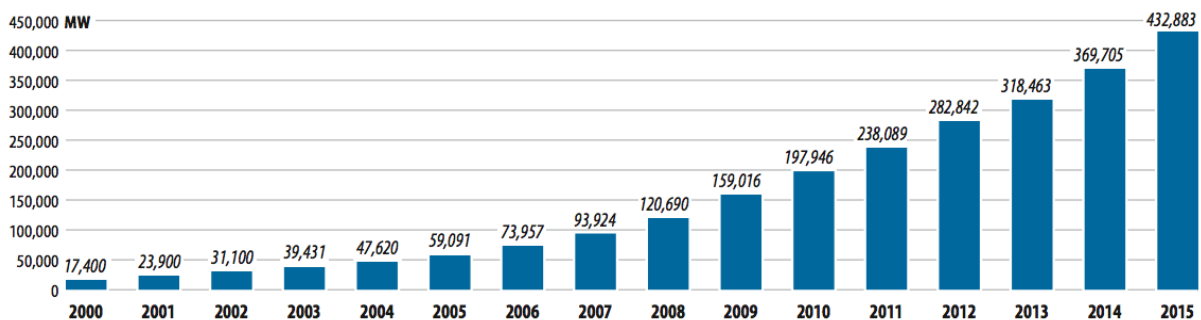


Figure 1.1: Wind power capacity in the world [13]

In parallel to this relatively new source of energy, new manufacturing methods are also emerging. This new set of techniques called rapid prototyping is used to quickly manufacture small objects

such as scale models or prototypes. The most promising of these technologies is additive manufacturing, also known as 3D-printing. It is opposed to subtractive manufacturing because it adds material layer by layer to form an object instead of removing it from a solid block of material. This technology has revolutionized the way to design an object because the path of the tool around the object is no longer limited by its final shape. The object can be hollow or have a varying density. Moreover, the cost of this technology has decreased a lot and is now affordable for personal use. This has led to the creation of numerous *fab labs* in universities and big cities. *Fab labs* are places open to the public and equipped with 3D printers and other means of rapid prototyping. For instance, the *Makilab* is a *fab lab* that opened in Louvain-la-Neuve in 2014. Finally, thanks to computer-aided design, it is very easy to share design files with other people. Thus we decided to take advantage of 3D printing to design and build a new prototype of small horizontal axis wind turbine.

## 1.2 Wind power

Before reviewing previous work on the subject we must quickly recall the basics of wind power. A wind turbine produces electrical power by slowing down the wind. First, the rotor transforms a fraction of the available kinetic power of the wind  $P_{kin}$  into mechanical power  $P_{mec}$ . This transformation is characterized by the **power coefficient** of the wind turbine:

$$C_P = \frac{P_{mec}}{P_{kin}} = \frac{P_{mec}}{0.5\rho V_0^3 A_R}$$

where  $V_0$  is the wind velocity and  $A_R$  is the area swept by the rotor.

The power coefficient is the figure of merit of the wind turbine. It defines the aerodynamic efficiency of its rotor. This aerodynamic efficiency depends on the total velocity seen by the tip of each blade. This velocity is composed of the wind velocity  $V_0$  and the tangential velocity of the tip  $\Omega R$ . The ratio of these two velocities is called the **tip speed ratio** (TSR):

$$\lambda \triangleq \frac{\Omega R}{V_0}$$

As we will see later, the TSR controls the global blade aerodynamics and it can be shown that the power coefficient depends on the tip speed ratio. Each wind turbine has an optimal TSR which maximizes the power coefficient. Maximum power coefficients of modern large wind turbine can reach up to 0.5. Whether the power coefficient is maximized for any wind velocity depends on the regulation of the wind turbine.

After the rotor, the generator of the wind turbine turns this mechanical power into electrical power. As there are losses in the generator (friction, copper and magnetic losses), this transformation is characterized by the **generator efficiency**:

$$\eta_{gen} = \frac{P_{elec}}{P_{mec}}$$

Finally the combination of the power coefficient and the generator efficiency gives the total efficiency:

$$\eta = \eta_{gen} C_P$$

Most of the time, the manufacturers of wind turbines do not give the power coefficient and total efficiency curves with respect to TSR. Instead, they communicate the power curve: this is the instantaneous electrical power produced for a range of wind velocity (see Figure 1.2). On this curve we can see different important values:

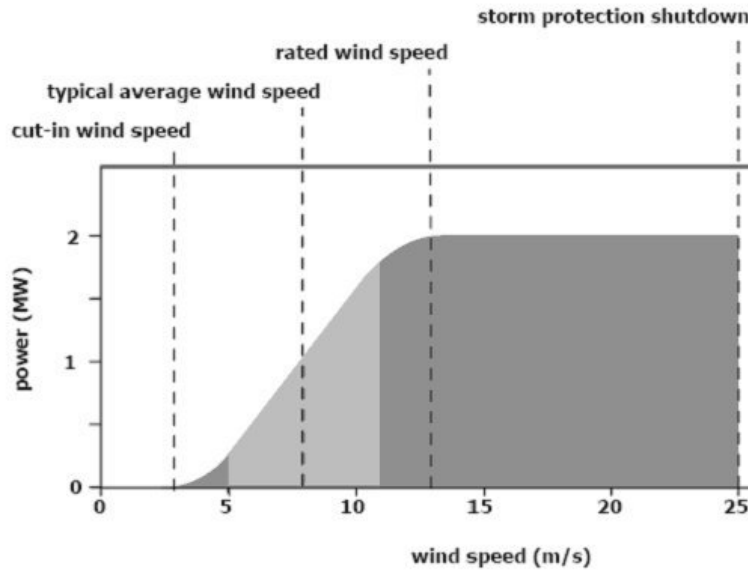


Figure 1.2: Example of power curve [49]

- the cut-in speed  $V_c$ : the wind speed at which the wind turbine begins to produce electrical power.
- the rated speed  $V_r$ : the wind speed at which the rated power  $P_r$  is attained, at this speed the wind turbine is at maximum capacity and over this speed the wind turbine must limit its power output.
- the cut-out speed: this is the maximum wind speed at which the wind turbine can safely produce power, over this speed the wind turbine must be stopped for safety reasons.

### 1.3 State-of-the-art

There is no consensus on the exact classification of small wind turbines. The IEC 61400-2 standard defines small wind turbines as having a rotor diameter  $D$  of less than 8 meters [57]. Kishore, Coudron and Priya [24] proposed a more precise nomenclature:

- micro-scale wind turbine:  $D < 0.1\text{m}$
- small-scale wind turbine:  $0.1\text{m} < D < 1\text{m}$
- mid-scale wind turbine:  $1\text{m} < D < 5\text{m}$
- large-scale wind turbine:  $D > 5\text{m}$

This nomenclature is the one we use in our report. Micro-scale wind turbines are designed to power small sensors in remote locations and are too small for anything else [25]. We will then focus on small and mid-scale wind turbines in this literature review.

First, there is a wide choice of commercially available small and mid-scale wind turbines. We gathered the characteristics of some of them in Table 1.1. We immediately noticed that constructors do not share much information about the aerodynamics of their wind turbines: we only have the power curve. Most of these models have a simple design to reduce their price: constant-chord and untwisted blades, small DC generator, basic regulation, etc. This results in low overall efficiencies compared to large-scale wind turbines. We also noticed the high number

of blades in comparison with three-bladed large-scale wind turbines. Finally, none of them is built using 3D-printing.

There are few scientific studies about the design of small-scale wind turbines. Fortunately, unlike documentation of commercially-sold wind turbines, scientific articles give much more useful information. Hirahara et al. [22] developed a 4-bladed 0.5 m diameter wind turbine called  $\mu$ F500. They used the NACA2404 airfoil and linearly tapered and twisted blades. They experimentally obtained a maximum power coefficient of 0.4 and a total efficiency of 0.28, which is higher than all the commercially available wind turbines presented. Finally, the optimal TSR of their wind turbine is 2.7, which is much lower than for usual large-scale wind turbines (see Vestas V80 in Table 1.1). Kishore, Coudron and Priya [24] developed a 0.394m diameter prototype of small-scale wind energy portable turbine (SWEPT). Their objective was a very low cut-in velocity in order to produce power even with very weak wind. They found a cut-in speed of 2.7 m/s, which is quite low, but at the expense of a very low maximal power coefficient: only 0.14. As the  $\mu$ F500, the SWEPT has a low optimal TSR compared to large wind turbines. Kishore and Priya [25] then developed a second version of the SWEPT. It has the same number of blades and almost the same diameter as the older SWEPT. But they achieved a much better power coefficient of 0.32 with almost the same cut-in velocity: 3 m/s. Finally, the blades and the hub were 3D-printed and withstood rotational speeds of over 1600 rpm without problem. However, the rated power is still very limited: only 1W.

Type	Wind turbine	D [m]	B	$V_c$ [m/s]	$V_r$ [m/s]	$P_r$ [W]	$\lambda_{opt}$	$C_P$	$\eta_{max}$
Commercial design	Rutland 504 [40]	0,51	6	3	11	30			0.18
	Rutland 914i [41]	0,91	6	3	11	143			0.27
	Superwind 350 [48]	1.2	3	3.5	12,5	350			0,26
	Aeromax Lakota [3]	2,09	3	2.7	12.87	1000			0.22
	Skystream 3.7 [45]	3.72	3	3.2	11	2100			0.24
3D printed	Reprap wind turbine [39]	0.84	3	2.8	4,15	5			0.2
Research	SWEPT [24]	0.394	3	2.7	5	0.83	2.9	0.14	0.089
	SWEPT 2 [25]	0.4	3	3	4	1	4.1	0.32	0.20
	$\mu$ F500 [22]	0.5	4	3.6	12	50	2.7	0.4	0.28
Large-scale wind turbine	Vestas V80 [57]	80	3	4	16	$2 \times 10^6$	8		0.435

Table 1.1: Examples of existing small wind turbines

Finally, there are also many small wind turbine models on DIY communities such as *Thingiverse* or *Shapeways*. Most of the time these designs are only concepts and the designers give no information about performance. However there is one interesting project: the Reprap wind turbine [39]. To build it, you must first purchase the construction manual, print the parts in your own 3D printer and then assemble it. It proves the possibility to create a small wind turbine

entirely with 3D printing. The electromechanical converter is a home-made DC generator. The brushes are made from old parts from a cordless screwdriver. The blades are only made from flat aluminum and the performance of the wind turbine is then very low.

## 1.4 Objectives

The main objective of our master's thesis is to design and build a small-scale horizontal axis wind turbine by 3D printing in order to allow everyone to reproduce it in another *fab lab*. To assemble the wind turbine, we use parts that are easy to find in hardware stores: bolts, screws, threaded rods, etc.

To reach this objective, we use a lot of very different branches of engineering: aerodynamics, electromechanical engineering, power electronics, etc. Moreover, the design must comply with the limitations of 3D printing.

After this chapter of introduction, the second chapter details the manufacturing means that are at our disposal. Then, we explain the limitations of 3D printing and how it affects our project. Based on these limitations and weaknesses identified in previous research, we set a list of realistic specifications that we will try to meet.

In the third chapter we study the aerodynamics of the wind turbine. We develop a numerical method that allows us to predict theoretically its power output depending on the shape and dimension of its blades. This method is very well-known but a new method of resolution of the equations was recently found and is implemented in this chapter. Based on this method, we choose the number of blades and the type of airfoil that match the best with our specifications. After building the first rotor, we decided to improve it and design a second one.

The fourth chapter presents the characteristics of the generator that we use in our prototype, the Maxon BLDC EC-40. We analyze its efficiency as a generator and we study its thermal properties. In the second part of this chapter, we begin the design of a 3D printed generator to replace the Maxon generator. We choose its main characteristics and develop its thermal model. However, we do not build it due to a lack of time and resources.

In the fifth chapter, we design the parts of the wind turbine and of the whole assembly. For each piece, we propose different solutions, analyze them and choose the best fit based on specifications and constraints. At the end, different views of the total assembly are given.

Finally, in the sixth chapter, we present the results of the tests we did to assess the performances of our prototype and its two different rotors. We tested it in two subsonic wind tunnels: one is located in our university, the other is located in the Von Karman Institute in Brussels. First we compare these two wind tunnels. Then we detail the measuring instruments that we used and the test bench that we put in place. Finally we analyze the results of the tests.

To end our thesis, we draw conclusions from our findings and present prospects for the continuation of our work.



## Chapter 2

# From manufacturing constraints to specifications

In this chapter, we study the manufacturing methods we chose to realize our project. First, we explain the 3D printing process and give its limits. Then we detail the machines at our disposal: there is one high grade 3D printer at Université Catholique de Louvain and two simpler models at the *Makilab* (a *fab lab* installed in Louvain-la-Neuve). Indeed we need to take the limits of these particular machines into account before beginning the design of our prototype. We also briefly introduce the laser cutting manufacturing method, as it is also available at the *Makilab*. Finally, we develop specifications for our project based on the limitations of our manufacturing methods and on the objectives of our project.

### 2.1 3D printing

3D printing, also known as additive manufacturing, is a new kind of manufacturing developed in the 1980s. It adds material layer by layer to form an object instead of removing it from a solid block of material like older manufacturing methods do.

#### 2.1.1 Printing process: fused deposition modeling

The concept of building an object layer by layer is quite simple but there are several different additive processes to achieve the formation of a layer: stereolithography, selective laser sintering, selective laser melting, etc [16]. Each one is adapted for a different kind of material. The most widespread one is fused deposition modeling. For this technique the 3D printer is made of an extrusion head mounted on a cartesian robotic arm powered by 3 servomotors. The head heats a thermoplastic over its melting point and extrudes it along a predetermined path (see Figure 2.1). The speed of the extruder head determines the layer thickness. The thermoplastic cools off quickly after being extruded, solidifies and bonds with adjacent material to form the layer. This method is popular for personal use because the necessary hardware is simple compared to other methods and it uses a cheap material (thermoplastic).

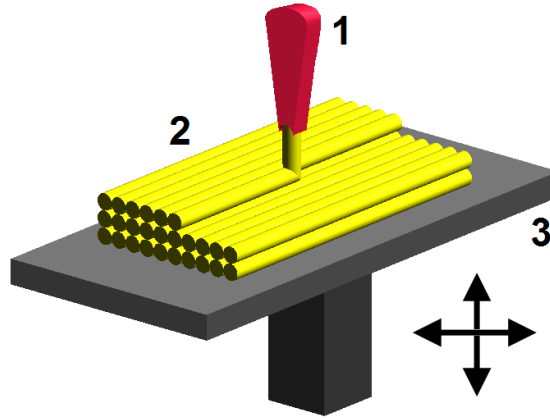


Figure 2.1: Fused deposition modeling [53]

### 2.1.2 Materials

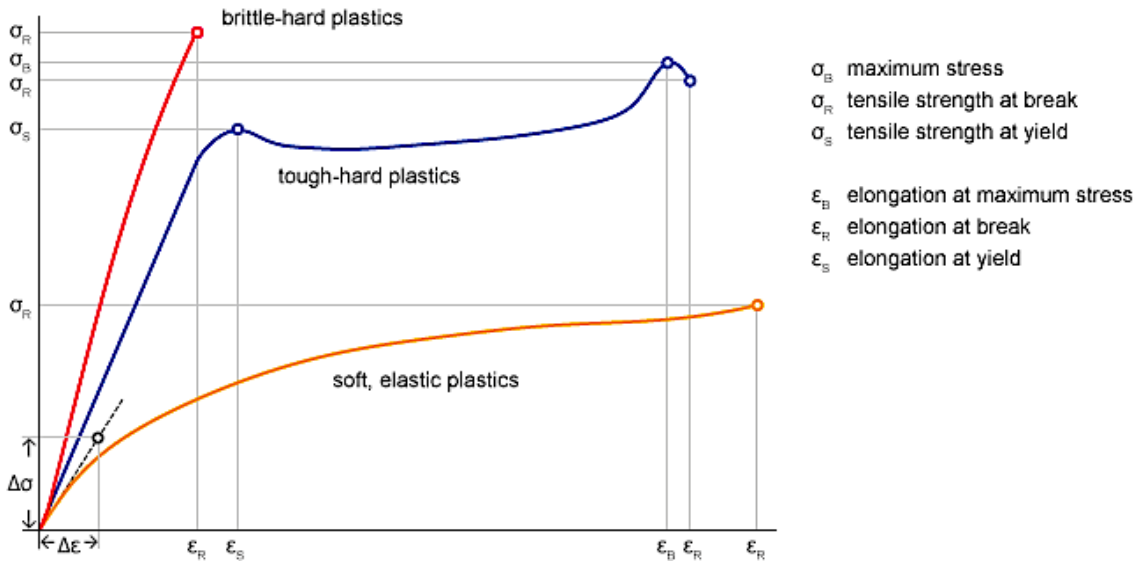


Figure 2.2: Example of stress-strain diagram

In this section, we present the main thermoplastics used for FDM 3D printing: acrylonitrile butadiene styrene (**ABS**) and polylactic acid (**PLA**). Their most important physical properties are:

- density  $\rho$ : it determines the weight of the printed parts.
- glass-transition temperature  $T_g$ : it is the temperature at which a material exhibits a glass transition and becomes rubber-like, this temperature should not be exceeded while the printed parts are under load.

We also compare their deformation under stress. This deformation is illustrated in the stress-strain curve (see Figure 2.2). This curve is defined by several mechanical properties:

- Young modulus  $E$ : slope of the stress-strain curve for elastic deformation (see Figure 2.2), it shows the stiffness of the material.
- yield strength  $\sigma_s$ : stress at which the material begins to deform plastically (see Figure 2.2), this is the maximal stress that should be applied to a part under normal operation.

- elongation at break  $\epsilon_r$ : ratio between deformed length and initial length after breakage, it shows if a material is rather brittle or ductile.

The values of these properties are given in Table 2.1. Young modulus and yield strength values were experimentally found in [50], other values come from the datasheets. We must emphasize the fact that these properties depend heavily on the chosen parameters for each print. Therefore they should not be seen as precise limits but more like qualitative values. We see that ABS is slightly more stiff than PLA (higher Young modulus for ABS) but they approximately have the same yield strength. ABS is lighter than PLA, which is an advantage for our project (to limit the inertia of the rotor and the centrifugal stresses). Moreover, we notice that the elongation at break of PLA is much smaller than the elongation of ABS. It means that PLA is much more brittle than ABS and a part printed in PLA will break more likely under an impact than a part printed in ABS. Finally, the glass transition temperature of ABS is higher than that of PLA. It means that ABS is more resistant to temperature than PLA. For all these reasons, we decided to use ABS instead of PLA to print our parts.

Material	$\rho$ [g/cm <sup>3</sup> ]	$\sigma_s$ [MPa]	$E$ [GPa]	$\epsilon_r$ [%]	$T_g$ [°C]
ABSplus P430 [47, 50]	1.06 - 1.08	31.05	2.12	6	108
PLA Polymax [36, 50]	1.17 - 1.24	31	1.975	1.36	50-60

Table 2.1: Properties of 3D printing materials

### 2.1.3 Printing parameters and limitations

Before printing a part on a 3D printer, it is designed on a CAD software and then "sliced" by a specific program. It means that the needed path of the head extruder to produce the object is computed. There are several parameters that we can change to influence this path and the characteristics of the final object :

- filling: the quantity of matter within the outline of the part.
- layer thickness
- support generation: a temporary construction which supports the overhangs of hollow or concave parts.
- the printing speed

We can see on Figure 2.3 different fillings. Higher is the filling, higher is the time of printing and the mass of 3D-printed piece. The strength of the object in traction and compression depends on the type and direction of filling. To create an object resistant to compression, the better filling is the honeycomb one. It consists in filling the piece with regular hexagons. To create an object that will resist to stresses in one direction, the solution is to make the filling parallel to this one. The problem of making such a piece is that that creates an highly anisotropic object. A squared filling increases the isotropy.

The layer thickness is the parameter that will influence the smoothness of the object in the printed direction z. A smaller layer thickness will increase the printing time but the surface of the object will be more precise. It's due to the fact that the thickness influences the number of layers. So this parameter is important to adjust the desired degree of precision.

3D printers can manage overhangs of angles until 50-60°. Once this limit is exceeded, the 3D printer has to build a support . Actually, with such an high angle, each layer doesn't have enough support from the layer below to maintain his desired position and will flow over this one. The

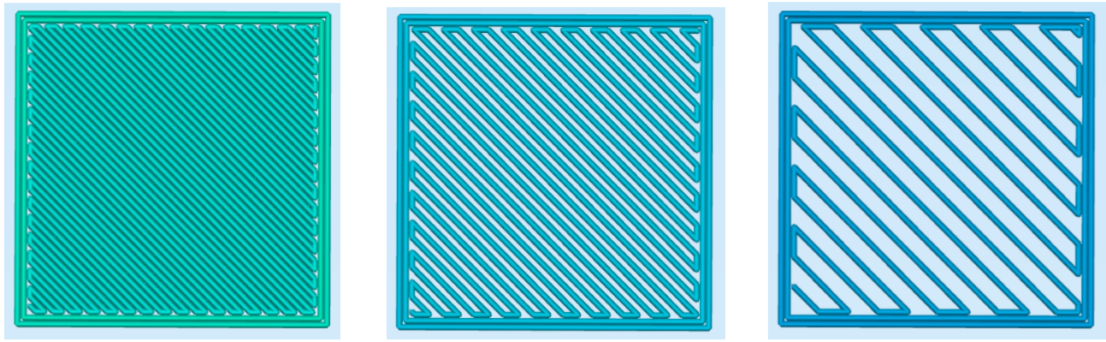


Figure 2.3: Fillings of 100%, 60% and 30% (from [50])

support can be used to maintain a relatively thin piece in position during the printing. Indeed the nozzle movement can produce a small motion of thin pieces during printing that will induce a bad finish of surface. Another use of the support is to hold the object at the printing table. Some materials suffer a thermal contraction that may be important. For this reason it's important to hold the piece during the printing to avoid any buckling.

In the majority of 3D printers, especially the ones available by everyone, the support is made of the same material as the object. It's so printed with a small density to permit to remove it the most easily possible. In other machines, the support is a soluble material. It allows to pull out it without a manual intervention and then give a better finish for 3D-printed pieces. A lot of adjustable parameters are available to adjust the support: thickness of layer, minimum angle, minimum surface, number of layers for the holding.

The printing speed influences the precision. The lower is the speed, the higher is the precision and the longer is the printing. Generally the fast speed is only used to see the general aspect that may have an object.

#### 2.1.4 Available 3D printers

Nowadays, there are numerous *fab labs* and *hacker spaces* in universities and big cities. These places provide access to 3D printers for a small fee and allow anyone to become a designer. For example, the *Makilab* is a *fab lab* in Louvain-la-Neuve that opened in 2014. It is equipped with a laser cutter and two consumer grade 3D printers: the Up! mini and the bq Witbox. The Université Catholique de Louvain also has its own 3D printer, the high grade Fortus 250mc.

The characteristics of these 3D printers can be found in Table 2.2. Based on these characteristics, we will now choose the 3D printer that is the best fit for our thesis.

3D printer	Build volume	Material	Layer thickness	Cost
<b>Fortus 250mc</b>	$254 \times 254 \times 305\text{mm}^3$	ABS/PLA	0.178 - 0.33 mm	0,5€/g + 15€ per print
<b>bq Witbox</b>	$210 \times 297 \times 200\text{mm}^3$	PLA	0.2 - 0.3 mm	0,1€/g
<b>Up! Mini</b>	$120 \times 120 \times 120\text{mm}^3$	ABS	0.2-0.35 mm	0,1€/g

Table 2.2: 3D printers at UCLouvain

Printing in the Fortus is more expensive than in the others. It's due to the fact that it's a professional machine that prints with an ABS with better properties that can be used for medical application. Moreover it needs a new support shelf, that costs 15€, for every utilisation of the

machine. Both others have the same cost of printing of 0.1 €/g. But as the PLA is more dense, at identical volume, the printing in PLA will be a bit more expensive.

At the level of printing quality and capacity, the Fortus is the best. It has the biggest possible printing volume ( $254 \times 254 \times 305\text{mm}^3$ ) and a better precision than the others (0.178 - 0.33 mm). Another advantage of the Fortus is that the support is soluble. As we don't have to remove the support manually, it signifies that the surface finish is better for all the areas where the support is present. The Up! Mini has the smallest printing volume that is less than a quarter than the Fortus one ( $120 \times 120 \times 120\text{mm}^3$ ). With the Witbox, we are allowed of printing objects that have more or less two third of the ones we can make in the Fortus (printing table of  $210\text{ mm} \times 297\text{ mm} \times 200\text{ mm}$ ). From a precision point of view, there are not big difference between both 3D printers of the Makilab: they both have a lower precision of 0.2mm.

If we make our choice based on printing precision and capacity, we would choose the Fortus. But one goal of our project is to use rapid prototyping to make a wind turbine that may be create by everyone. The Fortus is a professional machine that we can't find in small *fab lab* for the moment. Furthermore the printing costs are expensive and a limiting factor for small budget. We then choose not to use the Fortus.

So we have to choose between the Up! Mini and the Witbox. From a printing point of view, the Witbox is more advantageous because it allows the printing of bigger pieces. But as we will build a small wind turbine that will have a high rotational speed, we can't afford us to use a breakable material. And we have already seen that PLA possesses worst mechanical characteristics than ABS. Furthermore, the thermal properties of PLA may be inadequate for some pieces. Indeed, in our wind turbine, we will have a generator to transform mechanical power into electrical power and this device will heat. Based on these informations, we finally choose to use the Up! Mini. With it, we will have one main constraint that is the small printing volume at our disposal.

## 2.2 Laser cutting

Laser cutting is a technology that allows to cut or engrave thanks to a laser a lot of material types: wood, some plastics, cardboard, paper, leather, steel, ... The laser displacement is managed by CNC (computer numerical control). These machines have a high quality surface finish. The positioning accuracy of new laser cutters can reach 0.01mm.

The machine that we have at disposal has a work surface of  $60\text{cm} \times 40\text{cm}$  and a power of 80W. The materials allowed to be cut are: wood, acrylic and plexiglas. Slabs of rigid plywood are available in different thickness (3mm/6mm/9mm) and cost 4€ each. The machine needs files in DXF format to work. Depending on the function and the slabs thickness, the execution speed and the laser power have to be chosen cleverly.

This machine can be used for flat parts.

## 2.3 Design specifications

The power produced by a wind turbine depends heavily on the wind speed. We searched data about wind statistics in Belgium. We found the average wind speed at the coast: 6 m/s[30]. But we won't design our wind turbine for this wind speed because wind power is proportional to the wind speed cube (see Figure 2.4):

$$P_{wind} = \frac{1}{2} \rho A v_{wind}^3$$

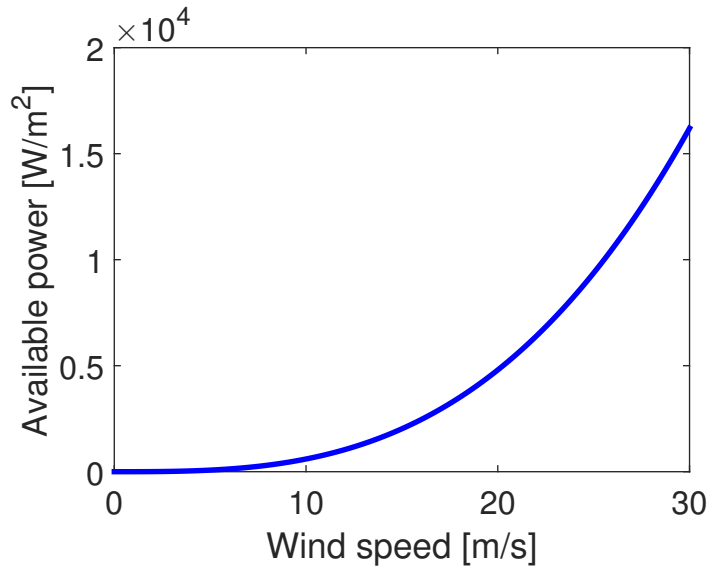


Figure 2.4: Wind power

So we have to find the wind distribution to multiply it by the wind power. We will then obtain the wind energy distribution for every wind speed. The integral of these distribution, also named power density, gives us the total wind power. We know that the wind distribution has the same form as a Weibull distribution. It has the following form:

$$F(v) = 1 - \exp \left[ - \left( \frac{v}{c} \right)^k \right]$$

The k parameter is the Weibull shape factor and illustrate the speeds variability. For wind speed distribution, its value varies between 1 and 3. The weaker is the k factor, the more variable are the wind speeds. On the contrary, a bigger factor will induce less variability. The c parameter is the Weibull scale factor and is proportional to the average wind speed. As we don't know the distribution variability, we use an average k parameter of 2. Based on k parameter and average wind speed, we find the c parameter value: 6.8 [5]. We can now make a graph of the wind distribution (figure 2.5).

By multiplying the wind power by its probability, we find the power density (figure 2.6). We can see on this graph that the wind speed at which we will produce the most is near 10m/s. So it's the wind speed we will use for designing the blades.

There is a theoretical maximum power percentage that we can take from the wind power. It is named the Betz limit and its value is 16/24. Small wind turbines have a performance coefficient that can potentially reach 0.4 [22]. Our objective is to reach the best performance coefficient possible, so we allocate a desired value of 0.4 to this coefficient. On figure 2.6, we drew the power densities using Betz limit and our theoretical performance coefficient.

Due to the 3D printer constraints, we can't print the blades in one piece. More pieces we will use to do the blades larger will be the diameter and the power we could take from the wind. But a larger wind turbine will have as consequence a more complex assembly. We decided to make two rotors: one of four pieces and one of three pieces. As the Up! Mini can't print more than 120 mm in any direction. It gives us an approximate radius of 360 mm for the small and 480 mm for the large. With this radii, we can calculate the theoretical power taken from the wind at

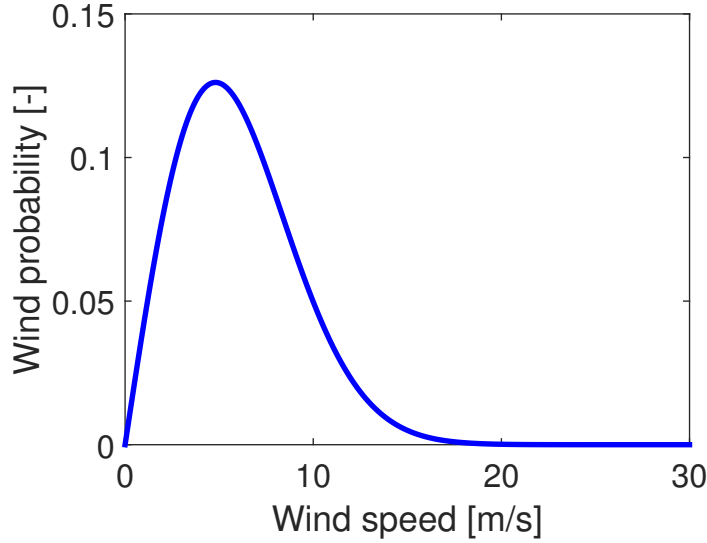


Figure 2.5: Wind distribution

our nominal wind speed:

$$\begin{cases} P_{meca1} = C_P \cdot P_{wind} = C_P \cdot \frac{1}{2} \cdot \rho \cdot \pi R_1^2 \cdot v_{wind}^3 = 97.72W \\ P_{meca2} = C_P \cdot P_{wind} = C_P \cdot \frac{1}{2} \cdot \rho \cdot \pi R_2^2 \cdot v_{wind}^3 = 173.72W \end{cases}$$

Where index 1 refers to the small blades set and 2 refers to the large ones.  $C_P$  is the power coefficient that we previously choose equal to 0.4.

We know that power is proportional to the mechanical torque and the rotational speed ( $P = \omega \cdot T$ ). We have to do a compromise between both parameters. On one hand we can't impose an excessive torque. Indeed, for a fixed length generator value, the torque that it can admit is proportional to the cube of generator radius [38]. We can't create an extremely large generator as it will perturb the air flux at the blades base. On the other hand we won't allow an excessive rotational speed because centrifugal stresses are proportional to the square of this one. Centrifugal forces may cause the blades break and so the destruction of the wind turbine.

After reading of some articles ([25, 24, 22]), we decided to impose a rotational speed of 750 rotations per minutes [rpm]. We can now calculate the maximal torque for the motor design:

$$\begin{cases} T_1 = \frac{P_{meca1}}{\omega_1} = \frac{97.72}{\frac{750}{60} \cdot \frac{2\pi}{60}} = 1.24N \\ T_2 = \frac{P_{meca2}}{\omega_2} = \frac{173.72}{\frac{750}{60} \cdot \frac{2\pi}{60}} = 2.21N \end{cases}$$

By giving a numerical efficiency for the generator, we can approximate our desired nominal electrical power. Let's give a plausible value at the generator efficiency:  $\eta_{gen} = 0.8$ . We can now calculate the estimated electrical power:

$$\begin{cases} P_{elec1} = P_{meca1} \cdot \eta_{gen} = 78.2W \\ P_{elec2} = P_{meca2} \cdot \eta_{gen} = 139W \end{cases}$$

More explanations can be found about generator torque in chapter 4, and about rotational stresses in chapter 3. As summary of this chapter, all the main design specifications are put in table 2.3.

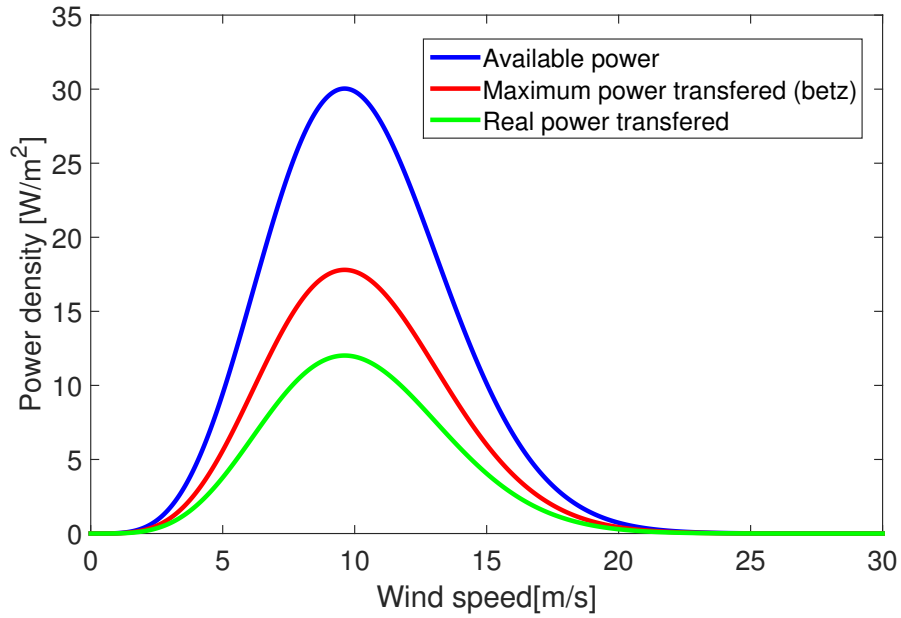


Figure 2.6: Power density

	Rotor 1	Rotor 2
Design wind speed	10 m/s	
3D printer	Up! Mini (ABS)	
Performance coefficient goal	0.4	
Mechanical nominal power	± 98W	± 174W
Nominal rotational speed	750 rpm	
Nominal generator torque	1.24 N	2.21 N
Nominal generator efficiency	0.8	
Electrical nominal power	± 78W	± 139W

Table 2.3: Wind turbine specifications

## Chapter 3

# Aerodynamical design

Wind turbines are aerodynamical devices which produce mechanical power by extracting kinetic power from an air flow. Thrust  $T$  is applied in the direction of the flow and torque  $Q$  is applied to mechanical shaft. The critical parts of the wind turbine in this transformation of power are the blades (attached to the rotor). In order to optimize the power produced, we must understand how the blades of a wind turbine interact with the flow to create the thrust, the torque and extract power.

The main goal of this chapter is to explain how we designed the blades of our wind turbine. First we give some necessary elements of aerodynamics. Then we show how we developed the numerical method (i.e. the Blade Element Momentum method) that we use to simulate the flow around wind turbine blades. Finally we use this method to find the best shape for our blades, in relation with the general specifications of our wind turbine.

We will also quickly introduce the roles of the tail fin and the duct but those elements were not studied in detail for this report.

### 3.1 Momentum theory

Developed by Rankine and Froude and then refined by Betz and Glauert [19], the momentum theory is the first and most simple aerodynamic theory of wind turbines. It was originally created to study airplane propellers. As this theory has already been extensively detailed in a lot of reference books [10, 19, 57], we will only give the main results here.

#### 3.1.1 Actuator disc (1-D analysis)

To extract kinetic power from the wind, the rotor must slow down the flow. But a sharp discontinuity of velocity at the blades would imply very high forces on the blades and that is not a good thing. Instead, the flow is gradually slowed down in front of the wind turbine and behind it.

To study this deceleration, the momentum theory assumes that the rotor behaves like an actuator disk. It means that the rotor has no thickness and that the air velocity is constant through it (the momentum theory is then a 1-D analysis). The actuator disk must then create a discontinuity of pressure between the upstream and the downstream to induce the deceleration of the flow. The volume used for this analysis is of course the stream-tube that surrounds the flow going through the rotor. As the flow is slowed down, this stream-tube expands to keep the mass flow

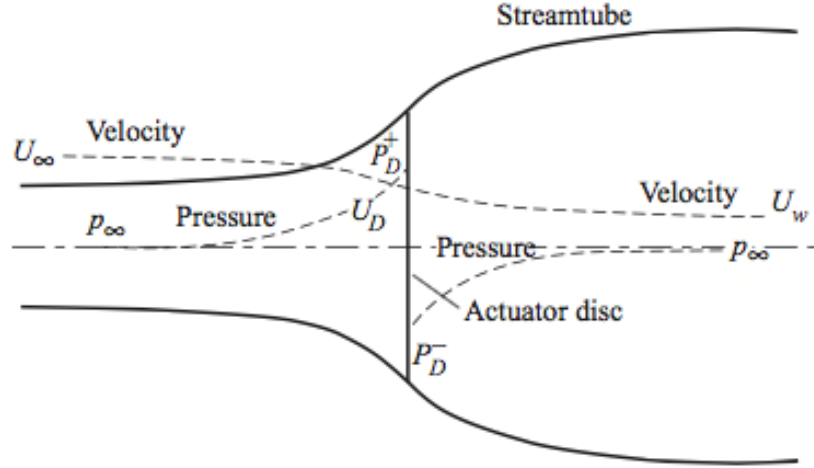


Figure 3.1: Actuator disc and streamtube (from [10])

constant (see fig. 3.1, the stream-tube radius is smaller than the rotor radius upstream and bigger downstream). Other hypotheses for the momentum theory are:

- incompressible flow (compressible flow can be taken into account but is not relevant at natural wind speeds)
- steady and uniform flow with free stream velocity  $V_0$  in front of the rotor (no turbulence)

We can then define the **axial induction factor**, it is the ratio of the negative velocity induced by the wind turbine in front of it and the free stream velocity:

$$a \triangleq \frac{v_x}{V_0}$$

$$V_R = V_0(1 - a)$$

with  $V_R$  the velocity at the rotor.

By conservation of mass and momentum in the whole stream-tube, we can express the thrust in function of the velocity in the flow and by conservation around the rotor, we can express it in function of pressure:

$$T = \dot{m}(V_0 - V_W) = \rho A_D V_R (V_0 - V_W)$$

$$= (p_D^+ - p_D^-) A_D$$

with  $V_W$  the velocity of the wake,  $\dot{m} = \rho A_D V_R$  the mass flow through the stream-tube and  $A_D = \pi R^2$  the rotor disc area.

Then we apply Bernoulli's equation in front and behind of the rotor to obtain:

$$V_W = V_0(1 - 2a)$$

with  $V_W$  the velocity in the wake of the wind turbine.

We see that the velocity of the flow is slowed down as much in the front of wind turbine than in the wake.

From there, we can express the thrust applied on the wind turbine and power extracted by the wind turbine in function of the axial induction factor:

$$T = \rho V_0^2 A_D 2a(1 - a)$$

$$P = \dot{m}(V_0^2 - V_W^2) = \rho V_0^3 A_D 2a(1 - a)^2$$

To analyze a wind turbine's efficiency regardless of its size, we define two dimensionless coefficients, the thrust and power coefficients:

$$C_T \triangleq \frac{T}{1/2\rho V_0^2 A_D}$$

$$C_P \triangleq \frac{P}{P_{cin}} = \frac{P}{1/2\rho V_0^3 A_D}$$

For the momentum theory, we have:

$$C_T = 4a(1 - a) \tag{3.1}$$

$$C_P = 4a(1 - a)^2 \tag{3.2}$$

### 3.1.2 Betz limit

If we optimize eq. (3.2) for  $a$ , the maximum power coefficient is reached for  $a_{opt} = 1/3$  and is called the Betz limit:

$$C_{P,max} = 16/27 \simeq 0,59$$

According to the momentum theory, the mechanical power extracted by the wind turbine cannot exceed 59% of the kinetic power of the flow, regardless of the design of the blades. This is a very important deduction, as it gives us an indication on how much power we can expect to harvest from the wind.

### 3.1.3 Breakdown of the momentum theory

For axial induction factors greater than  $1/2$  ( $a > 1/2$ ), the wake speed becomes negative:

$$V_W = V_0(1 - 2a) < 0$$

This is of course impossible for the mass flow of the wind turbine. Indeed, at that point the flow becomes turbulent and breaks one of the momentum theory hypotheses. Then the momentum no longer makes physical sense above  $a = 1/2$ . In the next section, empirical relations will be presented to solve this problem.

## 3.2 Blade Element Momentum method

The Blade Element Momentum method (BEM method) is a very popular numerical method based on the momentum theory presented in the last section. For the implementation, we followed the approach of Ning in *A simple solution method for the blade element momentum equations with guaranteed convergence* [33]. This section will present the equations in the same way as this article.

### 3.2.1 Definitions

The rotor is composed of  $B$  blades. The torque applied on the rotor through its blades is  $Q$ . Similarly to  $C_T$  and  $C_P$ , we define a dimensionless coefficient to describe the torque:

$$C_Q \triangleq \frac{Q}{1/2\rho V_0^2 A_D R} = \frac{C_P}{\lambda}$$

The rotor of the wind turbine has a rotational speed  $\Omega$ . The mechanical power produced is  $P = \Omega Q$ . In order to study the effect of the rotational speed on the efficiency of the wind turbine regardless of the free stream velocity, we define a dimensionless number called the **tip speed ratio** (TSR) :

$$\lambda \triangleq \frac{\Omega R}{V_0}$$

As we will see later, the TSR controls the global blade aerodynamics.

### 3.2.2 Rotor disc and blade elements (2-D analysis)

The actuator disk allowed us to deduce how much power we can extract from the flow but it did not explain how the flow apply a torque on the rotor. Indeed, by conservation of the angular momentum, if a torque is applied by the flow on the rotor, the rotor must induce a tangential velocity  $\omega_\theta$  on the flow and that was not predicted by the momentum theory. We must then modify the actuator disk hypothesis.

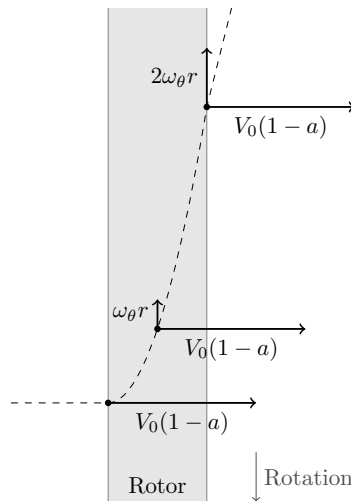


Figure 3.2: Rotor disc and tangential induced speed (seen in the  $e_x - e_\theta$  plane)

The tangential velocity cannot be instantly induced. Thus, we assume that the rotor has some thickness and induce the tangential velocity gradually along its thickness (see fig. 3.2). The

unknown total tangential velocity after the rotor is  $2\omega_\theta r$ . We also assume that the mean tangential velocity over the thickness of the rotor disk is half the tangential velocity of the wake:  $\omega_\theta r$ . From this observation we can define the **tangential induction factor** as the ratio of the mean tangential velocity in the rotor disk and the rotational velocity of the rotor disk (see vectors of fig. 3.2):

$$a' \triangleq \frac{\omega_\theta}{\Omega}$$

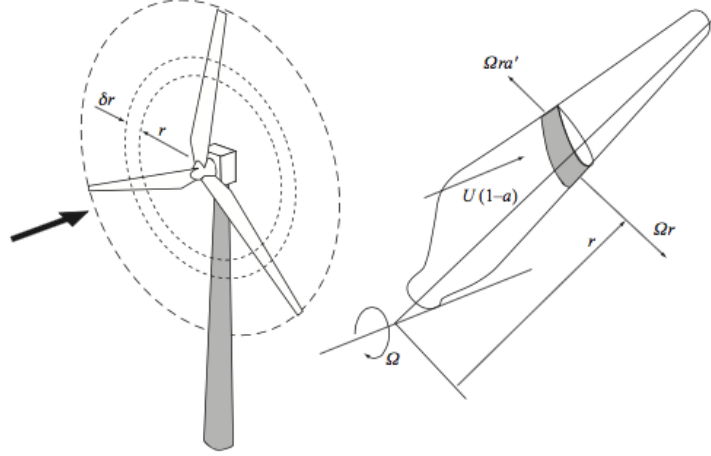


Figure 3.3: Blade element (from [10])

This factor  $a'$  will likely vary along the blade radius. Indeed, if we divide the rotor disc into  $n$  concentric rings (see fig. 3.3), each ring will deflect the flow differently depending on the local shape and size of the blade. These concentric rings are called blade elements. We make two assumptions on them:

- The flow in the stream-tube of each blade element is independent from the others.
- Blade elements behave as two-dimensional airfoils which produce lift and drag for a given airspeed, angle of attack and Reynolds number:

$$C_l = f_l(\alpha, Re_c) \quad (3.3)$$

$$C_d = f_d(\alpha, Re_c) \quad (3.4)$$

To describe these  $n$  blade elements, we define local characteristics:

- the local radius of the blade element  $r$  (see fig. 3.3).
- the local solidity  $s$ , the local percentage of the ring perimeter which is occupied by the blades:

$$s = \frac{Bc}{2\pi r}$$

where  $B$  is the number of blades of the rotor and  $c$  is the local chord of the blade.

- the local tip speed ratio  $\lambda_l$ , the ratio between the tangential speed of the blade element and the free flow velocity:

$$\lambda_l \triangleq \frac{\Omega r}{V_0} = \lambda \frac{r}{R}$$

The flow is now divided in  $n$  blade elements that we will analyze separately to take into account the variation of  $a'$  (2-D analysis).

### 3.2.3 Geometry of a blade element

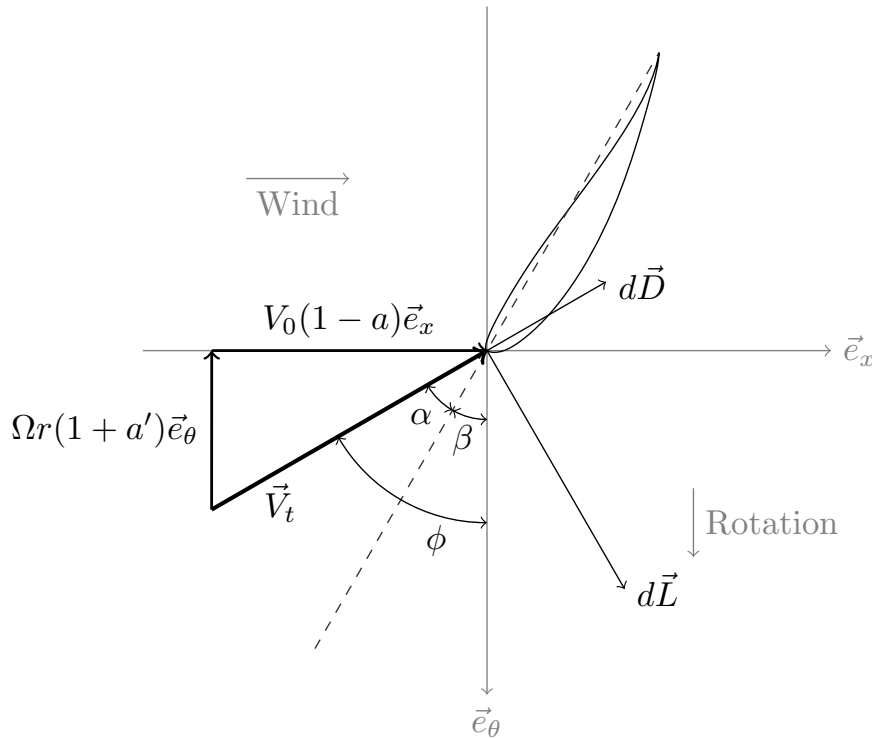


Figure 3.4: Flow around a blade element

Each blade element can now be analyzed separately. On fig. 3.4, we represented the geometry of the flow around a blade element. The total air velocity seen by the airfoil is the vector sum of the free flow velocity, the rotational speed and the axial and tangential induced velocities:

$$\vec{V}_t = (V_0 - v_x)\vec{e}_x + (\Omega + \omega_\theta)r\vec{e}_\theta$$

The Reynolds number of the blade element uses the local chord as characteristic length but doesn't have to consider the induced velocities, as they don't change the order of magnitude of the velocity at the blade:

$$Re_c = \frac{\|\vec{V}_t\|c}{\nu} \simeq \frac{V_0\sqrt{1 + \lambda_t^2}c}{\nu}$$

The different angles are:

- $\beta$  : the twist angle is the angle between the local chord of the airfoil and the rotational plane. It is a constant physical characteristic for each blade element.
- $\phi$  : the inflow angle is the angle between the rotational plane and the flow velocity. It depends on the flow and is computed through the BEM method.
- $\alpha = \phi - \beta$  : the angle of attack of the airfoil is the angle between the local chord of the airfoil and the flow velocity. It is necessary to compute the lift and drag produced by the airfoil.

From fig. 3.4 we can deduce the geometric relationships between the inflow angle and the induction

factor:

$$\frac{\|\vec{V}_t\|}{V_0} = \frac{1+a}{\sin \phi} = \frac{1-a'}{\cos \phi} \lambda_l$$

$$\tan \phi = \frac{1+a}{(1-a')} \frac{1}{\lambda_l}$$

Finally, with the inflow angle, we can rotate the lift and drag coefficients to obtain aerodynamic coefficients in the free flow direction and the rotational plane:

$$C_x = C_l \cos \phi + C_d \sin \phi \quad (3.5)$$

$$C_y = C_l \sin \phi - C_d \cos \phi \quad (3.6)$$

### 3.2.4 Aerodynamic forces and momentum conservation

The mass flow  $d\dot{m}$  through a blade element is :

$$d\dot{m} = \rho dA V_R = \rho 2\pi r dr V_0 (1-a)$$

where  $dr$  is the radial width of the blade element and  $dA$  its area.

If we apply axial and angular momentum conservation on a blade element, we obtain:

$$dT = d\dot{m} 2v_x = 1/2 \rho V_0^2 \overbrace{2\pi r dr}^{dA} \overbrace{4a(1-a)}^{C_{T,loc}} = 4\pi r \rho V_0^2 a(1-a) dr$$

$$dQ = d\dot{m} 2\omega_\theta r = 4\pi r^3 \rho V_0 \Omega a'(1-a) dr$$

We can compute the thrust and torque from the aerodynamic coefficients:

$$dT = 1/2 \rho \|\vec{V}_T\|^2 c B C_x dr$$

$$dQ = 1/2 \rho \|\vec{V}_t\|^2 c B C_y r dr$$

By equating aerodynamic and momentum equations and using the relations between the inflow angle and the induction factors, we find:

$$\frac{a}{1-a} = \frac{s C_x}{4 \sin^2 \phi}$$

$$\frac{a'}{1+a'} = \frac{s C_y}{4 \sin \phi \cos \phi}$$

### 3.2.5 Tip and root losses

The tip of each blade sheds a vortex into the wake like a wing. In the original BEM method, there is no influence of these vortices on the induced velocity field. This effect is of course stronger near the blade tips. To take account of this effect we define the tip loss factor as the ratio of the azimuthal (in the  $\vec{e}_\theta$  direction) average of the axial induction factor  $a$  and its value at the blade:

$$F_{tip} \triangleq \frac{a}{a_b}$$

with  $a$  the azimuthal average and  $a_b$  the value at the blade.

Similarly we define a hub loss ratio  $F_{hub}$  which accounts for losses due to the vortex shedding at the root.

Prandtl developed an analytical model for these losses [10]. He simplified the form of the wake of the turbine and found:

$$f_{tip} = \frac{B}{2} \left( \frac{R-r}{r|\sin\phi|} \right) \quad (3.7)$$

$$F_{tip} = \frac{2}{\pi} \arccos(\exp(-f_{tip})) \quad (3.8)$$

$$f_{hub} = \frac{B}{2} \left( \frac{r-R_{hub}}{R_{hub}|\sin\phi|} \right) \quad (3.9)$$

$$F_{hub} = \frac{2}{\pi} \arccos(\exp(-f_{hub})) \quad (3.10)$$

$$F = F_{tip}F_{hub} \quad (3.11)$$

This ratio is used to modify the equations of momentum:

$$\begin{aligned} dT &= 4\pi r \rho V_0^2 a F (1-a) dr \\ dQ &= 4\pi r^3 \rho V_0 \Omega a' F (1-a) dr \end{aligned}$$

This is equivalent to modifying the local thrust coefficient:

$$C_{T,loc} = 4aF(1-a)$$

We define local constants (depending on the inflow angle):

$$k(\phi) = \frac{sC_x}{4F \sin^2 \phi} \quad (3.12)$$

$$k'(\phi) = \frac{sC_y}{4F \sin \phi \cos \phi} \quad (3.13)$$

Finally we find the local BEM equations for the momentum region:

$$a = \frac{k(\phi)}{k(\phi) + 1} \quad (3.14)$$

$$a' = \frac{k'(\phi)}{1 - k'(\phi)} \quad (3.15)$$

### 3.2.6 High-thrust correction

As seen in section 3.1.3, the momentum theory becomes invalid in the high-thrust region (when the axial induction factor exceeds 0,5). This situation happens rarely for well-designed wind turbines (as we want to operate close to the Betz optimum, at  $a = 1/3$ ). But to make a BEM method effective in any case, we must modify the equations for high axial inductions factors.

In 1926, Glauert introduced an empirical relationship for the local thrust coefficient fitting experimental data [18]:

$$C_{T,loc} = 4a(a-1) + 2$$

for  $a > 0,5$ .

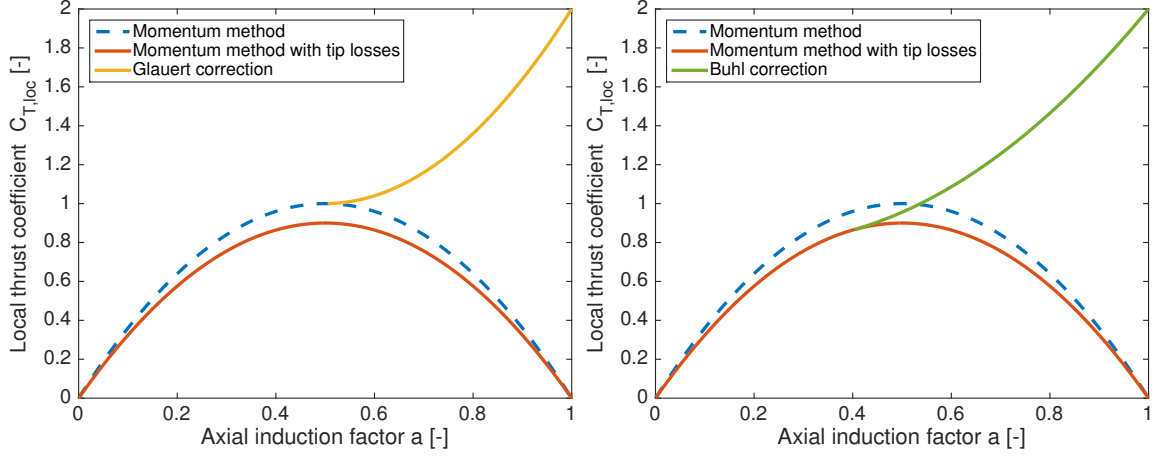


Figure 3.5: Glauert and Buhl high thrust corrections

Unfortunately, if we also use the tip loss factor, there is a discontinuity between the momentum theory and Glauert's empirical high thrust correction (see fig. 3.5). This might cause problems for the BEM method to converge and it must be avoided.

To solve this problem, we use the relation proposed by Buhl [9]. It is a second order polynomial like Glauert's correction but it was derived to close the discontinuity (see fig. 3.5):

$$C_{T,loc} = \left(\frac{50}{9} - 4F\right) a^2 - \left(\frac{40}{9} - 4F\right) a + \frac{8}{9}$$

for  $a > 0,4$ .

If we solve this equation, we obtain the axial induction factor for the high thrust region:

$$\gamma_1 = 2Fk - \left(\frac{10}{9} - F\right) \quad (3.16)$$

$$\gamma_2 = 2F - F\left(\frac{4}{3} - F\right) \quad (3.17)$$

$$\gamma_3 = 2Fk - \left(\frac{25}{9} - 2F\right) \quad (3.18)$$

$$a = \frac{\gamma_1 - \sqrt{\gamma_2}}{\gamma_3} \quad (3.19)$$

### 3.2.7 Residual function and guaranteed convergence algorithm

Now that we found the relation between the induction factors and the inflow angle (i.e. the local BEM eqs. (3.14) and (3.15)), we can use the geometric relationship found in section 3.2.3 to close the problem:

$$\tan \phi = \frac{1+a}{(1-a')\lambda_t}$$

By manipulating this equation, we can define a residual function:

$$\mathcal{R}(\phi) = \frac{\sin \phi}{1-a} - \lambda_t \frac{\cos \phi}{1+a'} \quad (3.20)$$

This residual function is entirely defined by eqs. (3.3) to (3.19) and now the BEM problem amounts to finding the root of this equation. It can be shown that reducing the problem to one dimension is more robust than the usual two-dimensional approach because we can use

very robust one-dimensional root-finding algorithms. It should also be noted that this reducing approach can also be used for propellers.

In order to find the root, Ning advised to use Brent's algorithm because it guarantees the convergence as long as an initial bracket is identified [33]. It is conveniently already implemented in MATLAB in the `fzero` function. To use it, we must identify the different brackets that might contain a physical solution (see [33] for details):

- the momentum/empirical region (the torque is in the same way as the rotational velocity) :  $\phi \in (0, \pi/2]$
- the propeller-brake region (the torque is opposed to the rotational velocity) :  $\phi \in [-\pi/4, 0)$

The propeller brake is not a region of interest for the conception of a wind turbine so there will be a solution for a set of parameters only if:

$$\mathcal{R}(\epsilon)\mathcal{R}(\pi/2) < 0$$

with  $\epsilon$  an arbitrary small number (for example  $\epsilon = 10^{-6}$ ).

### 3.2.8 Extension of the lift and drag coefficients' range

The twist angle  $\beta$  of a blade is usually very low close to the tip of the blade. This creates very high angles of attack when the blade is rotating slowly. However, there is not much data available for the lift and drag of airfoils at these high angles of attack, especially for low Reynolds numbers. In order to evaluate the residual function  $\mathcal{R}(\phi)$  at any  $\phi$  in the bracket, we must extrapolate the airfoil data.

In 1982 Viterna and Corrigan proposed this approximation valid for  $\alpha \in [-\pi/2, \alpha_{low}]$  and  $[\alpha_{high}, \pi/2]$  ( $[\alpha_{low}, \alpha_{high}]$  being the interval of available data) [51]:

$$\begin{aligned} C_l &= A_1 \sin(2\alpha) + A_2 \frac{\cos^2(\alpha)}{\sin(\alpha)} \\ C_d &= B_1 \sin^2(\alpha) + B_2 \cos(\alpha) \\ A_1 &= C_{D,\max} \\ B_1 &= C_{D,\max}/2 \end{aligned}$$

where  $C_{D,\max}$  is related to the aspect ratio of the blade and  $A_2$  and  $B_2$  are chosen to insure continuity with the data at  $\alpha_{low}$  and  $\alpha_{high}$ .

See fig. 3.6

### 3.2.9 Example of application

To show that our method works, we used it for a given set of parameters, as an example. Here are the parameters used:

- number of blade elements: 40
- airfoil: SG6043
- chord and twist distributions: optimal Betz distribution from [10] (see eqs. (3.21) and (3.22))

Those parameters are not particularly important for this example (others could have been used) but their choice will be detailed more thoroughly in the next section.

Results of the simulation are in fig. 3.7.

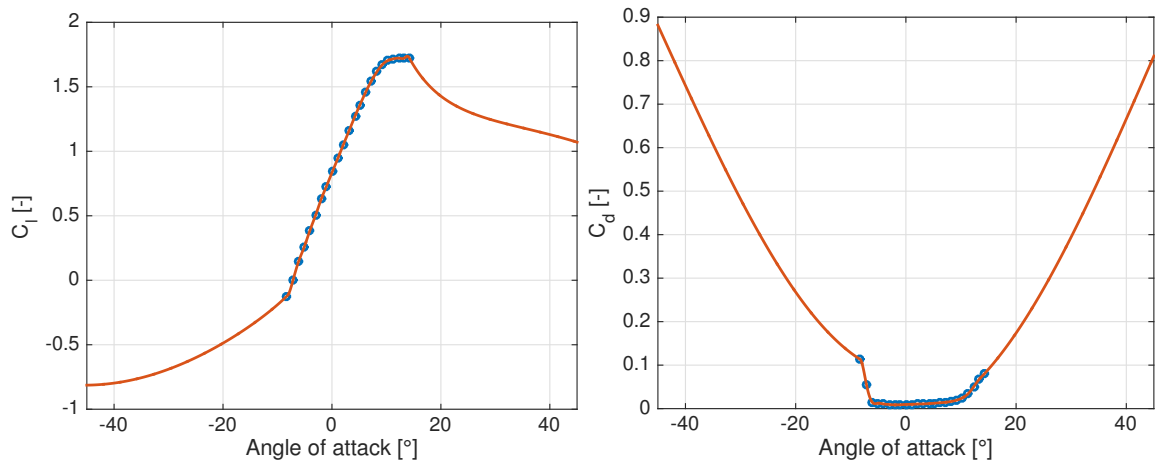


Figure 3.6: Viterna and Corrigan lift and drag extrapolation

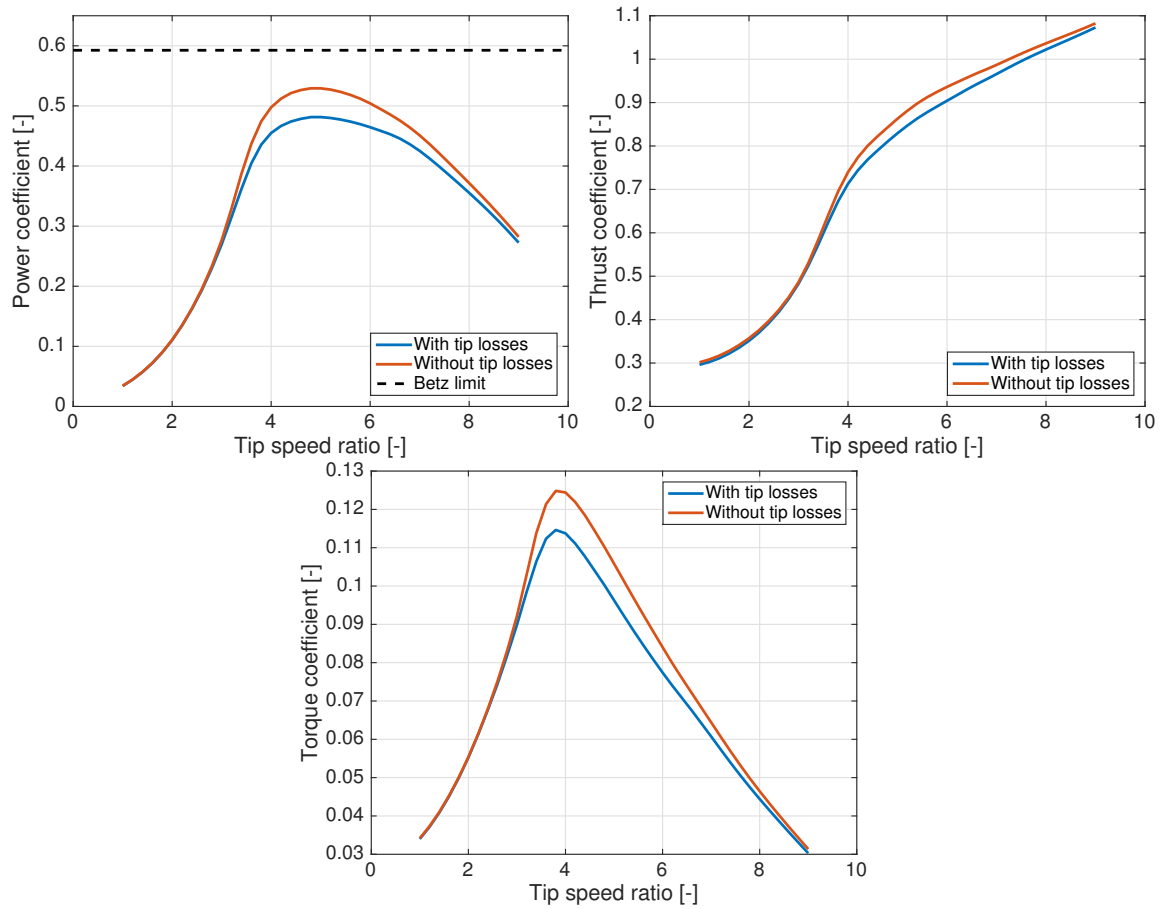


Figure 3.7: BEM method: power, thrust and torque coefficients

### 3.3 Design of the blades

With the BEM method as a tool to predict the thrust and the torque produced by a certain wind turbine, we can now analyze the influence of the shape of the blades on the performance. This shape is defined by these parameters:

- the radius of the hub
- the total radius of the rotor
- the airfoil(s) chosen and its/their lift and drag coefficients.
- the distribution of twist  $\beta(r)$  and chord  $c(r)$  along the blade.

The first two parameters influence the total power produced: the hub should be the smallest possible and the rotor the biggest possible. The hub radius is limited by the size of the nacelle and the total radius by manufacturing methods and structural strength of the blade. The radius of the blades was determined in chapter 2. The size of the generator will be addressed in chapter 5.

The last three parameters (airfoil,  $\beta(r)$ ,  $c(r)$ ) mainly influence the efficiency of the rotor, i.e. the power coefficient  $C_P$ . In this section we will optimize those parameters given our constraints.

#### 3.3.1 Airfoil(s)

The first step in designing the blade is the choice of airfoil. It determines the lift and drag produced by the blade elements and ultimately the performance of the wind turbine. We must notice that the Reynolds number at which small wind turbines operate is usually very low. For example, a wind turbine of  $R = 0.4\text{m}$ , operating at  $\lambda = 3$ ,  $V_0 = 10\text{m/s}$  and of chord  $c = 0.08\text{m}$  at 75% of the blade has a Reynolds number of:

$$Re \simeq \frac{V_0 \sqrt{1 + \lambda_l^2} c}{\nu} = 1.31 \times 10^5$$

This is sufficiently low for laminar separation of the flow to occur before the flow becomes turbulent. Indeed a laminar boundary layer is much more sensible to adverse pressure gradients than a turbulent boundary layer. After separation, either the flow doesn't reattach at all or a laminar separation bubble appears (see fig. 3.8). Either way it degrades the aerodynamic quality of the airfoil. This is why a special attention needs to be given to performances of airfoils at low  $Re$ .

The criteria that we used to choose the airfoil are:

- high maximum lift-to-drag ratio: because the torque of a blade element is proportional to  $C_y = C_l \sin \phi - C_d \cos \phi$ . For variable speed wind turbines, the lift-to-drag ratio doesn't have to be high over a broad range as the regulation insures that the TSR is constant (so the angle of attack of each blade element stays constant).
- low sensitivity to surface roughness: the 3D printed blades will not likely be smooth and that should not impact the airfoil performance too much.
- high thickness to chord ratio: the ABS or PLA used for 3D printing is not as tough as resin composites usually used to mold wind turbine blades, therefore the blade should not be too thin.
- gentle stall behavior: the loss of lift at high angles of attack should not be too brutal to avoid unstable behaviour of the wind turbine.

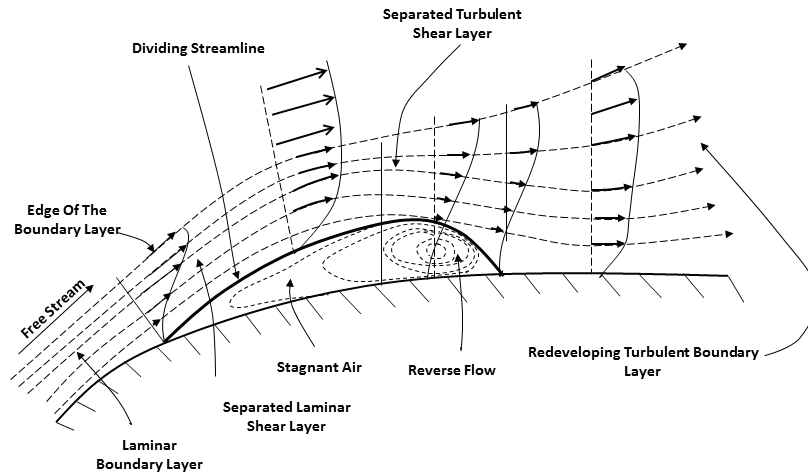


Figure 3.8: Laminar separation bubble (from [54])

Unfortunately there are few airfoils with available experimental data at low  $Re$ . The main source of data that we found is the "Low speed airfoil tests" carried out at University of Illinois at Urbana-Champaign (UIUC) for Reynolds numbers between  $1 \times 10^5$  and  $5 \times 10^6$  (see *Summary of Low-Speed Airfoil Data - Vol. 1,2,3,4 and 5* [42, 43, 44, 29, 55]). Among the airfoils tested at UIUC, we chose to present 3 of them that seemed interesting and we compare them in this section.

### NREL S833, S834 and S835

The S833 airfoil family was developed by the American National Renewable Energy Laboratory (NREL) in 2001 [46]. It was specifically designed for 1-to-3 meter diameter horizontal wind turbines and was therefore optimized for lower  $Re$  than older NREL airfoil families. It consists of 3 airfoils of different thicknesses (see fig. 3.9). The root airfoil is thicker for structural reasons and the tip airfoil is thinner to be quieter. Only the S834 airfoil was tested by UIUC (see fig. 3.12) but we assumed the airfoils of the same family to have roughly the same lift and drag characteristics. See table 3.1 for other characteristics.

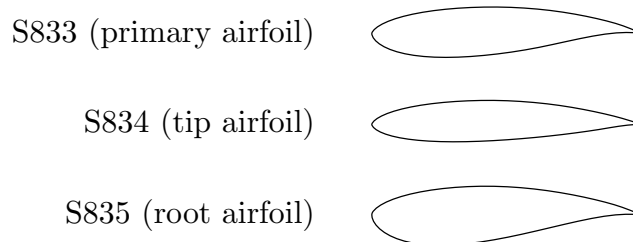


Figure 3.9: NREL S833 airfoil family

### SG6040 and SG6043

The SG6040 and SG6043 airfoils were developed specifically for small variable-speed wind turbines by Michael Selig and Philippe Giguère in 1998 [17]. They are primarily intended for 1kW to 5kW wind turbines, which corresponds roughly to diameters of 1.5m to 3m (with  $C_P = 0.3$  and  $V_0 = 10m/s$ ).

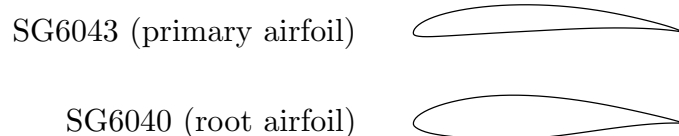


Figure 3.10: Selig and Giguere low Reynolds airfoil family

### Wortmann FX 63-137

The FX 63-137 airfoil was developed by F. X. Wortmann in 1963 as a high-lift, low- $Re$  airfoil. It was used in the Puffin II and Liverpuffin human-powered aircrafts in 1965. Since then it has been used in many low- $Re$  applications because of its high-lift and soft-stall characteristics. In particular, it has been used by Aeromag for the Lakota wind turbine and by Southwest Windpower for the H-40 and H-80 wind turbines [29].



Figure 3.11: Wortmann FX63-137 airfoil

### Comparison

The main characteristics of all the airfoils are in Table 3.1 and the polars are in Figure 3.12, Figure 3.13 and Figure 3.14. Most of the data come from the M. Selig's "Low speed airfoil tests" ([44, 29]) but each airfoil of the presented families was not experimentally tested. For the missing data, we used the data of XFOIL simulations from [4].

First, we notice that all airfoils perform much worse at  $Re$  below  $1 \times 10^5$ . This is because of the apparition of a laminar separation bubble which increases the drag significantly (see the spike in each polar). We also observe that the angle of attack at which the lift-to-drag ratio is maximized is shifted when the  $Re$  changes. This may cause a problem of performance, as a blade will be optimized for the rated wind speed and might be less efficient at slower speeds.

The best airfoil is the SG6043: it has the highest lift-to-drag ratio at both Reynolds numbers. However, it is a very small thickness-to-chord ratio and a very high lift at the optimum angle of attack, which would result in very thin dimensions at the tip (this will be confirmed in the next subsection about the chord distribution) . This would be impossible to manufacture by 3D printing and this airfoil was therefore not chosen.

Out of the FX63-137 and the NREL family, we see that the FX63-137 has a better lift-to-drag ratio at high  $Re$  but its performance at low  $Re$  is quite similar to the S834 (the only airfoil from the NREL family with reliable experimental data). Moreover, the thickness-to-chord ratio of the S834 is higher than that of the FX63-137. That is why we chose the NREL family for our first rotor. But then, after testing it, we realized that this first rotor was very tough so we decided to build a second rotor with the FX63-137 airfoil to compare them experimentally. From the experimental results of these airfoils, the rotor based on the FX63-137 should be more efficient.

	S833	S834	S835	SG6040	SG6043	FX63-137
$t/c$	18%	15%	21%	16%	10%	13.66%
$Re_{design}$	$4 \times 10^5$	$4 \times 10^5$	$2.5 \times 10^5$	$2 \times 10^5$	$2.5 \times 10^5$	Unknown
$(C_l/C_d)_{max}$ at $Re = 1 \times 10^5$	(39.4)	47.4	(34.8)	46	59.4	50.8
at $Re = 5 \times 10^6$	(79.9)	79.5	(88.4)	86.6	125.1	109.8

Table 3.1: Airfoil comparison

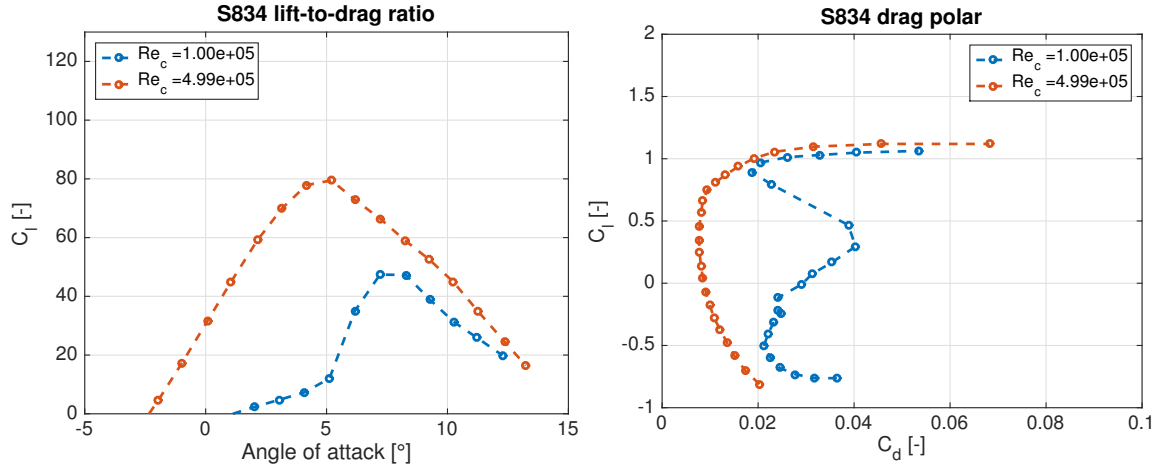


Figure 3.12: S834 lift-to-drag ratio and drag polar (data from [29])

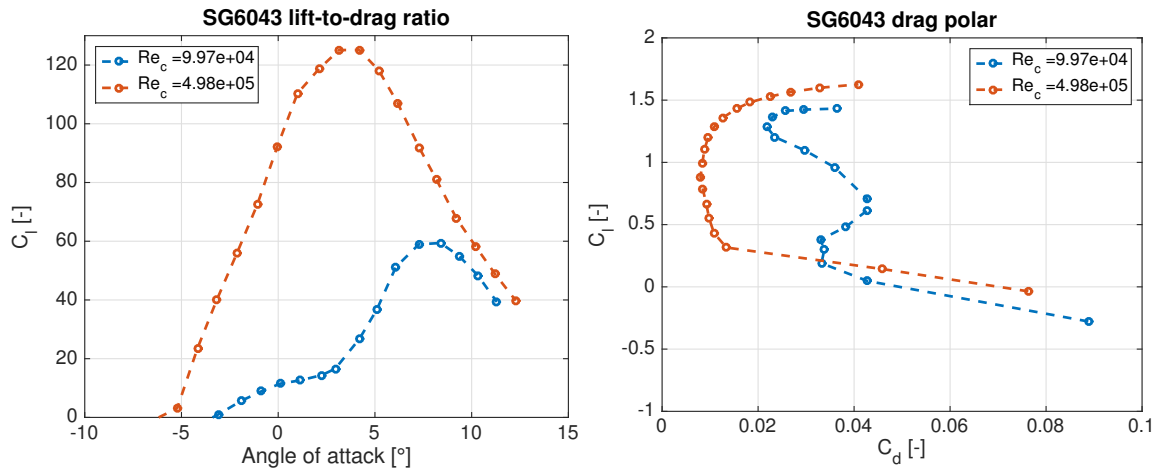


Figure 3.13: SG6043 lift-to-drag ratio and drag polar (data from [44])

### 3.3.2 Chord and twist distribution

The lift-to-drag ratio of an airfoil varies with its angle of attack. There is one angle of attack  $\alpha_d$  for which this ratio is maximized. The flow of each blade element should be at this angle of attack to maximize the torque produced. The relative speed of the flow to each blade element becomes more and more tangential as we move closer to the tip of blade because of the tangential component  $\Omega r$ . As a result, the blade must be twisted.

For the blade to operate optimally, the circulation must be uniform. The circulation is related by the Kutta-Joukowski:

$$L = \rho V_t \Gamma$$

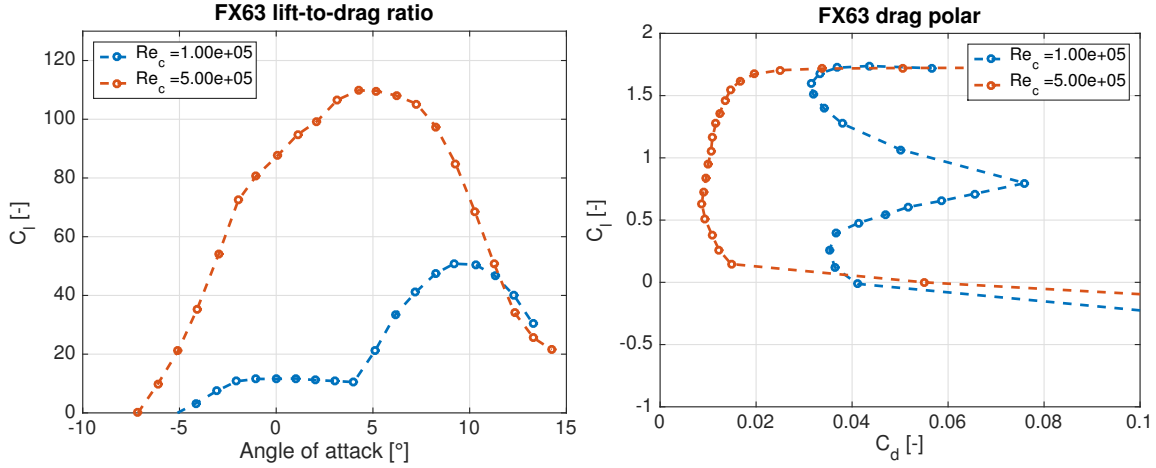


Figure 3.14: FX63 lift-to-drag ratio and drag polar (data from [29])

For the circulation to be uniform, we must regulate the lift production along the blade by varying the chord of the blade elements. An analytical method is developed in Burton et al. [10] :

$$\frac{c}{R} = \frac{1}{B C_{l,opt} \lambda_d} \frac{16\pi}{9\sqrt{4/9 + (\lambda_l + 2/(9\lambda_l))^2}} \quad (3.21)$$

$$\phi = \frac{2}{3\lambda_l + 2/(3\lambda_l)} \quad (3.22)$$

$$\beta = \alpha_d - \phi \quad (3.23)$$

where  $B$  is the number of blades,  $\alpha_d$  is the angle of attack at which the lift-to-drag ratio is maximized and  $C_{l,opt}$  is the lift coefficient at this point,  $\lambda_l$  is the local TSR and  $\lambda_d$  is the design TSR (the lambda at which the blade is supposed to be optimized).

The design TSR was chosen to fit the rotor characteristics (rotational speed and torque) to the generator Maxon BLDC (see chapter 4 for further details). We used  $\lambda_d = 3$ .

To make sure these distributions are efficient, we used them on the example of section 3.2.9 for a design TSR. The distribution of axial induction factor and angle of attack along the blade are visible on Figure 3.15. We observe that the angle of attack is constant along most of the blade and the induction factor is very close to the Betz optimum ( $a = 1/3$ ) excepted at the tip of blade when tip losses are taken into account in the BEM simulation. This was expected as those distributions were developed from a simplified case without tip losses [10]. We conclude that these distributions are sufficiently efficient for our prototype. We applied those equations to design our two rotors and we obtained the curves of Figure 3.16.

### 3.3.3 Number of blades optimization

The last step in the design of our rotor is the choice of the number of blades. We simulated the power coefficient of a rotor with a varying number of blades (see Figure 3.17). For each number of blades, the shape of the blades was optimized by the relations defined in the last subsection. We noticed that increasing the number of blades increased the power coefficient but with diminishing returns. Moreover, the shape of the blades predicted by the chord and twist distributions was very wide for low numbers of blades (between one and 3). We then decided to build a rotor with 5 blades.

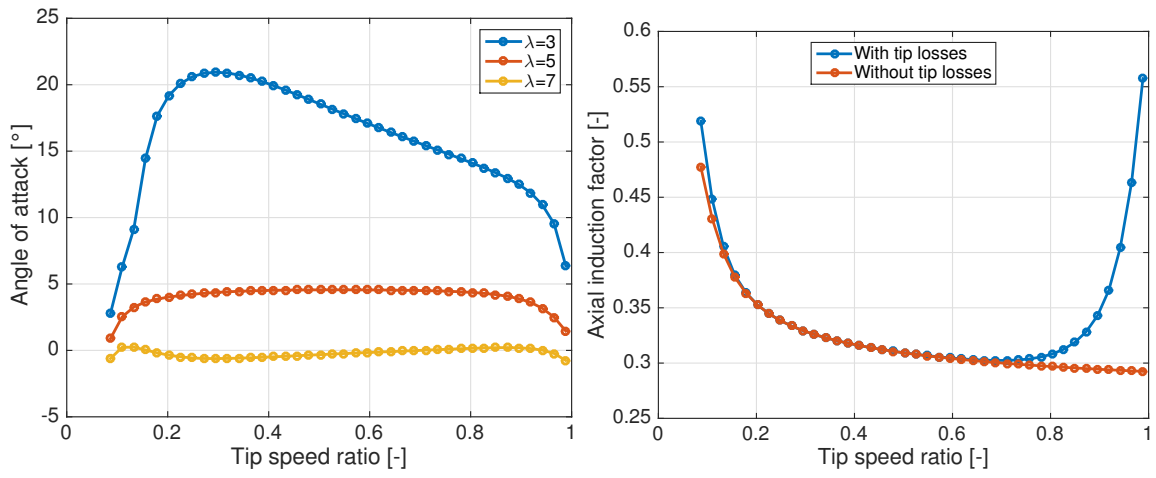


Figure 3.15: Optimal distribution of chord and twist: angle of attack and induction factor along the blade

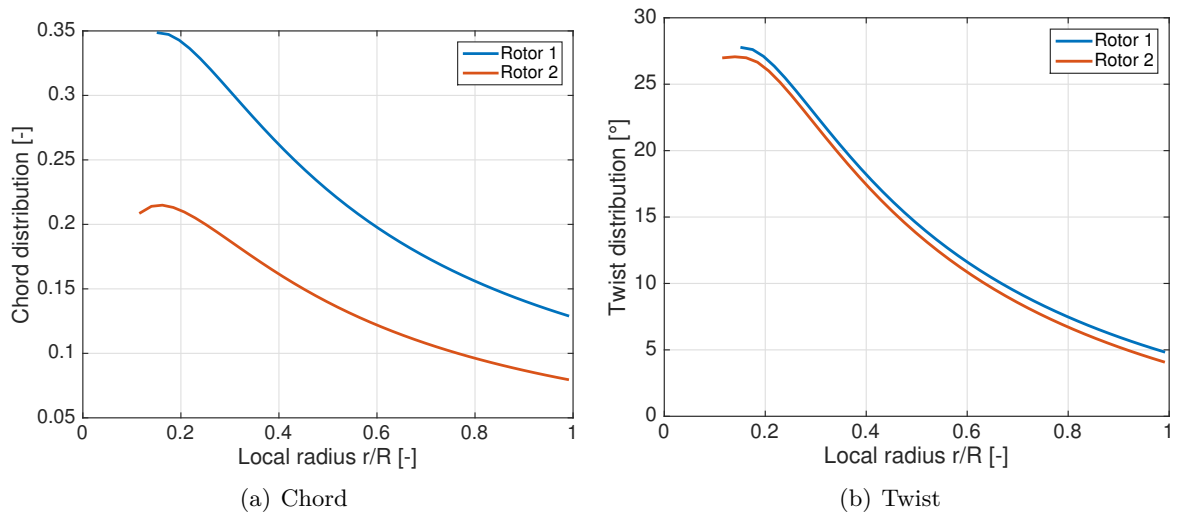


Figure 3.16: Twist and chord distributions

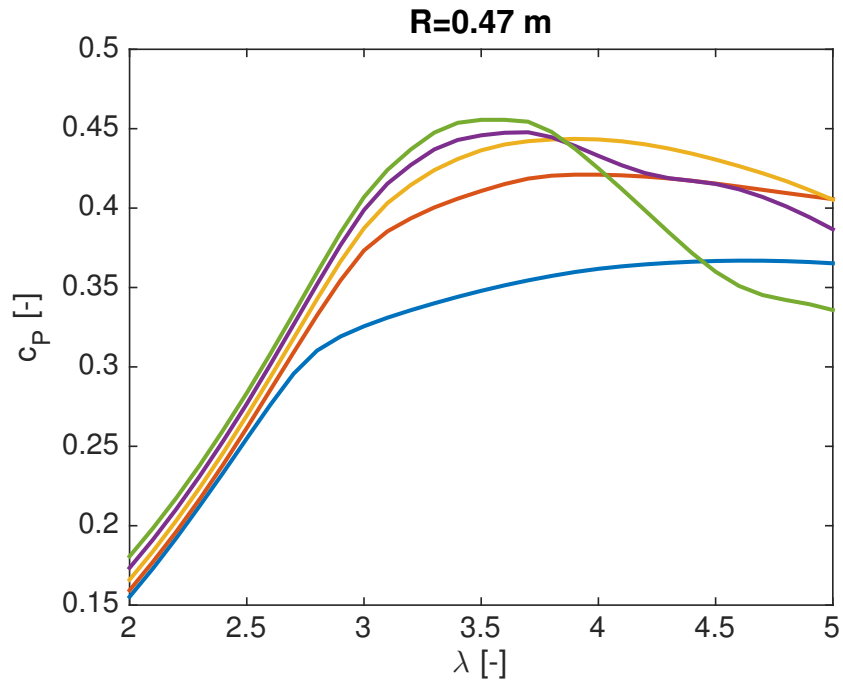


Figure 3.17: S834: number of blades influence on power coefficient

### 3.4 Numerical power prediction of the rotors

For future comparison with experimental results, we simulated the rotors we designed with our BEM method. The results are in Figure 3.18 and Figure 3.19.

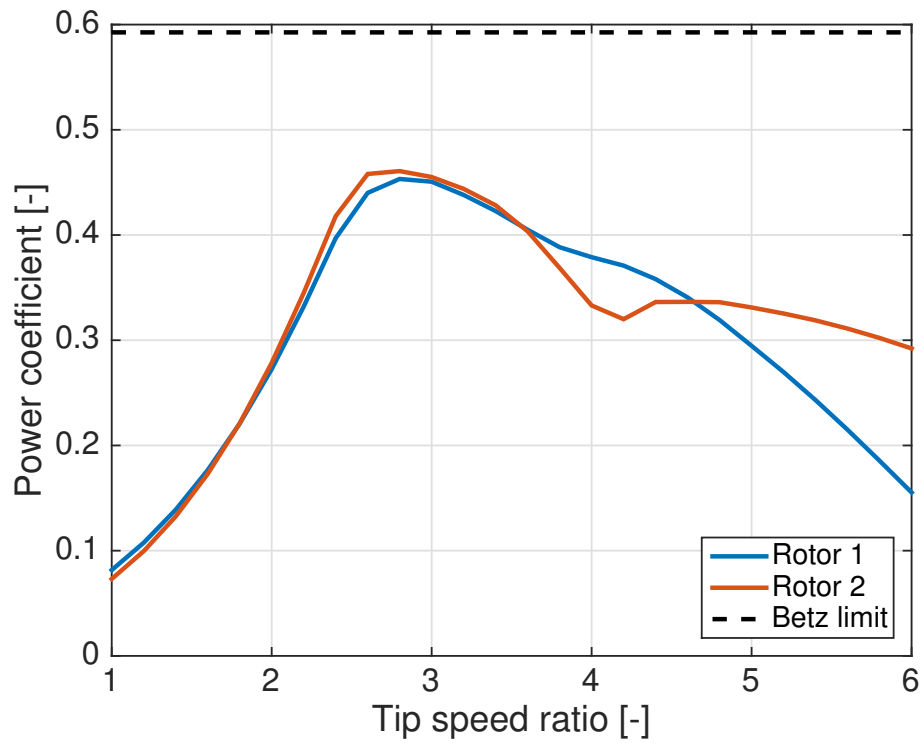


Figure 3.18: Designed rotors: prediction of power coefficient

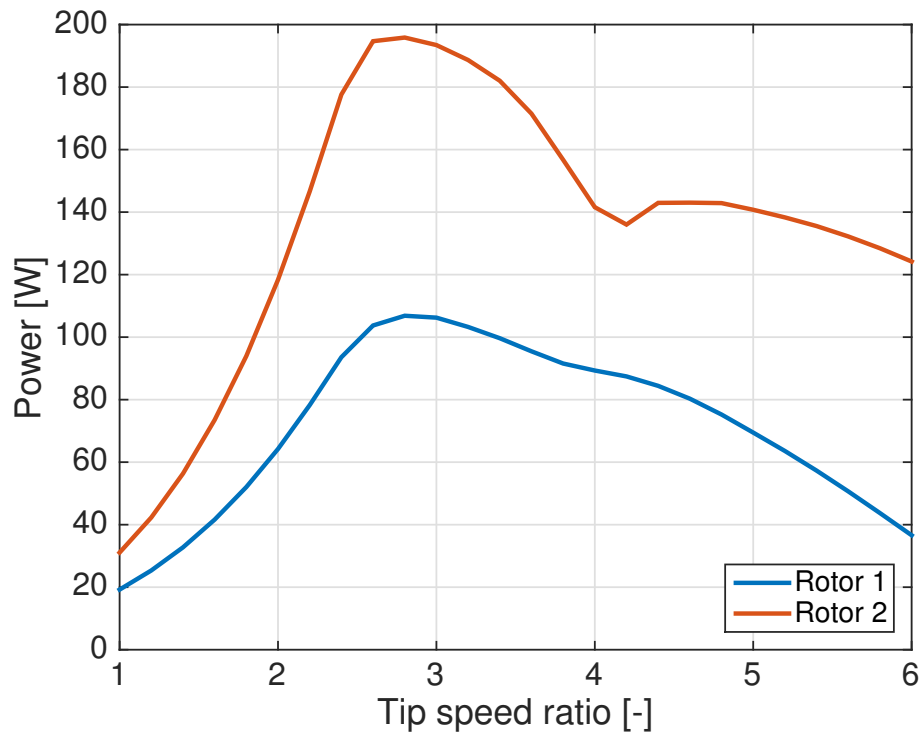


Figure 3.19: Designed rotors: prediction of power produced

### 3.4.1 Blade roots

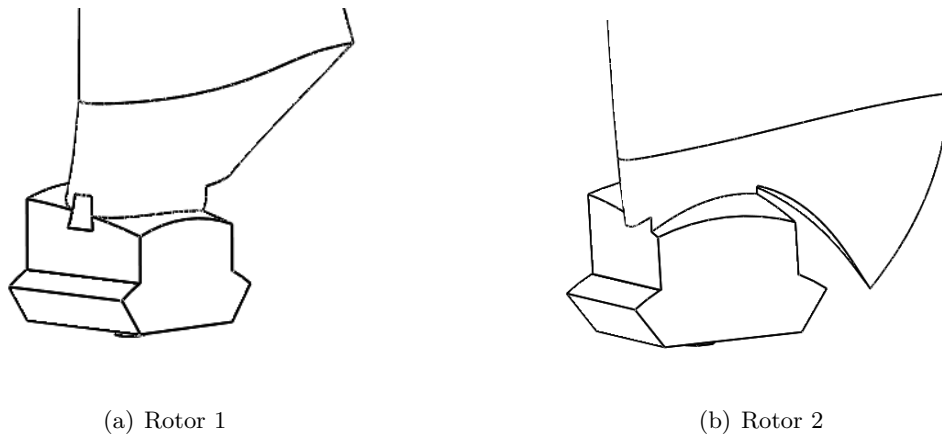


Figure 3.20: Shape of the blade roots (CAD file)

If we extend the blade to the rotor with the chord and twist distribution of section 3.3.2, the shape of the blade clashes with the hub. We have to modify the optimal shape at the root to avoid this. Most large-scale wind turbines use a circular shape at the root for structural reasons. That is the solution we used for our first rotor (see Figure 3.21). This solution is very simple but not the most efficient: it allows the shedding of a vortex at the hub because of the sudden change in shape. For the second rotor, we decided to extend the blade so that it closely fits the hub. This way the hub provides a wall effect which limits the vortex shedding. It also provides a better starting torque because when the rotor is still, most of the torque is produced by the part of the blade close to the root.

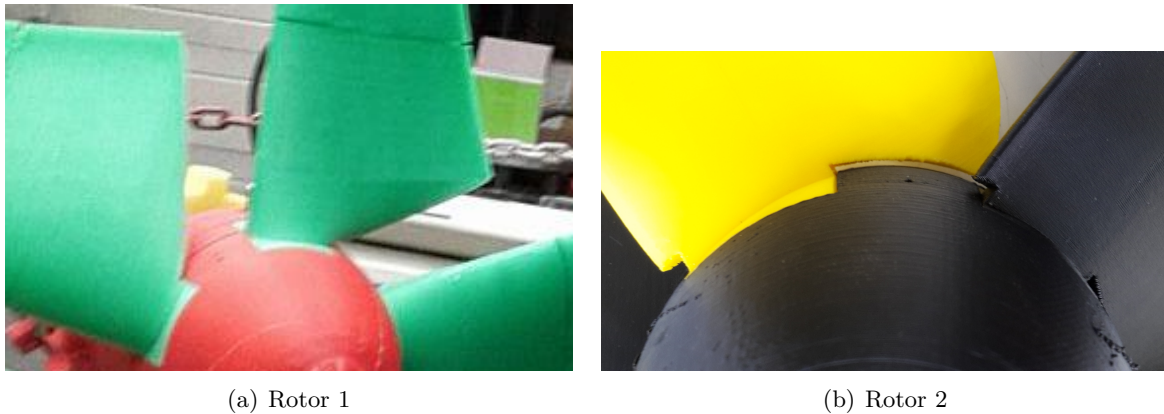


Figure 3.21: Shape of the blade roots (prototype)

### 3.5 Yaw system: tail fin

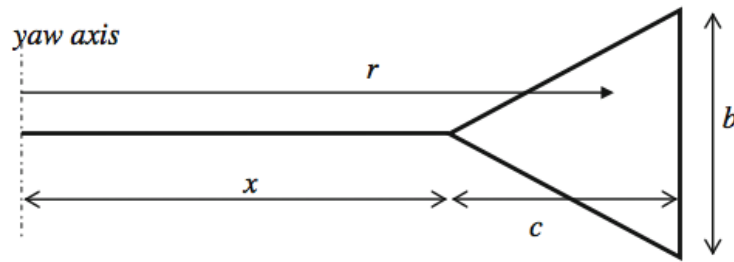


Figure 3.22: Geometry of a delta wing tail fin [57]

In real conditions, the wind is never a steady flow but its direction and force vary continuously. In order to produce the most power possible, a wind turbine always face the wind. The yaw system is the component of the wind turbine responsible for adjusting the nacelle of the wind turbine towards the wind. That is why a yaw bearing is always required between the tower and the nacelle.

Large sized wind turbines use an active yaw system: they measure the wind direction with a sensor and use a motor to adjust the orientation of the nacelle. However, this system is impractical for small wind turbines because of the cost and the size of this solution. Small wind turbines use a passive yaw system, they use the force of the wind to produce a corrective torque and reorientate the nacelle in the right direction. There are two types of passive yaw systems:

- tail fin: A flat plate (called the tail fin) is mounted at some distance behind the nacelle. When the wind changes of direction, the angle of attack on the flat plate creates a torque on the nacelle which reorientates it.
- downwind rotor: Instead of being in front of the nacelle, the rotor is now behind it. A torque is directly created on the rotor whenever the wind is not perfectly orientated towards the rotor.

The downwind rotor can accelerate blade fatigue failure because of the "tower shadow" effects: the cyclic thrust and torque applied on the blades at each rotation behind the tower. Moreover, the tail fin is more widespread in existing small wind turbines and has well-known characteristics. That is why it is the solution we chose for our yaw system. There are many tail fin designs but the delta wing (see fig. 3.22) is often preferred for its high stall angle and its well-known aerodynamic characteristics [57]. The tail fin should be designed to produce a corrective torque high enough for the size of the wind turbine but also to follow only "low frequency" wind direction changes ("high frequency" wind direction changes induce high gyroscopic loads). Unfortunately this is outside the scope of our work and was not studied.

### 3.6 Diffuser augmented wind turbine

A diffuser augmented wind turbine (DAWT) is equipped with a diffuser around its blades to increase the wind speed across it (see table A.1). As the power output of a wind turbine is proportional to the cube of the wind speed, theoretical gains can seem attractive. But such a structure is complicated to design, especially in 3D printing (see chapter 5). It can be very

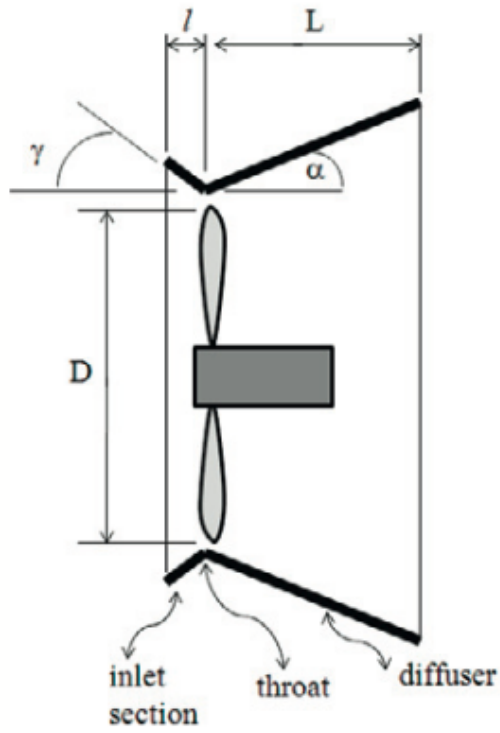


Figure 3.23: Diffuser augmented wind turbine (from [26])

heavy and we were not convinced it would be useful for a very small wind turbine that needs to continuously align itself with the wind.

## Chapter 4

# Generator design

The part of the wind turbine which produces electrical power from the mechanical power is the generator. For the wind turbine to be optimized, the nominal torque and rotational speed of the generator must match the characteristics of the rotor. Indeed, the optimized operating point is reached while the generator efficiency is maximum.

Nowadays there are two types of generators for large-scale wind turbines: doubly-fed induction generators (DFIG) and permanent magnet synchronous generators (PMSG). With the advances in power electronics they are combined with full scale power converters (a combination of a controlled thyristor rectifier and a controlled inverter) and are able to both regulate the rotational velocity of the wind turbine, as well as provide power quality advantages to the grid such as: reactive power compensation, energy storage, etc.

For small wind turbines, the constraints of simplicity and price are more important. That is why a lot of early designs re-used DC motors as generators. These motors are equipped with brushes that wear out so they are not an optimal choice. Moreover they are often poorly adapted for a use in a wind turbine and require the use of a gearbox.

Actual designs generally use permanent magnet synchronous generator (PMSG). Advantages in comparison with DC generators are multiples: higher lifespan (no brushes), easier to create (concentrated windings instead of distributed windings), smaller ripple torque, higher speed range [35]. Furthermore PMSG can contain a numerous poles pairs. The use of a gearbox is then no more necessary what highly increases the total efficiency.

To create our prototype, we rapidly needed a generator. We then searched an existing generator available at the UCL that more or less matches our rotor characteristics. The first part of this chapter gives and explains the characteristics of this off-the-self solution.

To create a adapted home-made generator, the choice of a PMSG configuration is developed in the second part of this chapter. The choice of the generator type is explained. Tools are also developed to permit a pre-design.

### 4.1 Off-the-shelf solution

The machine used in our prototype is a brushless DC motor re-used as a generator. It possesses three parts: a gearbox that reduces the torque and increases the rotational speed at the generator input, the generator itself that transforms mechanical in electrical power, an encoder that allows us to know the rotational speed during the tests (see Figure 4.1).

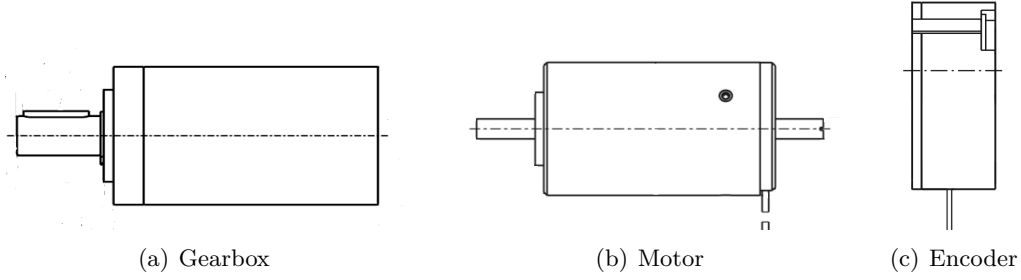


Figure 4.1: Maxon BLDC motor: schematic representation

#### 4.1.1 Characteristics

The main characteristics of the Maxon BLDC motor and the gearhead GP42C can be found in Table 4.1.

Maxon BLDC EC40		
Nominal power [W]	$P_{gen,n}$	120
Nominal torque [Nm]	$T_{gen,n}$	0.122
Nominal rotational speed [rpm]	$\Omega_{gen,n}$	9290
No load rotational speed [rpm]	$\Omega_{gen,nl}$	10400
Max. <b>motor</b> efficiency [-]	$\eta_{gen,max}$	0.84
Nominal voltage [V]	$U_{gen,n}$	42
Nominal current [A]	$I_{gen,n}$	3.4
No load current [A]	$I_{gen,nl}$	0.258
Torque constant [mNm/A]	$k_\phi$	38.2
Winding arrangement		Y
Phase resistance [ $\Omega$ ]	$R_{ph}$	0,625
Thermal resistance housing-ambient [K/W]	$R_{h-a}$	3.2
Thermal resistance winding-housing [K/W]	$R_{w-h}$	1.2
Planetary gearhead GP42C		
Gear ratio [-]	$n$	49 : 4
Max. efficiency [-]	$\eta_{red,max}$	0.81

Table 4.1: Maxon BLDC EC-40 and planetary gearhead characteristics (from [14])

The theoretical values calculated on the basis of the BEM method are given in Table 4.2.

	Symbol	Rotor1	Rotor2
Nominal power [W]	$P_{sys,n}$	106.8W	195.8W
Nominal torque [Nm]	$T_{sys,n}$	1.33	3.28
Nominal rotational speed [rpm]	$\Omega_{sys,n}$	763	568

Table 4.2: Rotors characteristics

To compare our designed rotors with the Maxon generator, we calculate the nominal torque and the nominal rotational speed at the output of the gearhead:

$$T_{g,out} = T_{gen,n} \cdot n = 1.49Nm$$

$$\Omega_{g,out} = \frac{\Omega_{gen,n}}{n} = 758.4rpm$$

Because the machine is originally a motor, the datasheet gives values in a motor configuration. We must compute the nominal mechanical power in a generator configuration. The maximum electrical power is known:

$$P_{elec,max} = U_{gen,n} \cdot I_{gen,n} = 142.8W$$

with losses calculated in section 4.1.2 and the gearhead efficiency, we can then find the maximum mechanical power:

$$P_{meca,max} = \frac{P_{elec,max} + P_{los,max}}{\eta_{red,max}} = 209.9W$$

In terms of powers, the maximal permitted power at the gearhead output is above the theoretical power of both rotors. The nominal torque and rotational speed of the first rotor are very similar to the ones at the gearhead output. For the first rotor, the Maxon motor matches then perfectly. For the second rotor, there is a huge problem of torque. Indeed, the nominal torque is more than twice the permitted torque. For this rotor, we thus won't be allowed to reach the nominal power (see section 6.4).

#### 4.1.2 Generator efficiency

The electric power produced by the generator can be measured. Then, to be able to find the mechanical power produced by the wind turbine and the power coefficient  $C_P$ , the efficiency of the generator have to be known.

In a generator, the main losses are the copper and friction losses:

$$P_{los} = P_{cop} + P_{fr}$$

with  $P_{los}$  the total losses,  $P_{cop}$  the copper losses and  $P_{fr}$  the friction losses. The efficiency of the generator is:

$$\eta_{gen} = \frac{P_{elec}}{P_{meca}} = \frac{P_{elec}}{P_{elec} + P_{los}} = \frac{P_{elec}}{P_{elec} + P_{cop} + P_{fr}}$$

Thus, as we are able to measure the electric power, the only unknowns are the losses. The datasheet contains useful informations to deduce them. The data is given for the motor configuration. We make then the hypothesis that the losses are similar for a use in generator or in motor.

When it is used as a motor, the tensions in a BLDC have the forms shown in Figure 4.2. The current pass through two of the three phase resistances at the same time. The copper losses are then:

$$P_{los} = 2R_{ph}I_{ph}^2$$

with  $R_{ph}$  the phase resistance (its value is given in the datasheet:  $R_{ph} = 0.625\Omega$ ) and  $I_{ph}$  the phase current. The phase current is also the line current as the windings are wye-connected.

The friction losses can be calculated with the friction torque  $T_{fr}$  and the rotational speed  $\omega$ :

$$P_{fr} = T_{fr} \cdot \omega$$

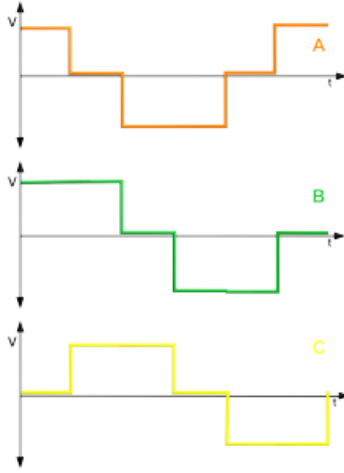


Figure 4.2: Voltage in a BLDC motor [15]

The friction torque is separated in two parts: dry friction and kinetic friction. Dry friction is the torque necessary to put the generator in rotation from rest. It is thus independent of the rotational speed. On the contrary, kinetic friction is dependent on the rotational speed.

With the data given in the datasheet, we can determine the friction torque for two different rotational speed: at nominal speed and at no load speed. With these two points, we want to deduce the friction torque for any rotational speed. To solve this problem, we make the hypothesis that the kinetic friction is mainly dependent on the rotational speed square. The friction torque has then the following form:

$$T_{friction} = a + b \cdot \omega^2$$

Lets find now the friction torque at nominal and no load speed:

- At nominal speed, the nominal current, voltage and power are known. The nominal losses are:

$$P_{los,n} = U_{gen,n} \cdot I_{gen,n} - P_{gen,n} = 22.8W$$

We can also calculate the nominal copper losses:

$$P_{cop,n} = 2R_{ph} \cdot I_{gen}^2 = 14.45W$$

The nominal friction losses are then:

$$P_{fr,n} = P_{los,n} - P_{cop,n} = 8.35W$$

The friction torque at nominal speed is easily deduced:

$$T_{fr,n} = \frac{P_{fr,n}}{\omega_n} = 8.58mNm$$

- At the no load speed, we can calculate the friction torque with two different methods. We will use both and then verify if the equations are correct.

The first method is the same that the one used at the nominal speed. As the motor works without load, there is no mechanical power. No load power losses are then simply:

$$P_{los,nl} = U_{gen,nl} \cdot I_{gen,nl} = 10.836W$$

We calculate the no load friction torque:

$$T_{fr,nl} = \frac{P_{fr,nl}}{\omega_{nl}} = \frac{P_{los,nl} - P_{cop,nl}}{\omega_{nl}} = \frac{P_{los,nl} - 2R_{ph} \cdot I_{gen,nl}^2}{\omega_{nl}} = 9.87mNm$$

For the second method we use the torque constant  $k_\phi$ . While multiplied by the current, this torque gives the electromagnetic torque. As there is no load:

$$T_{em} = T_{fr,nl} = k_\phi \cdot I_{gen,nl} = 9.86mNm$$

The results obtained are almost equals and prove that our resolutions methods are correct

The equation of the friction torque as function of the rotational speed can now be calculated (see Figure 4.3):

$$T_{fr} = 3.5 + 5.38 \cdot 10^{-6} \cdot \omega^2 [mNm]$$

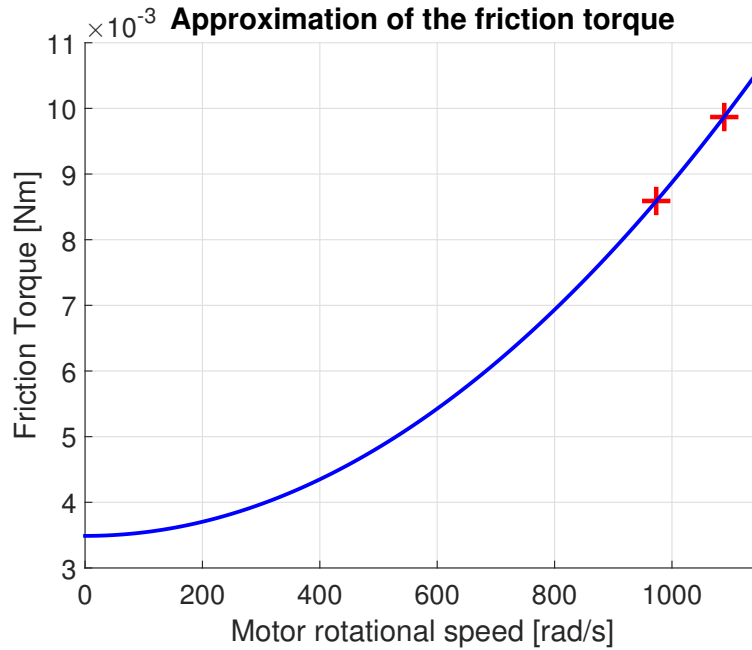


Figure 4.3: Approximation of the friction torque

### 4.1.3 Generator thermal characteristic

In the generator specifications, thermal data are given. We know the thermal resistance between winding and housing ( $R_{w-h}=1.2$  [K/W]) and the thermal resistance between housing and ambient ( $R_{h-a}=3.2$  [K/W]). The maximum permissible winding temperature is 125° C. With these informations, we can calculate the losses we can tolerate in the generator for a 25°C ambient temperature.

A thermal circuit is analogical at an electrical one. Voltage difference is replaced by temperature difference and current is replaced by losses (see figure 4.4). The ambient temperature  $t_w$  and the maximal windings temperature  $t_a$  are known. We can easily calculate the losses:

$$P_{los} = \frac{t_w - t_a}{R_{w-h} + R_{h-a}} = \frac{125 - 25}{1.2 + 3.2} = 22.7W$$



Figure 4.4: Thermal system

On the basis of this result, we want to approximate the maximum power we could produce without exceeding the thermal constraints. We make the hypothesis that the efficiency at this limit point is the same as the nominal one. In generator, electric and mechanic powers are linked by the efficiency:

$$P_{elec} = P_{meca} \cdot \eta_{gen}$$

The maximum electric power can then be calculated:

$$P_{elec} = P_{meca} - P_{los} \Rightarrow P_{elec} = \frac{P_{los}}{1 - \eta_{gen}} = 142W$$

The Maxon BLDC EC-40 is a 120W motor. It signifies that it can produce a mechanical power of 120W. The electrical nominal power is:

$$P_{elec,n} = U_{gen,n} \cdot I_{gen,n} = 142.8W$$

The electrical powers found directly and with the losses are close. The nominal current is then the maximal current in the windings.

To increase the electrical power potentially produced, we have to reduce the windings temperature. Indeed, in our case, it is limiting factor. The thermal resistance between the housing and the ambient given in the data represents the natural convection. By forcing an air flux at the generator surface, we create forced convection and reduce the thermal resistance between housing and ambient. Larger losses are then allowed and the maximum electrical power increase. This amelioration is developed in other chapters (sections 5.4.1 and 6.4.3).

#### 4.1.4 Planetary gearhead efficiency

The gearhead efficiency depends on the number of stages and the torque at gear output. It also is unaffected by the generator speed and is greatly reduced with very small loads (see figure 4.5).

In the datasheet, we find out that the planetary gearhead GP 42C is an one stage piece and has a 81% maximum efficiency. As the efficiency decreases with small torques, we won't use the gearhead in this operating region. We don't have enough informations to calculate the equation of the efficiency in function of the torque. We then make the hypothesis that it is constant and equal to its maximum value near the maximum continuous torque.

This way, we will compute the lower limit of the power coefficient.

## 4.2 Ad-hoc solution

An ad-hoc solution was considered. Due to a lack of time, it was not possible to create this hand-made generator. At the beginning of this part, it will be explained which type of generator

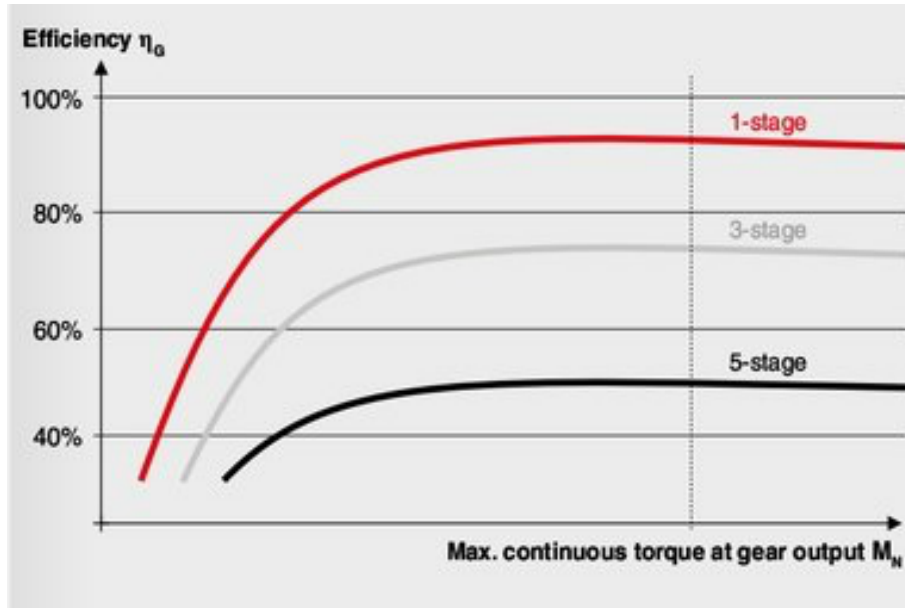


Figure 4.5: Gearhead efficiency as a function of torque (schematic) [31]

we planned to make and the reasons that lead us to this choice. Two methods that can be used for the generator design are then explained: one about the choice of the number of magnets/windings, the other about the thermal model. These developments could be used in a prolongation of this thesis.

#### 4.2.1 Choice of generator type

First of all, we choose to use a synchronous generator with permanent magnet. This is the easiest solution for a hand-made prototype. Indeed, the hardest part to create are the windings. And it is possible to use concentrated windings in PMSG. It is easier to wind that distributed windings used for example in DC generator. Another advantage is that we don't need brushes or a complicated system of electronic control.

For the permanent magnet synchronous generator, it exists 4 different configurations (see fig. 4.6). These propositions vary according to 2 parameters: with or without teeth, with internal or external rotor.

##### Internal rotor with teeth

To characterize the torque, we use the following equation [38]:

$$\frac{T}{c_f \cdot \pi \cdot R^3} = \left(1 - \frac{r^2}{R^2}\right) \cdot \frac{r}{R}$$

where  $c_f = B \cdot J_{max} \cdot l \cdot c_w$ .

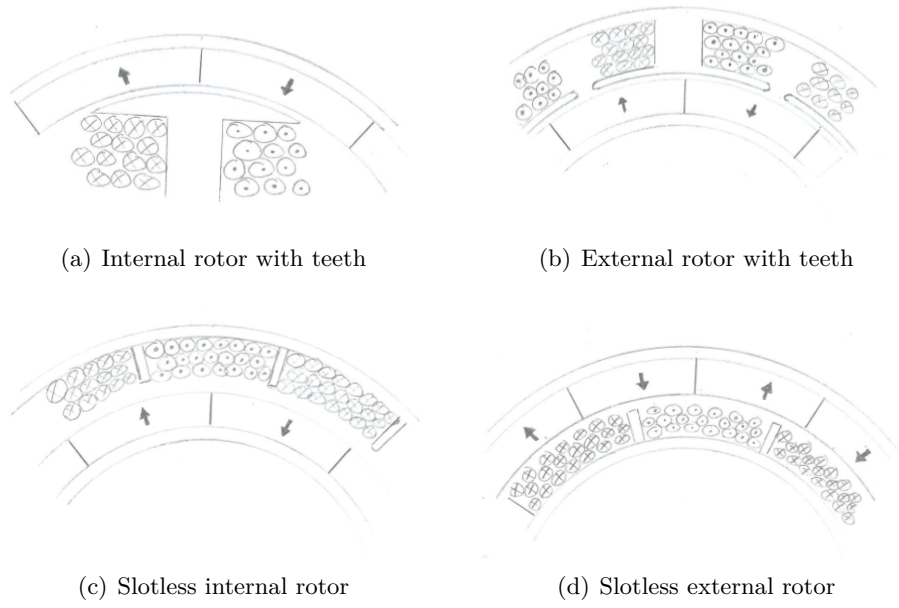


Figure 4.6: Types of PMSG

$$\left\{ \begin{array}{l} B = \text{the magnetic flux density due to the permanent magnets in the air gap} \\ l = \text{length of the machine} \\ J_{max} = \text{the maximum current density in the stator windings} \\ c_w = \text{percentage of the stator area used for the stator windings} \\ R = \text{the outer machine radius} \\ r = \text{the air gap radius} \end{array} \right.$$

The magnetic flux density  $B$  can be considered constant in the air gap. This is true for all type of configuration with all air gap radius. According to the following equation

$$B \approx B_r \cdot \left( \frac{\delta_{PM}}{\delta_{PM} + \delta} \right)$$

the air gap magnetic flux density  $B$  is close to the magnet's remanence  $B_r$  when the magnets thickness is bigger than air gap thickness ( $\delta_{PM} \gg \delta$ ).

### External rotor with teeth

To characterize the torque, we use the following equation [38]:

$$\frac{T}{c_f \cdot \pi \cdot R^3} = \frac{r^3}{R^3}$$

where  $c_f = B \cdot J_{max} \cdot l \cdot c_w$ .

The parameters are the same that the ones used for the internal rotor.

### Slotless internal rotor generator

In this case torque cannot be calculated like for rotors with slots. Indeed, the magnetic flux density  $B$  can't be assumed to be constant in the air gap. To calculate it we start with the

definition of a torque induce on windings:

$$T_{em} = \frac{\partial W_{cmag0}}{\partial \theta_m} + \sum_{k=1}^n \frac{\partial \psi_k}{\partial \theta_m} + \frac{1}{2} \sum_{k=1}^n \sum_{j=1}^n \frac{\partial L_{kj}}{\partial \theta_m} i_k i_j$$

As we don't have windings in the rotors and so no mutual inductances, the ultimate term can be suppressed. The first term is the cogging torque. As there are no slots there is no cogging torque. The first term can then be neglected. We then obtain the following equation:

$$T_{em} = \sum_{k=1}^n \frac{\partial \psi_k}{\partial \theta_m}$$

To find the torque, we so have to sum all the variations of the magnetic field flux of all windings. We cannot solve this problem easily. A resolving way is to use the simulation software *COMSOL*. We created a parametric model that allow to find the magnetic field for any position of the designed generator (see Figure 4.7). This simulation is a basis that can be improved with a view to make the pre-design of the PMSG generator.

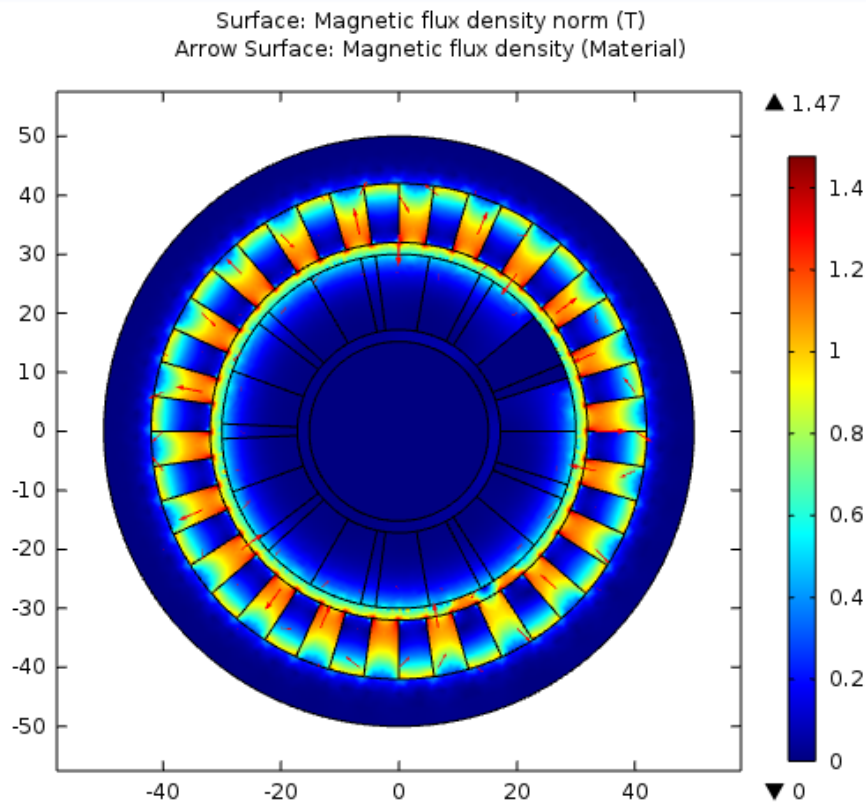


Figure 4.7: Magnetic field for a given position

### Slotless external rotor generator

The same approach can be use for this case than for the previous one.

## Comparisons and choice

The advantages about internal/external rotor and with slots/slotless generator are given in Tables 4.3 and 4.4.

We want a generator easy to produce with a sufficient torque. Furthermore we prefer a generator with the lowest cogging torque possible to allow a quicker start for our wind turbine. And as the cooling won't be very restrictive (see section 4.2.3), we choose a slotless generator with outer rotor.

	Advantages
with slot	<ul style="list-style-type: none"> <li>• Air gap magnetic flux density easier to produce ⇒ cheaper magnets</li> <li>• Air gap magnetic flux easy to find</li> <li>• Easy approximation of torque</li> </ul>
slotless	<ul style="list-style-type: none"> <li>• Reduced ripple</li> <li>• Easier to create manually</li> <li>• Allow a more compact generator</li> <li>• No cogging torque</li> <li>• Better electricity quality ( induced emf without harmonics)</li> <li>• reduced damping losses ( due to eddy currents)</li> <li>Higher lifespan</li> </ul>

Table 4.3: Comparison between slot and slotless generator

	Advantages
Internal rotor	<ul style="list-style-type: none"> <li>• Better cooling because windings on the exterior</li> </ul>
External rotor	<ul style="list-style-type: none"> <li>• Allow more poles and so higher torque <b>true?</b></li> </ul>

Table 4.4: Comparison between internal and external rotor

## Summary

Here is a summary of the chosen generator characteristics:

- axial flux permanent magnet synchronous generator (brushless and no power needed to start the generator)
- rotor:
  - outer rotor (directly attached to the hub (see section 5.3.2), higher torque concentration [38], centrifugal forces keep the magnets in place)
  - high number of pole pairs
  - Hallbach magnet network (flux concentrated in the airgap)
- stator:
  - 3-phased (standard)
  - double layer fractional slot concentrated windings (easier to manufacture, shorter end windings)

- slotless (low cogging torque and easier to manufacture)
- steel tube used as back iron

#### 4.2.2 Number of windings/magnets

To find the right number of magnets and windings/poles, we have to create balanced windings. In other words, we have to find a windings-poles combination in which the coils are arranged in such a way that they produce a symmetrical system of equally time-phased displaced emf's of identical magnitude, frequency and waveform. The possible windings-poles combinations fit the following equation [37]:

$$\frac{W}{CGD(W, 2p)} = 3k$$

where the parameters are:

- W: number of windings
- p: number of poles pairs
- k: a numerical integer

All the possible combinations are present on Figure 4.8. The values in parenthesis are the  $k_w$  coefficient for fractional slot concentrated windings machines.  $k_w$  is the winding coefficient and is defined as the ratio between the flux embraced by each turn and the flux produced by the excitation mmf. It is a performance coefficient. The higher it is the better it is. In our case, we create a slotless generator. We make then the hypothesis that the relation between slot and slotless can be considered as proportional.

To make a selection of numbers of windings and magnets, a high  $k_w$  factor has to be chosen. It must be paid attention to the generator size because we can't make it as large as we want. Indeed, it cannot be bigger than the hub (see section 5.3.2).

For determining the windings order, the number of windings per poles and per phase has to be calculated :

$$W_{pp} = \frac{W}{2p \cdot m} = \frac{1}{5}$$

According to the method used in [37], a repeatable sequence as to be made with a number of "1" equal to  $W_{pp}$  numerator and a number of "0" equal to  $W_{pp}$  denominator. The more regular is the sequence the higher are the generator performances. It has then to be repeated three times. Below the sequence found, the usual phase sequence is put. Of this usual phase sequence, we only take the ones below a "1". The return winding is then put at the side of the going winding. The final sequence obtained has to be repeated the number of times necessary to get all our windings position.

An example of this method has been made for  $S_{pp} = 3/7$  in Table 4.5. On the basis of the last table line, the final sequence is AA'-BB'-CC'-C'C-A'A-B'B-BB'-CC'-AA'.

TABLE I  
COMBINATIONS OF NUMBER OF SLOTS ( $S$ ) AND POLES ( $2p$ ) ALLOWING THE REALIZATION OF THREE-PHASE MACHINES  
WITH A BALANCED CONCENTRATED WINDING

$S \backslash 2p$	2	4	6	8	10	12	14	16	18	20	22	24
3	1/2 .866	1/4 .866		1/8 (.866)	1/10 (.866)		1/14 (.866)	1/16 (.866)		1/20 (.866)	1/22 (.866)	
6		1/2 .866		1/4 (.866)	1/5 (.866)		1/7 (.866)	1/8 (.866)		1/10 (.866)	1/11 (.866)	
9			1/2 .866	3/8 .945	3/10 .945	3/12 (.866)	3/14 (.945)	3/16 (.945)		3/20 (.945)	3/22 (.945)	
12				1/2 .866	2/5 .966		2/7 (.966)	1/4 (.966)		1/5 (.866)	2/11 (.966)	
15					1/2 .866		5/14 .866	5/16 .866		1/4 (.866)	5/22 (.951)	
18						1/2 .866	3/7 .945	3/8 .945		3/10 .945	3/11 (.902)	1/4 (.866)
21							1/2 .866	7/16 .932		7/20 .953	7/22 .953	
24								1/2 .866		2/5 .966	4/11 .957	

Figure 4.8: Combinations slots-poles allowing balanced concentrated windings [37]

1	0	1	0	1	0	0	1	0	1	0	1	0	0	1	0	1	0	1	0	0
A	C'	B	A'	C	B'	A	C'	B	A'	C	B'	A	C'	B	A'	C	B'	A	C'	B
A		B		C			C'		A'		B'			B		C		A		

Table 4.5: Resolution of the windings sequence

### 4.2.3 Thermal model

When a torque is applied to the generator, a current is induced in the windings. This creates copper losses which increase the temperature of the windings. Therefore the torque is limited by the maximum temperature of the windings. Moreover, in our assembly, some materials can't exceed some operational temperature. A magnets temperature bigger than 80°C will cause irreversible demagnetisation. ABS and windings respectively melt with a temperature that exceeds 108°C and 180°C. These reasons forced us to develop a thermal model. Thanks to it, we will be able to see if the generator works in a safe range of temperatures. First of all, we will explain the hypotheses and the model that we will use for our simulation. To develop it, we based this model on Nerg, Rilla and Pyrhonen [32].

#### Hypotheses and model

To simplify the problem, we make the following hypotheses:

- All the elements can be approximated by a cylinder that may be hollowed (see figure 4.9)
- radial and axial flux are independent
- the flux are constant
- the losses are constant and uniform in the simulated element

We will use thermal resistances to solve the 3D problem. The equivalent representation of an element is represented on Figure 4.10. The left part represents the model in T for the thermal

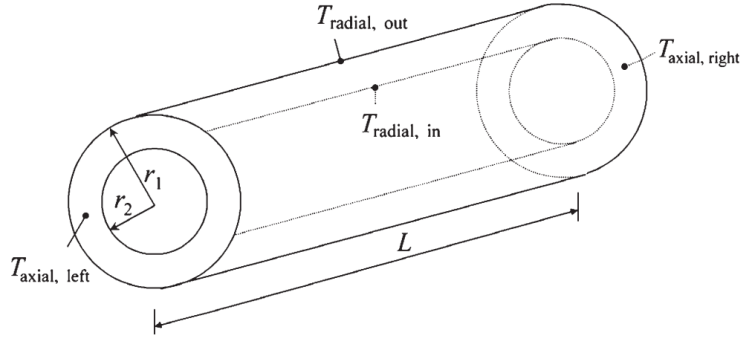


Figure 4.9: Approximation by a cylinder (from [32])

resistances of the axial flux. The right part is for the radial flux.  $T_m$  is the maximal temperature reached by the element.  $q$  is the thermal flux created by the element, for example Joule losses in the windings.

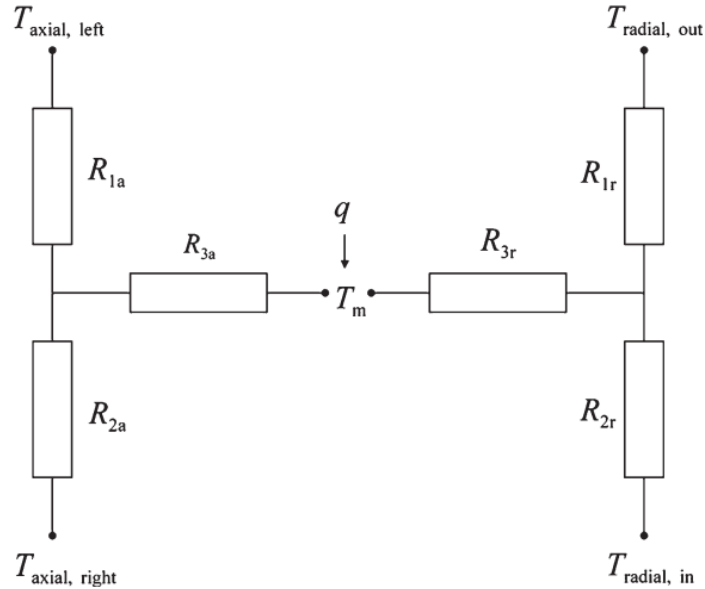


Figure 4.10: Circuit of thermal resistances (from [32])

The definition of thermal resistance is analogous to the electric one and is defined as follows:

$$R_{th} \triangleq \frac{\Delta t}{q} [K/W]$$

With  $\Delta t$  the the difference of temperature between both sides of the thermal resistance.

The heat transfer inside a solid or between solids is conduction. To find the value of thermal resistances that represent the conduction, we start with the heat equation:

$$\rho c \frac{DT}{Dt} = \nabla \cdot q + \epsilon$$

As we are is stationary, we can simplify:

$$0 = \nabla \cdot q + \epsilon$$

After development, we find:

- Axially:

$$- R_{1a} = \frac{L}{2\pi k(r_1^2 - r_2^2)}$$

$$- R_{2a} = \frac{L}{2\pi k(r_1^2 - r_2^2)}$$

$$- R_{3a} = \frac{-L}{6\pi k(r_1^2 - r_2^2)}$$

- Radially:

$$- R_{1r} = \frac{1}{4\pi kL} \left( 1 - \frac{2r_2^2 \ln\left(\frac{r_1}{r_2}\right)}{(r_1^2 - r_2^2)} \right)$$

$$- R_{2r} = \frac{1}{4\pi kL} \left( \frac{2r_1^2 \ln\left(\frac{r_1}{r_2}\right)}{(r_1^2 - r_2^2)} \right)$$

$$- R_{3r} = \frac{-1}{8\pi kL(r_1^2 - r_2^2)} \left( r_1^2 + r_2^2 - \frac{4r_2^2 r_1^2 \ln\left(\frac{r_1}{r_2}\right)}{(r_1^2 - r_2^2)} \right)$$

The winding part has to be homogenize because they are composed of different materials. Each thread has a copper part and a sheath part. We represent these threads by concentric cylinders as shown on Figure 4.9. We observe that:

- Axially: thermal resistances are in parallel  $\Rightarrow$  thermal conductivities are in series

$$k_x = \alpha_1 k_1 + \alpha_2 k_2$$

- Radially: thermal resistances are in series  $\Rightarrow$  thermal conductivities are in parallel

$$k_r = k_1 \frac{1 - \alpha_1 \frac{k_1 - k_2}{k_1 + k_2}}{1 + \alpha_1 \frac{k_1 - k_2}{k_1 + k_2}}$$

where  $\alpha$  is the relation between areas of concentric cylinders:

$$\alpha_2 = \frac{r_2^2}{r_1^2} \quad \text{and} \quad \alpha_1 = \frac{r_1^2 - r_2^2}{r_1^2} = 1 - \alpha_2$$

We also have to add thermal resistances for the convection. Indeed, we have a convection between the external side of the rotor and the air. The wind is there a cooling fluid and the convection depends on its speed. There also is convection in the gap between the stator and the rotor. This convection can be forced in the case of use of a cooling fluid. The equation for this thermal resistance is:

$$R_{conv} = \frac{1}{h_{conv} A}$$

With  $h_{conv}$ , the convection coefficient and  $A$ , the contact area

To find the value of  $h_{conv}$ , we use the following equation:

$$Nu = \frac{h_{conv}d_h}{k}$$

With  $k$  the thermal conductivity of the fluid, the hydraulic diameter  $d_h = \delta\sqrt{83}$  and  $\delta$  the radial length of the air gap.

According to [32, 7], we can determine  $Nu$  thanks to different equations, depending on the case of study:

- If we use a cooling fluid that we will inject into the air gap, the heat is mainly transferred to the fluid. Moreover, the convection is accentuated by the rotational speed that intensify the convective heat transfer. In this case, we use the following equations:

$$Nu = 0.0214(Re^{0.8} - 100)Pr^{0.4}\left(1 + \left(\frac{d_h}{L_\delta}\right)^{0.66}\right)$$

$$Re = \frac{\rho v_{red}d_h}{\mu}$$

$$v_{red} = \sqrt{\left(\frac{\omega R}{2}\right)^2 + v_{axial}^2}$$

with  $Re$  the Reynolds number,  $Pr$  the Prandl number,  $L_\delta$  the axial length of the air gap,  $\rho$  the mass density of the cooling fluid,  $\mu$  the dynamic viscosity of the cooling fluid,  $v_{red}$  the reduced velocity in the helical direction in the air gap,  $\omega$  the angular velocity of the rotor,  $R$  the inner radius of the rotor and  $v_{axial}$  the axial velocity of the cooling fluid.

- When we don't use a forced gas flow, the main heat transfer is in the radial direction. Without this cooling gas, we are in a Taylor-Couette flow. In this case, we calculate the convection heat transfer with the Taylor number:

$$Ta = \frac{\rho^2 \omega^2 r_m \delta^3}{\mu^2}$$

To match the convection heat transfer with our topology, air gap length and rotor radius, we use a modified Taylor number:

$$Ta_m = \frac{Ta}{F_g}$$

With

$$F_g = \frac{\pi^4 \left[ \frac{2r_m - 2.304\delta}{2r_m - \delta} \right]}{1697 \left[ 0.0056 + 0.0571 \left( \frac{2r_m - 2.304\delta}{2r_m - \delta} \right)^2 \right] \left[ 1 - \frac{\delta}{2r_m} \right]}$$

where  $r_m$  is the average of the rotor and stator radii.

We inject the  $T_m$  found in the Nusselt correlation to find  $h_{conv}$ :

$$\begin{aligned} - Nu &= 2 & (Ta_m < 1700) \\ - Nu &= 0.128Ta_m^{0.367} & (1700 < Ta_m < 10^4) \end{aligned}$$

$$- Nu = 0.409Ta_m^{0.241} \quad (10^4 < Ta_m < 10^7)$$

The radiation heat transfer can also be modelled by thermal resistances but is negligible in our case. Adding it would also vainly complicate the model.

Now that we know how create the circuit of thermal resistances and that we are able to give them numerical values, we can find the solutions of the thermal analyse. To solve the system, we first calculate the  $G$  matrix that contains the thermal resistances:

$$\mathbf{G} = \begin{bmatrix} \sum_{i=1}^n \frac{1}{R_{1,i}} & -\frac{1}{R_{1,2}} & \cdots & -\frac{1}{R_{1,n}} \\ -\frac{1}{R_{2,1}} & \sum_{i=1}^n \frac{1}{R_{2,i}} & \cdots & -\frac{1}{R_{2,n}} \\ \cdots & \cdots & \cdots & \cdots \\ -\frac{1}{R_{n,1}} & -\frac{1}{R_{n,2}} & \cdots & \sum_{i=1}^n \frac{1}{R_{n,i}} \end{bmatrix}$$

We can then resolve the system and find the temperature differences between all elements with:

$$\Delta T = G^{-1}P$$

When we use a cooling fluid (it is the case when we inject a flux between the rotor and the stator or when the wind cools the rotor external part), we have to add a  $G_{fluid}$  matrix. This matrix adds the fact that the fluid is moving in our model:

$$\mathbf{G}_{fluid} = \begin{bmatrix} \frac{1}{R_{q11}} & 0 & \cdots & 0 \\ -\frac{1}{R_{q21}} & \frac{1}{R_{q22}} & \cdots & 0 \\ \cdots & \cdots & \cdots & \cdots \\ -\frac{1}{R_{qn1}} & -\frac{1}{R_{qn2}} & \cdots & \frac{1}{R_{qnn}} \end{bmatrix}$$

where

$$R_q = \frac{\Delta T_{average,i}}{P_i} = \frac{1}{2\rho q_v c_p}$$

With  $q_v$  the volume flow rate of the cooling fluid passing the node  $i$  and  $c_p$  the specific heat of the cooling fluid.

The system to solve becomes:

$$\Delta T = (G + G_{fluid})^{-1}P$$

## Application

Now, we will apply the thermal analysis previously developed at our case. First of all, we have to represent our geometry with coaxial cylinders. The sketch of our simplified generator can be found on Figure 4.11.

We made two different analyses: one with a small cooling fluid taken from the wind in the air gap and one without cooling flow. Both circuits of thermal resistances are on Figure 4.12

The first circuit is the one without cooling fluid. There is no fluid at the generator and air gap ends. We considered the ends as insulated. The circuit is then only composed of radial thermal resistances. To find the thermal resistance of convection in the gap, we use the equations previously given for the case without forced gaz flow. To find the convection coefficient between the wind and the external wall of the rotor, we used equations found in [7].

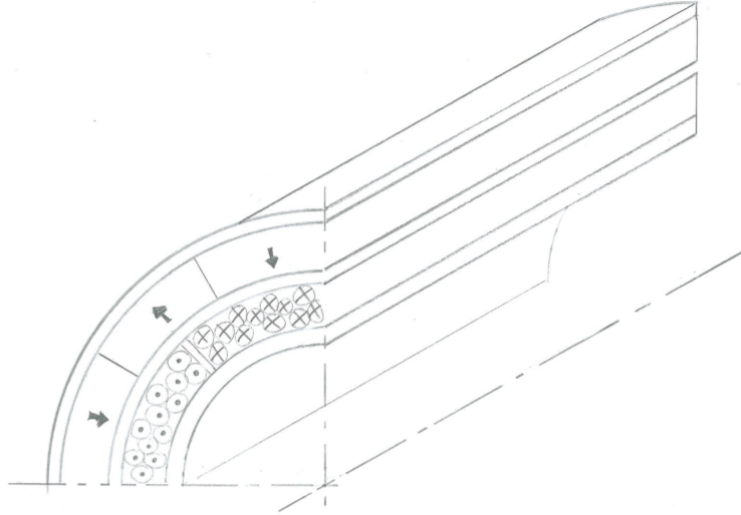


Figure 4.11: Simplified generator

The second circuit is with cooling flood into the air gap. This is why it possesses both: radial and axial thermal resistances. To find the thermal resistance of convection into the air gap, we use the equations given for the case with cooling fluid. For the others ones we used equations found in [7].

The main thermal parameters of our materials can be found in table 4.6.

	Symbol	units	ABS	Magnets	Copper	Iron	Windings
Thermal conductivity (at 300°K)	k	W/(m K)	0,17	8,949	398	80.3	-
Mass heat capacity	$c_p$	J/(kg K)	1675	502	412	385	-
Maximum temperature	t	°C	108	80	1085	1538	180

Table 4.6: Thermal parameters

The ultimate thing that we have to do before resolving the system is finding an approximation for the losses. Knowing the maximal power produced by the generator and the approximation of the efficiency, we can calculate the value of the losses:

$$P_{losses} = \frac{P_{gen}}{\eta_{gen}} - P_{gen} = \frac{139}{0.8} - 139 = 35W$$

These losses can be separated in two types: aerodynamic losses that occur in the air gap due to the air friction and electrical losses (copper losses and iron losses). Mathematical form of aerodynamic losses can be found in [32]. As the rotational speed of the generator isn't high, after an approximation, we found out that mechanical losses are negligible compared to electrical losses. In iron losses, we consider eddy current, hysteresis and excess losses in the stator iron cylinder. Approximations of these losses are given in [8, 27]. Thermal conductivities of the windings and the iron are both high. In a stationary state, they then have nearly the same temperature. Thus, we can make the approximation that all the losses occur in the windings.

We can now resolve the system. Parameters used and simulation results can be found in Table 4.7 and Table 4.8.

For the generator configuration without cooling flow in the air gap, the limit temperature for the windings is nearly reached. The convection coefficient in the air gap is the limiting factor and

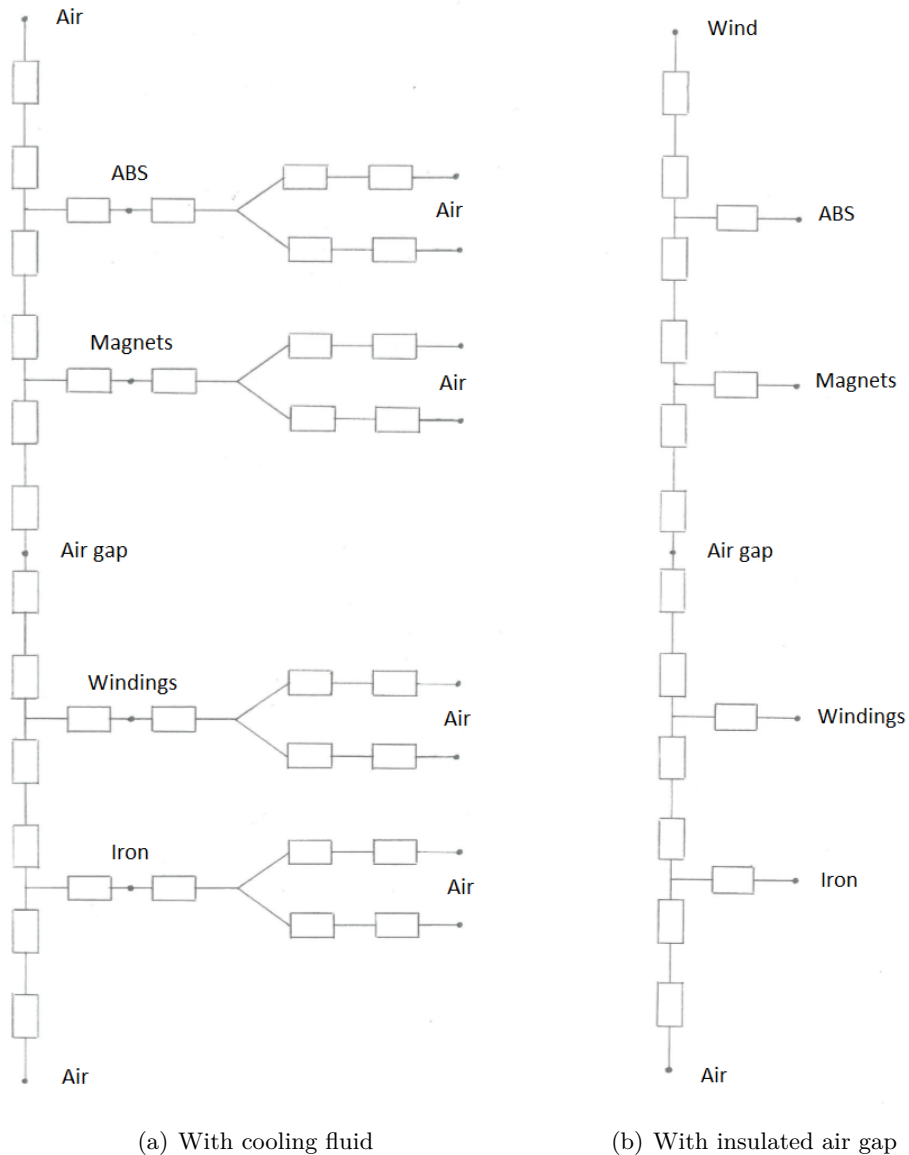


Figure 4.12: Circuit of thermal resistances

is just sufficient to prevent the melting of the wires sheaths. In this case, a way to reduce the temperature is imposing a smaller air gap. For example, with an air gap 25% smaller, we reach a temperature of 144.3°C in the windings. But reducing the air gap can be difficult as we have to do the assembly with several pieces made in ABS (see section 5.3.2). Another way to lower the temperature is to increase the generator length. Indeed, it extends the convection area in the air gap. By increasing this area by 25%, we find a windings temperature of 122.3°C

Nevertheless, the best way to reduce efficiently the windings temperature is to impose a cooling flood in the air gap. As we can see in the result table, with such a solution, we reach a temperature of 72.1°C in the gap, what is far from the limit temperature. Another advantage is that there is nearly no increase of temperature in the rotor items. Actually, almost all the heat is transmitted to the cooling flood. However, this solution may be difficult to implement with the design considered in section 5.3.2.

In conclusion, we developed a simulation that can give us an approximation of the maximum temperature in all the generator parts. It allows to simulate a generator with or without a cooling

	R1	R2	R3	R4	R5	R6	L
Value [mm]	25	30	40	42	57	62	150

Table 4.7: Geometric parameters

Elements	Temperature [°C]	
	Without cooling fluid	With cooling fluid
Iron cylinder	172.9	72.07
Windings	172.9	72.1
Magnets	58.9	20.07
ABS	48.9	20.05

Table 4.8: Simulation results

flood in the air gap. The goal of this simulation is to be used after any generator design to verify if it works in a safety range of temperatures.



## Chapter 5

# Prototype design

In this chapter, we describe how we designed the parts of our prototype and how we linked each one with the rest of the whole prototype. The main constraint on the design of all these parts was the obligation to 3D print them in the *Up!* printer (see chapter 2). Indeed the build volume of this printer is very limited ( $120 \times 120 \times 120\text{mm}^3$ ) and most parts were impossible to print in one piece. So we had to split them in several pieces and find a way to efficiently put them together.

For each part, we will give the functions that the part has to satisfy. Then we will detail the different options that we considered and explain which was chosen given its pros and cons.

### 5.1 Main components

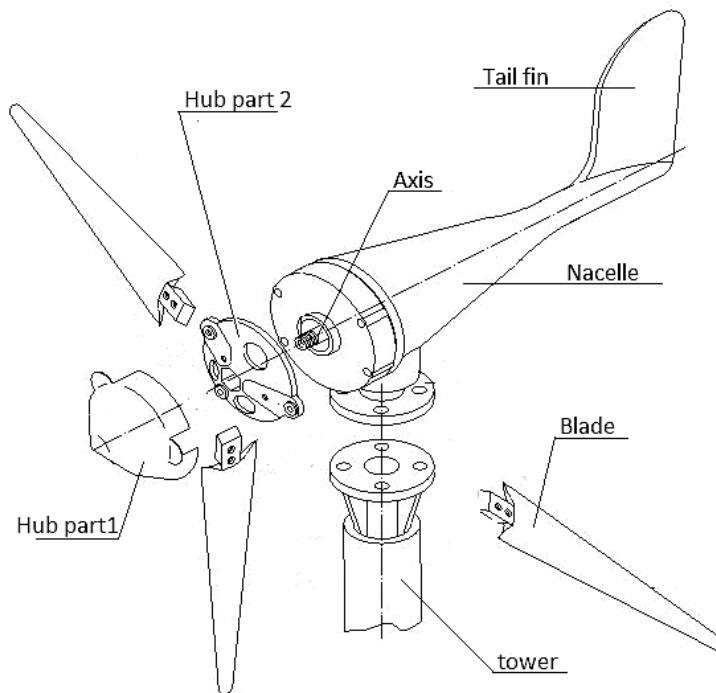


Figure 5.1: Structure of a small wind turbine (from [1])

There are the main components of a common small wind turbine (see Figure 5.1) :

- blade: part that converts the kinetic energy from the wind to mechanical energy
- hub: part that maintains the blades in position
- shaft: part that connects the hub to the generator and transmits the mechanical energy
- nacelle: part that supports and maintains the generator in position. It also contains the shaft bearings and the gearbox, if there is one.
- generator: part that converts mechanical energy to electrical energy
- tail fin: part that orientates the wind turbine in front of the wind
- tower: part that maintains the wind turbine at some distance from the ground
- cables: part that transmits electricity from the motor to the power electronics

All the elements are not visible on Figure 5.1. The generator cannot be seen because it is inside the nacelle. The cables are not present either but would pass through the nacelle and the tower by the hole in the center of these elements.

## 5.2 Blades

The blades have two functions:

- F1: create mechanical power from the wind the most efficiently possible
- F2: sustain high aerodynamic and centrifugal stresses

The first function F1 was already addressed in chapter 3: the shape and size of the blades was optimally defined to produce the most power possible. So in this section we only describe the solution for the second function F2: we had to think of an assembly method sufficiently robust (as the blades are too big to be printed in one piece). We considered two options (see sketches of Figure 5.2):

- glue between the parts (in red on the sketch)
- a threaded rod through the blade to compress the parts together

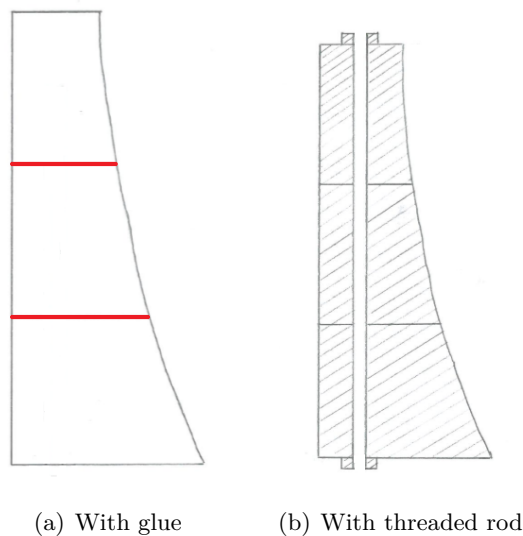


Figure 5.2: Blade assembly

The pros and cons of each solution are in Table 5.1.

	Pros	Cons
Glue between the blade pieces	<ul style="list-style-type: none"> <li>• Light</li> </ul>	<ul style="list-style-type: none"> <li>• Glue thickness between the parts</li> <li>• Less resistance to traction stresses</li> <li>• No compression of 3D printed layers</li> </ul>
Threaded rod through the blade pieces	<ul style="list-style-type: none"> <li>• Very robust</li> <li>• Compression of 3D printed layers</li> </ul>	<ul style="list-style-type: none"> <li>• Heavy (amplification of rotating unbalance due to assembly imperfections)</li> <li>• Force a minimum width at the tip of the blade</li> <li>• Holes in blades</li> </ul>

Table 5.1: Comparison of blades assemblies

Before taking a decision on the method of assembly, we made simulations in *Solidworks* to see which solution was the most robust. We simulated a rotation of the blades at 750 rpm and under thrust equivalent to a wind speed of 10 m/s. The parameters used are in Table 5.2 and results are on Figure 5.3. Parameters of materials were found in [11, 47]. On the left is the result with glue and on the right with the threaded rod. The final displacement at the end of the blade compared to its initial position is respectively 17.32 mm for the glued blades and 6.16 mm for the other. We conclude that the most robust option is of course the threaded rod but also that the deformation of the glue assembly is too high and not acceptable. That is why we decided to use threaded rods to assemble our blades.

Materials		
Young modulus [Pa]	ABS	$2.2 \times 10^9$
	Glue	$2.46 \times 10^9$
	Threaded rod	$2.1 \times 10^{11}$
Poisson's ratio [-]	ABS	0.394
	Glue	0.401
	Threaded rod	0.28
Maximum stress [Pa]	ABS	$30 \times 10^6$
	Glue	$17.5 \times 10^6$
	Threaded rod	$723.6 \times 10^6$
Stresses		
Wind speed [m/s]		10
Thrust on the blades [N]		38
Rotational velocity [rpm]		750
Blade mass [g]		181.5

Table 5.2: Rotation of the blade: *Solidworks* simulation parameters (partly from [11, 47])

Finally, to align pieces of the blades together, the easiest way is to use keys (*clavettes*) between each piece. We could use either 3D printed keys or separately manufactured metal keys. Even if 3D printed keys are more simple to produce as we already print all our parts with a 3D printer,

the metal keys are more robust and we can better control their dimensions. That is why we decided to use metal keys.

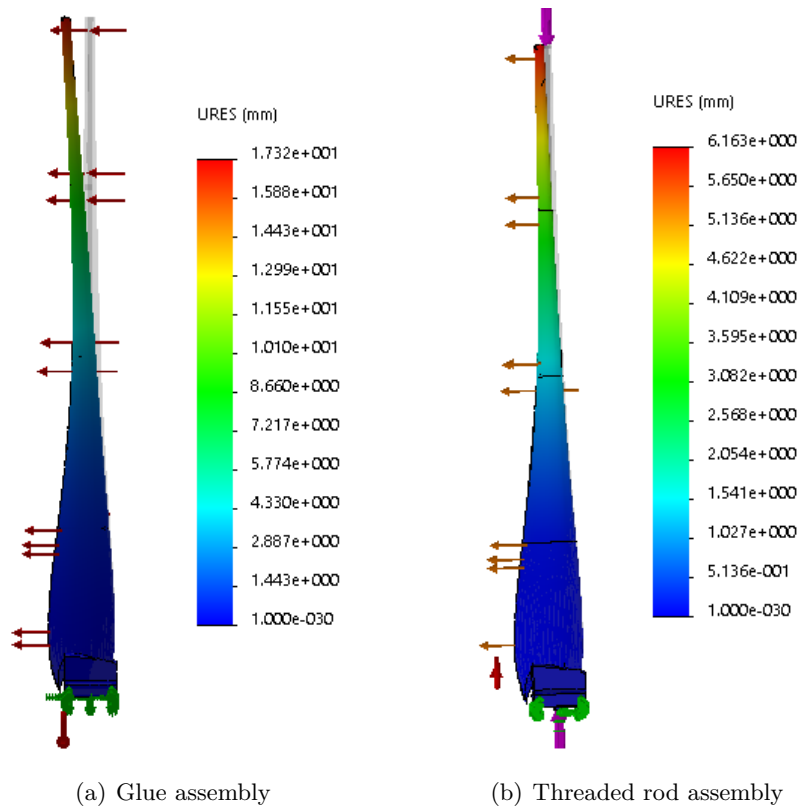


Figure 5.3: Rotation of the blade: *Solidworks* results

## 5.3 Hub

The hub has three functions:

- F1: secure the blades together to form the rotor (but allow to change the blades if needed)
- F2: connect to the shaft of the generator and transmit the torque produced by the blades
- F3: not disturb the flow or induce turbulences

These functions are sorted by order of importance. We will then analyzed them in the same order to define the hub step by step.

### 5.3.1 F1: hub and blades

The connection between the blades and the hub is the most important. Indeed, small wind turbine have a high rotational speed. Thus the blades and the hub must sustain very high radial stresses. We developed three different propositions, each one with advantages and inconveniences.

#### Proposition #1

The first proposition is to print directly a part of the hub at the blade root. The blades would be screwed to the main part of the hub. A sketch of this proposition can be found on Figure 5.4

and the pros and cons are in Table 5.3.

Pros	Cons
<ul style="list-style-type: none"> <li>• Easy to change blades</li> <li>• Simple</li> <li>• Small hub</li> </ul>	<ul style="list-style-type: none"> <li>• Delamination of plastic layers with screws</li> <li>• Not very robust</li> </ul>

Table 5.3: Pros and cons of hub proposition #1

### Proposition #2

For the second proposition, the blades roots would be locked in the hub using sliding dovetail joints. The hub would be printed in two parts that would compress the blades roots. This technique is already considerably used in other small wind turbines [56, 2]. A sketch of this proposition can be found on Figure 5.4 and the pros and cons are in Table 5.4.

Pros	Cons
<ul style="list-style-type: none"> <li>• Very robust</li> </ul>	<ul style="list-style-type: none"> <li>• More difficult to change blades</li> <li>• Complex (more parts)</li> </ul>

Table 5.4: Pros and cons of hub proposition #2

### Proposition #3

The last possibility would be to include the roots of the blades directly as part of the hub. The rest of blades would be fixed by screws. So the fixation between hub and blades is more distant from the axis of rotation that reduces the stresses on it. A sketch of this proposition can be found on Figure 5.4 and the pros and cons are in Table 5.5.

Pros	Cons
<ul style="list-style-type: none"> <li>• Robust</li> <li>• Less radial stresses at the fixation point</li> </ul>	<ul style="list-style-type: none"> <li>• Resistance to axial stresses limited by the surface of contact</li> <li>• Impossible to change blades without printing a new hub</li> <li>• Very big hub</li> </ul>

Table 5.5: Pros and cons of hub proposition #3

### Comparison

The 3 propositions are compared in Table 5.6. As we can see no solution is perfect and we must compromise. We want to give priority to robustness so we chose the proposition #2, even though it involves manufacturing more parts. We realized that the speed of fabrication was an advantage of 3D printing anyway so more parts is not really a problem.

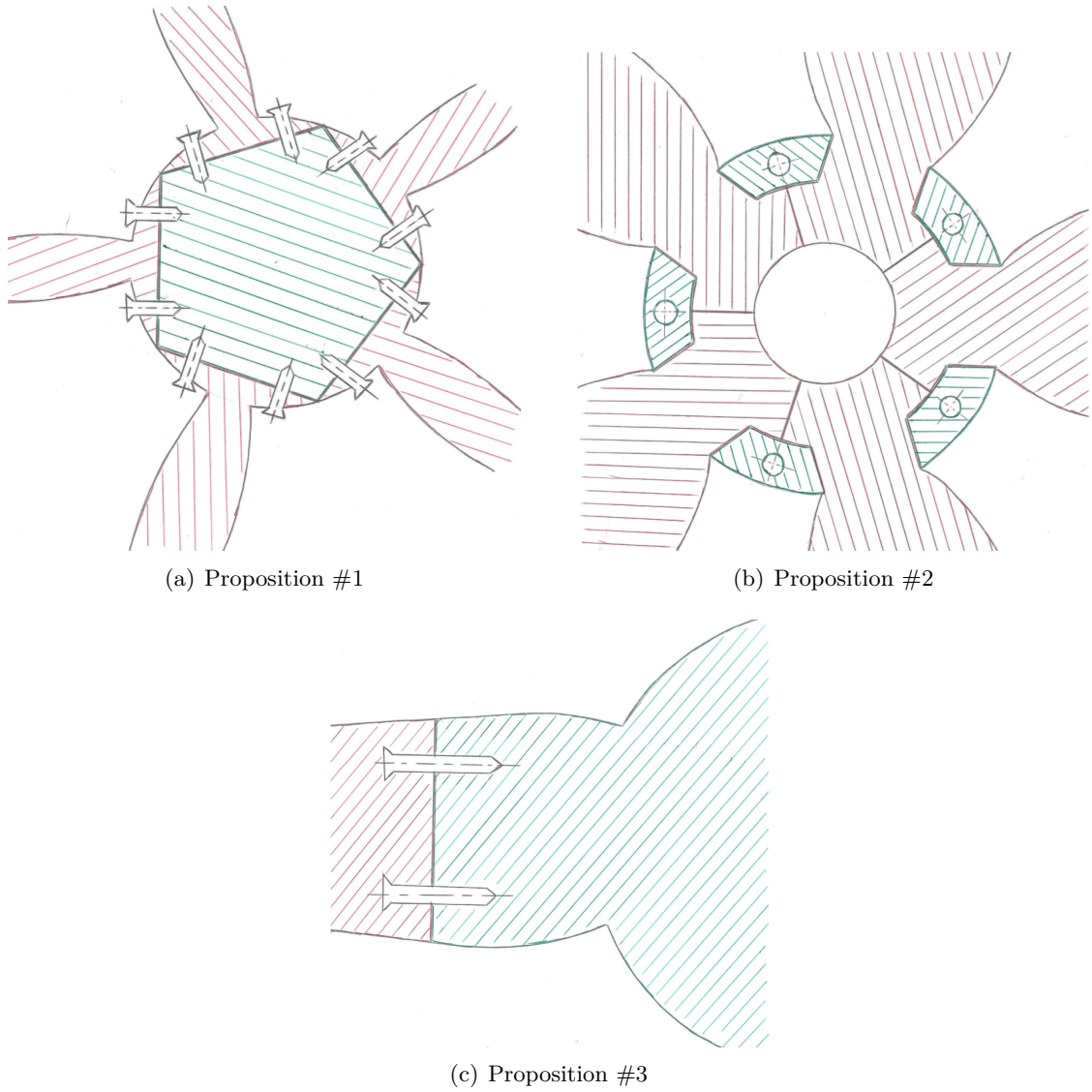


Figure 5.4: Blade and hub assembly

	#1	#2	#3
Hub robustness	-	+	+
Hub simplicity	+	±	±
Blade interchangeability	+	±	-

Table 5.6: Comparison of 3 hub propositions

### 5.3.2 F2: hub and generator

The connection between the hub and the generator is also very important. It must transmit the torque of the rotor to the generator. It also must insure that the rotor is securely attached to the shaft of the generator.

As explained in chapter 4, we thought of two types of generator: one off-the-shelf BLDC motor re-used as a generator and one ad-hoc generator manufactured by 3D-printing. We must find a different coupling solution for each of them. In the case of the ad-hoc generator, we did not have the resources and time to build it, so it is only a draft and should be refined in case someone wants to build it.

#### Off-the-shelf generator

Planetary gearhead bearing	
Max. axial load [N]	150
Max. radial load [N]	240

Table 5.7: Characteristics of planetary gearhead bearing

The BLDC machine that we use as generator was presented in section 4.1. It is composed of a planetary gearhead, a generator and an encoder. In Table 5.7 are the characteristics of the bearing of the planetary gearhead. As we can see, the maximal radial load is largely sufficient to support the weight of the rotor. That is why we decided to directly couple the rotor with the generator, without an intermediate bearing.

We can see that the gearbox has a keyed shaft. As a key is provided, we will use it to connect the hub to the shaft of the generator. The easiest way to do that is to create a bore with a keyway in the hub (see Figure 5.7). By sliding the keyed shaft into the hub we create a keyed joint.

A compression screw was added to press the key and maintain the rotor in place on the shaft. When we tested this hub with the compression screw, we found out that the screw induces a rotating unbalance at the nominal rotational speed. We then decided to use three compression screws instead of one, evenly spaced to even out the unbalance (see Figure 5.7).

#### Ad-hoc generator

The theoretical assembly for our ad-hoc generator is represented on Figure 5.6. References to this sketch will be made in the following explanations.

The ad-hoc generator designed in section 4.2 is a slotless external rotor PMSG. As it is supposed to be 3D-printed, we first considered printing the hub and the rotor in one big piece to avoid complex connection between these two parts. But, as we are limited in size by the 3D machine, we then thought about making it in several pieces assembled by threaded rods (red, blue and deep green pieces on Figure 5.6).

We have to be careful with the bearings position and tightening. We have to respect the rules for an assembly with an external rotor. Each bearing is constrained by shoulders and/or retainer rings. A special attention must be given to the mounting of those bearings, the shaft cannot be overconstrained (see Figure 5.5). The assembly of the rotating ring of the bearing must be tight and the assembly of the fixed ring must be loose. The ball bearings present on Figure 5.6 respect these rules of assembly.

The main elements of our rotor are the magnets. In our theoretical design, we put them in slots printed in the middle part of the hub-rotor assembly (blue piece on Figure 5.6). These slots would be closed by the assembly once the magnets in position. The wall that separates the magnets from the air gap has to be as thin as possible to reduce the gap between magnets and windings.

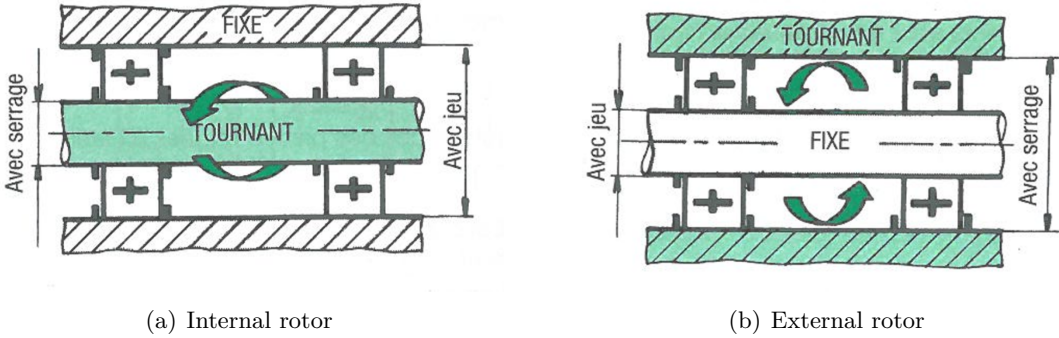


Figure 5.5: Assembly rule for bearings ([21])

For the stator, we chose to use a metal bar as the base (light green piece on Figure 5.6). Reasons are multiples: metal is a resistant material that is able to support the generator and hub mass, metal bars of all diameters can be easily found in any DIY store and metal is a magnetic material that offers a return path for magnetic flux. On this bar, we would place a 3D printed tube (purple piece on Figure 5.6). On this tube, there would be an obstacle for a bearing and teeth around which we will wind copper wires to create the windings of the stator.

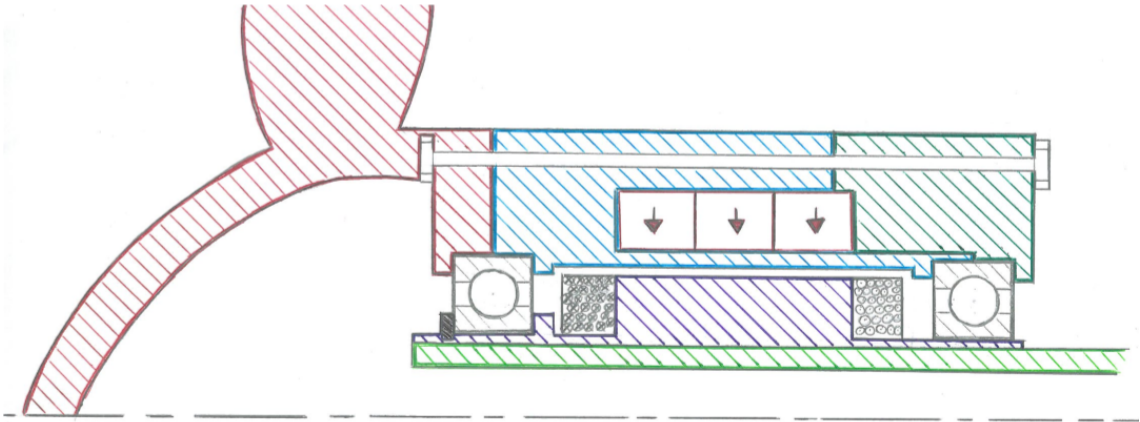


Figure 5.6: Sketch of generator and hub assembly

**5.3.3 F3: shape of the hub**

In order to reduce the aerodynamic drag on the structure, the hub should have an aerodynamical shape. To keep things simple, we chose the shape of an ellipse. See Figure 5.7.

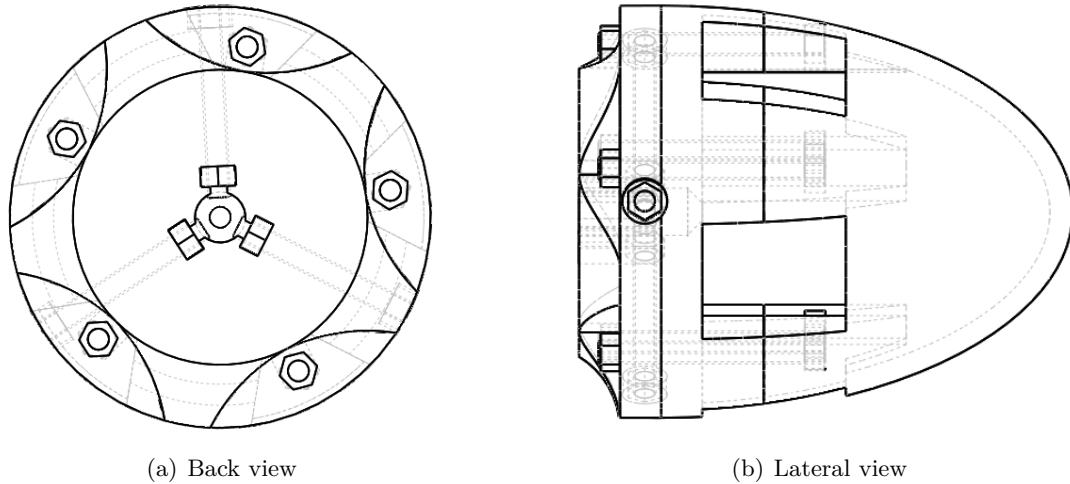


Figure 5.7: Shape of the hub

## 5.4 Nacelle

The nacelle has four functions:

- F1: house the generator and keep it in place
- F2: cool the generator with the oncoming flow if possible
- F3: allow the wind turbine to rotate on the tower
- F4: support the tail fin

### 5.4.1 F1 and F2: shape of the nacelle

As we explained in the last chapter, we decided to use a Maxon BLDC motor as generator. Thus the shape of the nacelle will depend on the the shape of the generator. To maintain the generator in position, we decided to clamp it. The nacelle part will then be printed in two different pieces that will be pressed against each side of the generator by screws. We need to tighten the parts sufficiently to prevent any rotation of the generator in the nacelle. This might happen if the wind speed varies suddenly and the regulator of the generator apply a very high electromechanical torque to counter-act it.

The second function of the nacelle is to avoid the generator to become too hot. Indeed, because of copper losses, the generator produce heat while it is functioning. The windings' temperature cannot exceed  $125^{\circ}\text{C}$ . Unfortunately, the thermal conductivity of ABS is small. The nacelle should then not cover entirely the generator but allow thermal convection with the air. Moreover, to improve the cooling it is better to have a forced convection. We then had the idea of using the wind flow to cool the generator. We printed a nacelle as a Venturi pipe (see Figure 5.8) to increase the air speed at the surface of the generator and increase the heat flow to cool the generator.

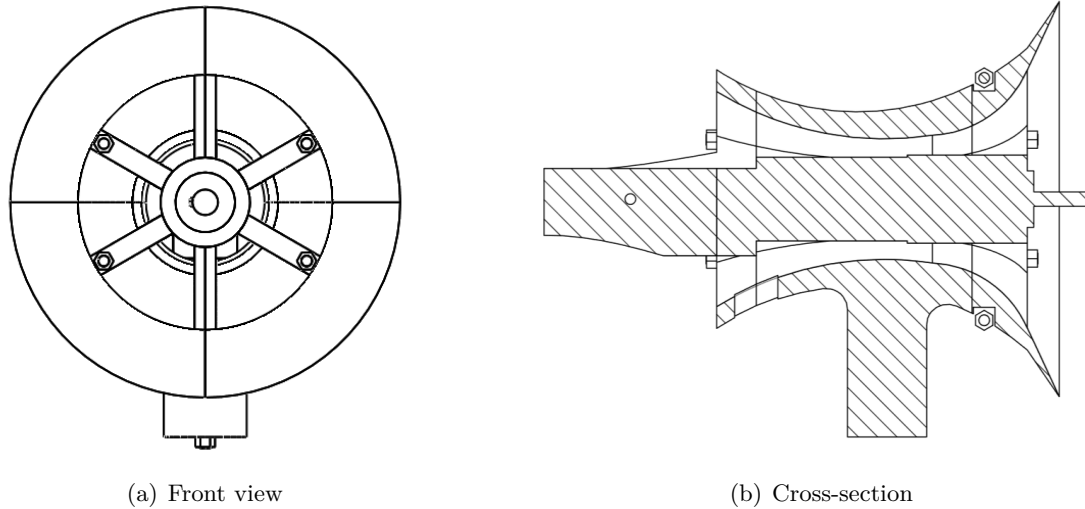


Figure 5.8: Shape of the nacelle

### 5.4.2 F3: nacelle and tower

To connect the nacelle to the tower, we need a rotative system. It allows the nacelle to align itself with the wind. The best way to do so is to use bearings. There are a lot of bearings types: roller bearing (tapered, cylindrical or needle) or ball bearing (single, angular or double). The sort of bearing to use depends on the stresses they have to support. In our case, the bearings will have to support axial stress due to the weight of the nacelle, as well as radial stress due to the thrust on the blades (see chapter 3). These forces are in Table 5.8. As this values are quite limited, we can use single ball bearings [20].

Loads on tower bearing	
Weight of the nacelle (axial load) [N]	29.92
Thrust on the blades (radial load) [N]	38

Table 5.8: Loads on tower bearing

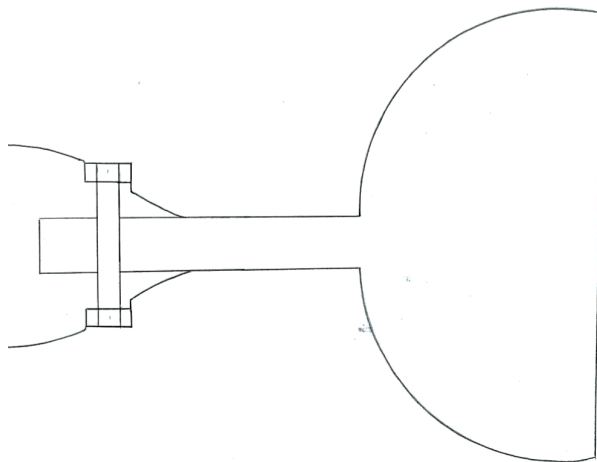
For the assembly of the bearing on the tower, we must respect the convention of Figure 5.5 [21]. For the exact choice of bearing, it depends on the tower and nacelle diameters. We did not use a tower for our tests so we did not install a bearing on the nacelle.

### 5.4.3 F4: nacelle and tail fin

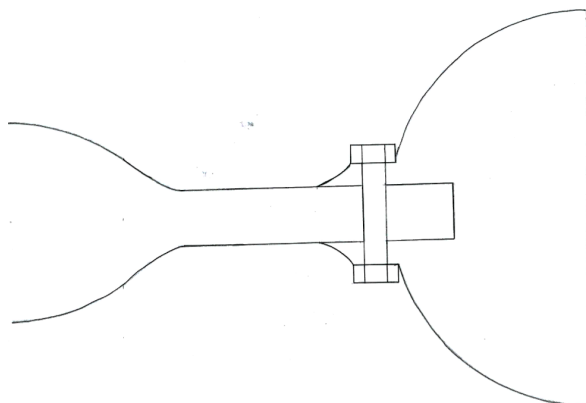
Three possibilities were considered: two with a bolt and one with screws. Sketches of the three ideas can be found on Figure 5.9.

We dismissed the solution with screws because it may cause damages delamination of the 3D printed layers. Furthermore screws don't fit really well for stresses in a radial direction when there is a small surface of contact, and that is the case here. Indeed the main stress came from the weight of the tail fin.

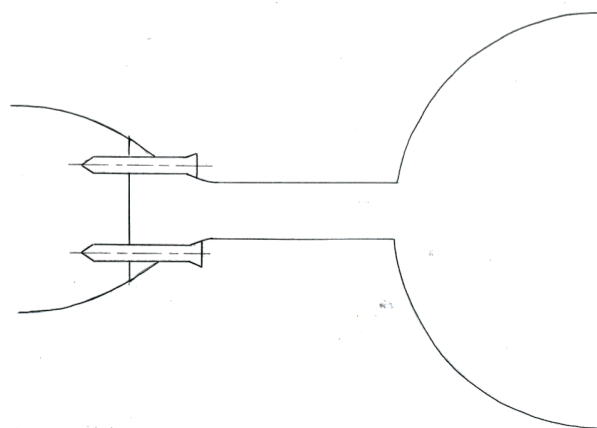
We finally choose the first proposal because, with this one, we can give a better aerodynamic shape to the assembly. Moreover, we can make a nacelle that is more compact.



(a) Proposition #1



(b) Proposition #2



(c) Proposition #3

Figure 5.9: Tail fin and nacelle assembly

## 5.5 Power transmission system

The function of the power transmission system is to transmit power from the generator to the load for any orientation of the rotor on the tower.

When the rotor turns around the tower to follow the wind direction, the cables transmitting power from the generator twist and might eventually break. This should be prevented by the power transmission system. We thought of three solutions:

- Untwisting motor: A position sensor measures the angle of the rotor and activates a small yaw motor when it is time to untwist the cables. This is the system used in full scale wind turbines.
- Slip ring: A mechanical system that will maintain the contact with brushes and bearings .
- Rotative transformer: rotating transformer which transmits electromagnetic power. AC power is needed.

In Table 5.9, we compare those three solutions.

	Untwisting motor	Slip ring	Rotative transformer
Price	–	+	+
Simplicity	–	+	±
Durability	+	–	+
Maintenance	+	–	+

Table 5.9: Comparison of power transmission devices

Considering this table, the rotative transformer seem to be the most appropriate solution for our small wind turbine. Indeed, it's unnecessary to add a complex system like the first proposition and the mechanical system doesn't fit the criteria like the rotative transformer. However, we did not install this system as we did not study the orientation of our prototype with respect to real wind.

## 5.6 Duct

The design of a duct was considered. The function of a duct is to increase the mass flow (i.e. the wind speed) through the rotor of a wind turbine. As the mass flow increases, the power produced by the wind turbine increases too. More informations about aerodynamical properties can be found in chapter 3.

We designed some ducts but it turned out that is was unrealistic to print it with the means put at our disposal (sketches and further explanations are present in annex). First of all, to be effective, the duct has to turn with the wind turbine upwind. So it has to be fixed either at the blades end or at the hub or the nacelle. In the first case, it would create rotating unbalance as we have to print it in lots of pieces. In the second one, the supports would be very long and would bend under the structure mass causing damages and potential destruction of the wind turbine. See section A.1 for additional precisions.

## 5.7 Complete prototype

On Figures 5.10 to 5.14, we can see the assembly or the blade, the hub and the nacelle.

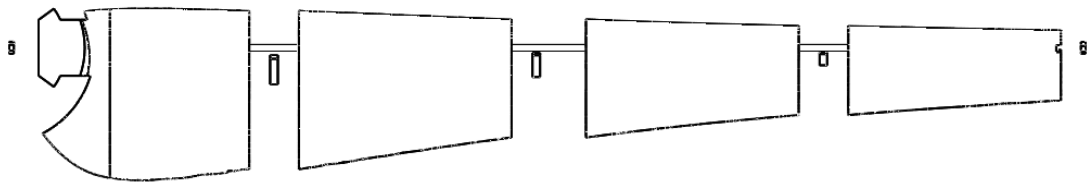


Figure 5.10: Blade assembly

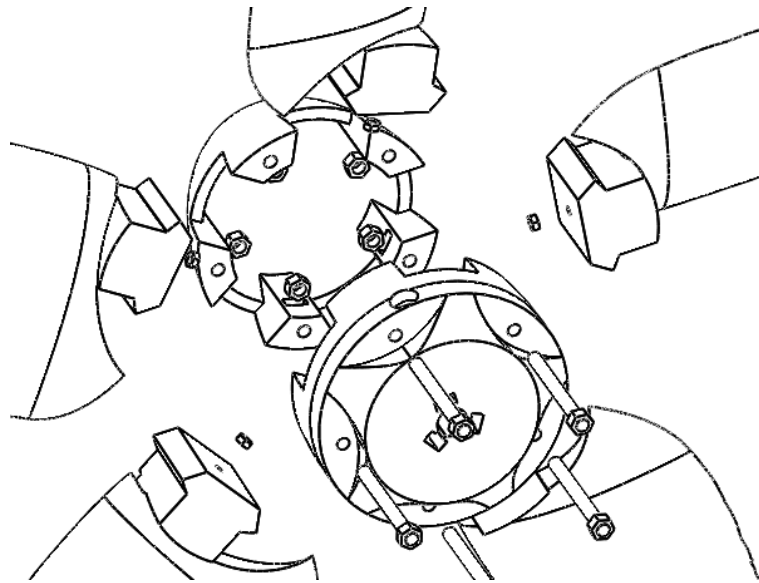


Figure 5.11: Hub assembly (back view)

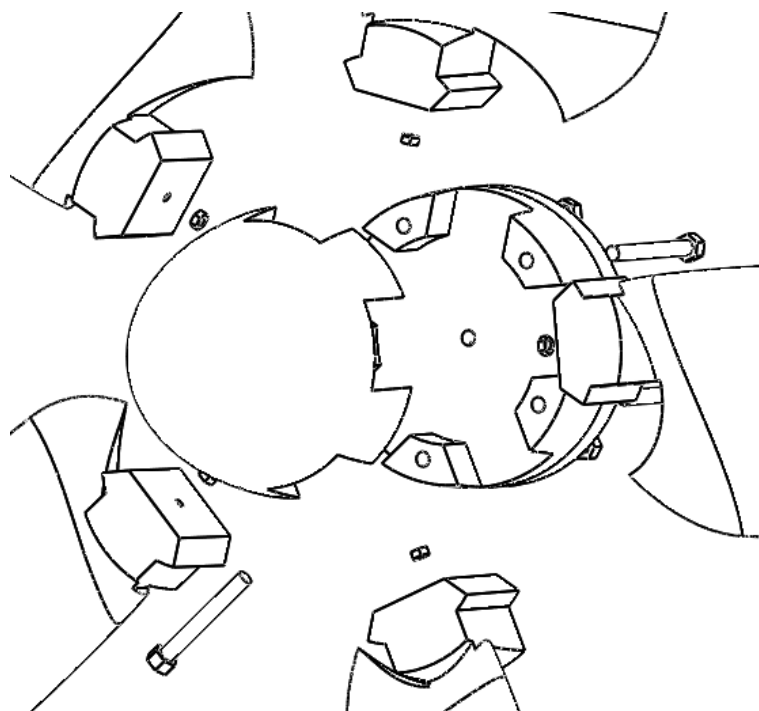


Figure 5.12: Hub assembly (front view)

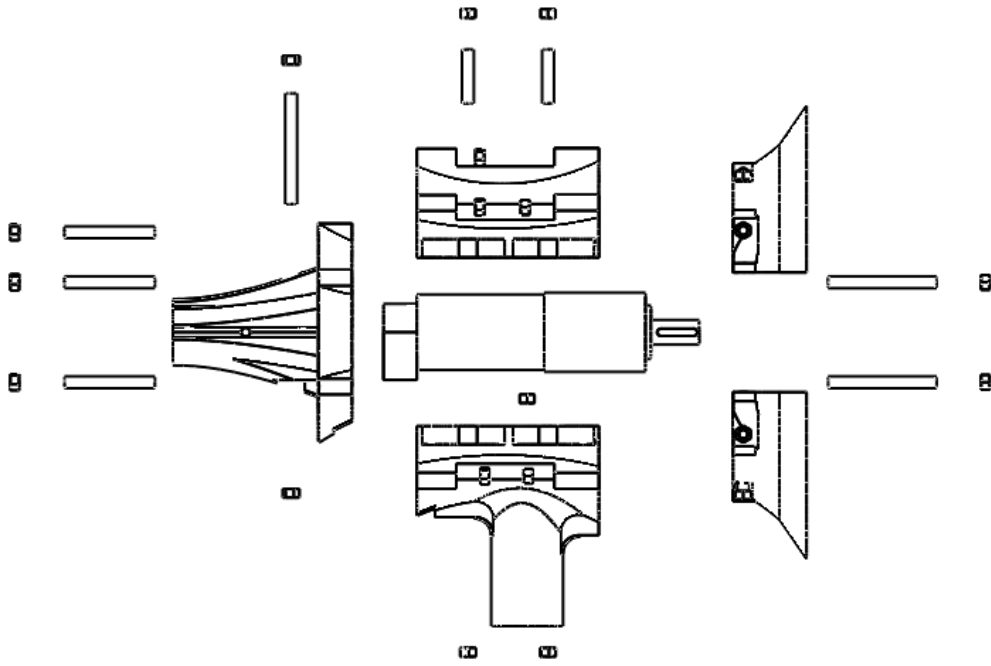


Figure 5.13: Global assembly (lateral view)

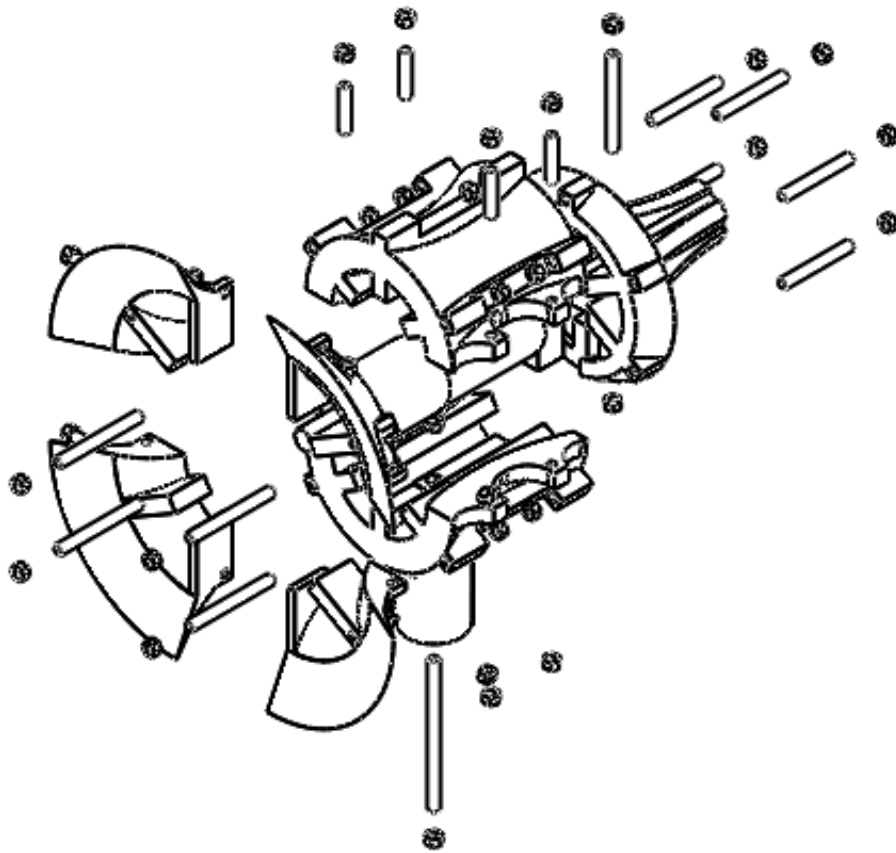


Figure 5.14: Global assembly (front view)

# Chapter 6

## Tests

After designing and building our prototype, we tested it to compare the results with the numerical predictions. We brought it in two different wind tunnels: the open-circuit wind tunnel of our university and the closed-circuit wind tunnel of the von Karman Institute (the biggest subsonic wind tunnel in Belgium). There, we applied different wind speeds to the wind turbine and we measured the power produced. We also studied the influence of the variation of rotor speed (and ultimately the influence of the tip speed ratio introduced in section 3.2.2). Finally, we tested different shapes of nacelle to see which could cool down the generator the most efficiently.

In this section, we will first present the devices that we used to measure the relevant characteristics of our prototype. Then we will explain the methodology we used to do the experiment. Finally, we will analyze the results that we found.

### 6.1 Aerodynamical setup

When testing an aerodynamic body in a wind tunnel, it is very important that the wind tunnel produces a steady and uniform flow with a flat velocity profile. If this is not the case, the experiment is not fully controlled and the results are skewed.

To produce the flow, a wind tunnel is usually equipped with a propeller and is either closed or open-circuit. The closed-circuit tunnel is usually better than the open one because the air at the inlet of the open-circuit tunnel might be very turbulent (depending on the return path from the output). After the propeller, the produced flow goes through a straightener and usually a honeycomb structure to cancel out the swirl induced by the propeller and limit turbulence. Finally there is often a contraction nozzle before the test section in order to accelerate the flow and give it a flat velocity profile.

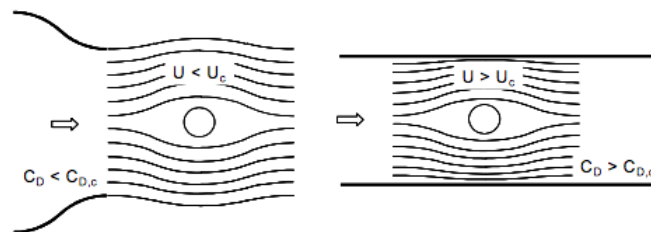


Figure 6.1: Blockage effect in open and closed test sections (from [52])

The test section of a wind tunnel might either be open (open jet wind tunnel) or closed (closed jet wind tunnel). In the case of the closed jet, the rigid walls around the test section prevent

lateral motion of the air and the velocity at the blade is then higher than it would be in an unlimited free stream. In the case of an open test section, it is reversed: the flow which goes out of the nozzle over-expand into the still air that surrounds it and the velocity at the blade is lower than in an unlimited free stream. This is called the blockage effect. It is less strong in the open test section than in the closed one [52]. To avoid it, the test section area must be much bigger than the aerodynamic body cross section area tested, so the body does not influence the whole stream-tube. In the case of wind turbines, the blockage ratio should be less than 10% for the blockage effect to be negligible [12]:

$$BR \triangleq \frac{S}{C} < 0.1$$

where  $S$  is the frontal area of the body tested and  $C$  is the area of the test section.

The blockage effect is characterized by the blockage factor, which is a function of the blockage ratio and the tip speed ratio [12]:

$$BF \triangleq \left( \frac{V_T}{V_F} \right)^3 = f(BR, \lambda)$$

where  $V_T$  is the wind speed in wind tunnel conditions and  $V_F$  is the wind speed in free stream conditions.

The body must also be sufficiently away from the walls to avoid the boundary layers (see fig. 6.2). The width of these boundary layers depends on the Reynolds number of the flow.

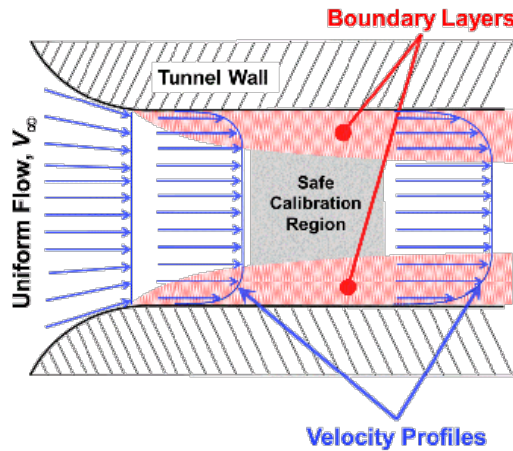


Figure 6.2: Velocity profile in a wind tunnel (from [28])

### 6.1.1 von Karman Institute: low speed wind tunnel L-1A

The wind tunnel at the von Karman Institute is 3 meters wide. It is a closed-circuit, open-jet tunnel and it is the biggest subsonic wind tunnel in Belgium. It was therefore the best place in which we could test our prototype. Its characteristics are in table 6.1. We can see that the turbulence level is very low. As the area of the cross section ( $9\text{m}^2$ ) is much bigger than area of the rotor of our prototype ( $1\text{m}^2$  for the biggest rotor), the blockage ratio is  $C/S = 0.098$ . This is sufficiently low to neglect the blockage effect. Because of all the qualities of this wind tunnel, we can expect the results to be very reliable. See fig. 6.3 for the setup at the VKI.

Type	Closed-circuit, open-jet tunnel
Diameter	3 m
Speed	2 - 60 m/s
Contraction nozzle ratio	4
Turbulence level	0.3 %

Table 6.1: VKI low speed wind tunnel L-1A: characteristics (from [23])

### 6.1.2 Wind tunnel at Université Catholique de Louvain

After testing our prototype at the VKI, we performed additional tests at the LEFT laboratory of our university in an open-circuit, open-jet wind tunnel. It is 1 meter wide and is equipped with a 6-blades propeller and a simple straightener. There is also no contraction before the test section. Because of the straightener and the boundary layers of the walls, the velocity profile was not flat at all but was varying along the whole cross section. We decided to measure the velocity at different points and to average it (see section 6.3).

The area of our rotor is almost equal to the area of the wind tunnel so the blockage ratio is very high ( $BR = 0,88$ ). The blockage effect is then very significant and should not be neglected. Unfortunately blockage corrections for horizontal axis wind turbines in open jet wind tunnel are not well defined. So we decided not to correct these results from the UCL wind tunnel and consider them approximative. Nevertheless they can still give some qualitative insights. See fig. 6.4 for the setup at the UCL.

Type	Open-circuit, open-jet wind tunnel
Diameter	1m
Contraction nozzle ratio	0
Turbulence level	2-3%

Table 6.2: UCL LEFT wind tunnel: characteristics

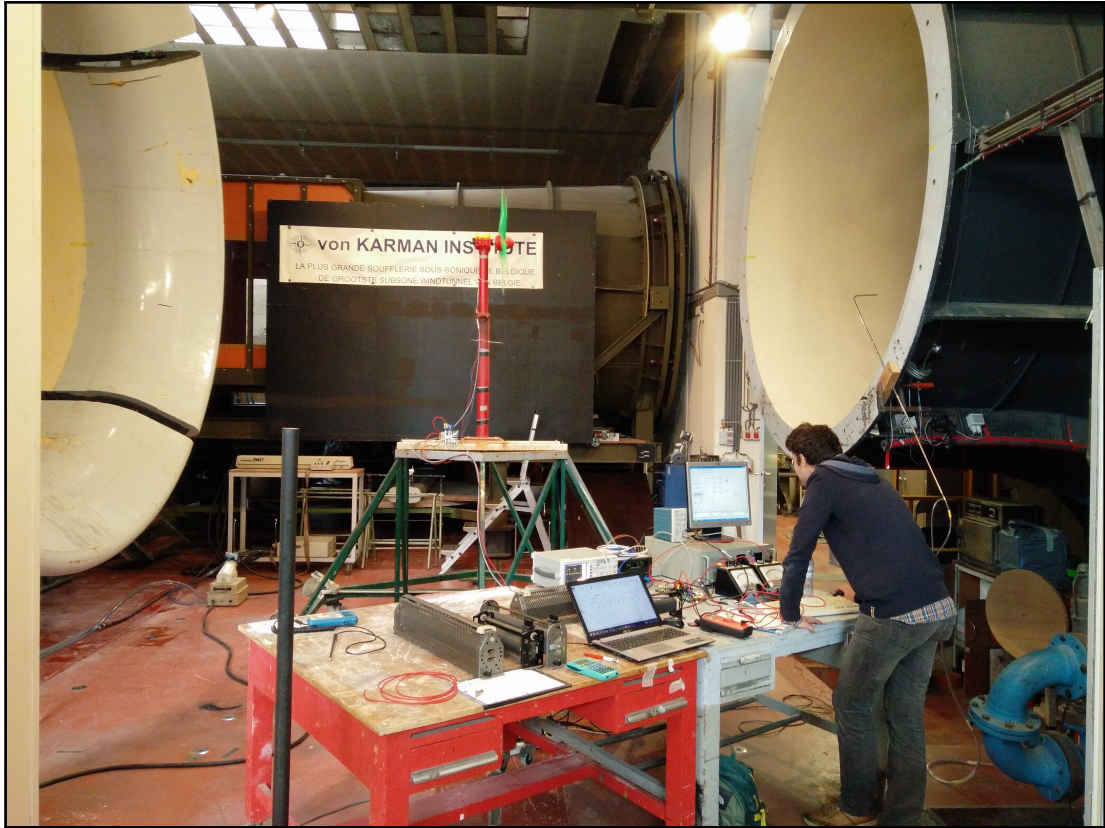


Figure 6.3: Experimental setup at von Karman Institute



Figure 6.4: Experimental setup at UCL LEFT

## 6.2 Electrical setup

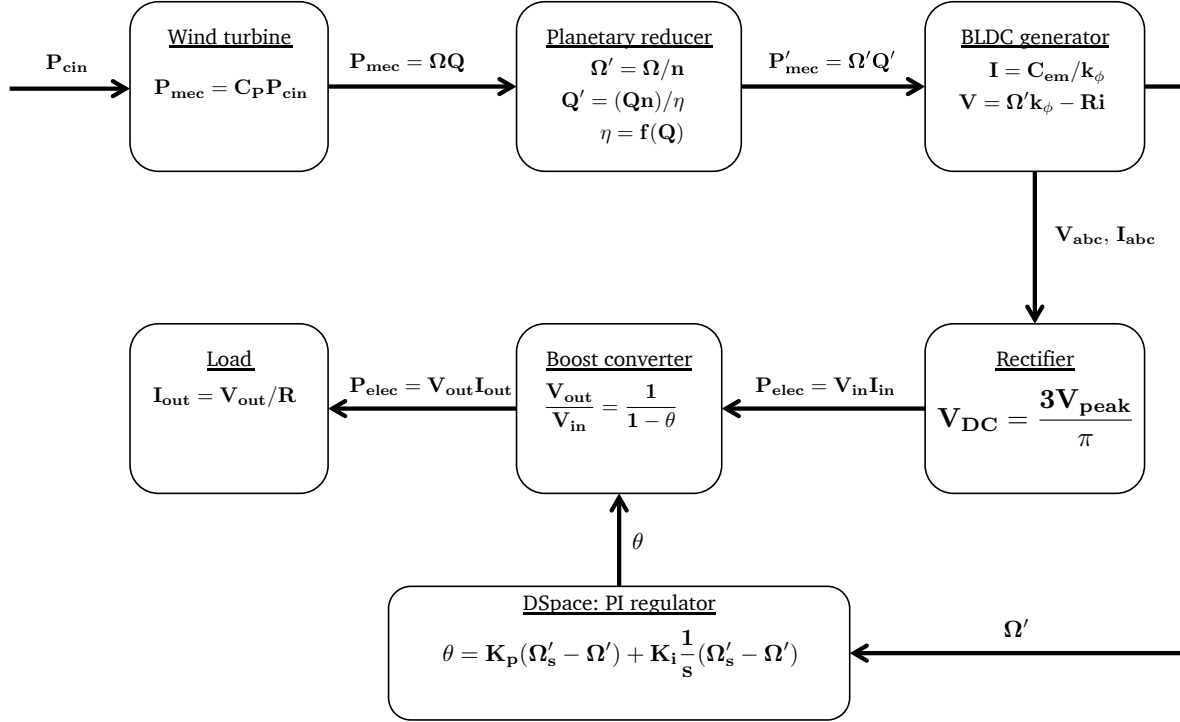


Figure 6.5: Experimental setup diagram

### 6.2.1 Rectifier

A rectifier is an electrical device that converts AC into DC voltage. In our case, the Maxon generator output is three-phase. We then choose to use an uncontrolled three-phase bridge rectifier (see fig. 6.6). This device is composed of six diodes. The output is the maximum of the rectified line voltages. The ideal DC output voltage can be calculated with the input line peak voltage:

$$V_{DC} = \frac{3V_{peak}}{\pi}$$

We add a capacitor in parallel with the output to smooth the DC voltage. While output tension increase, the capacitor voltage follows the signal because its tension is imposed. While output tension decrease, the capacitor attempt to keep the tension at its peak value (see fig. 6.7)

### 6.2.2 Boost converter and load

To control the wind turbine, it is necessary to be able to adjust the electromagnetic torque of the generator. For a BLDC machine such as the Maxon EC40 used for our prototype, the torque is proportional to the current flowing through the windings:

$$T_{em} = k_\phi i_0$$

with  $k_\phi$  the torque constant and  $i_0$  the current flowing through the windings.

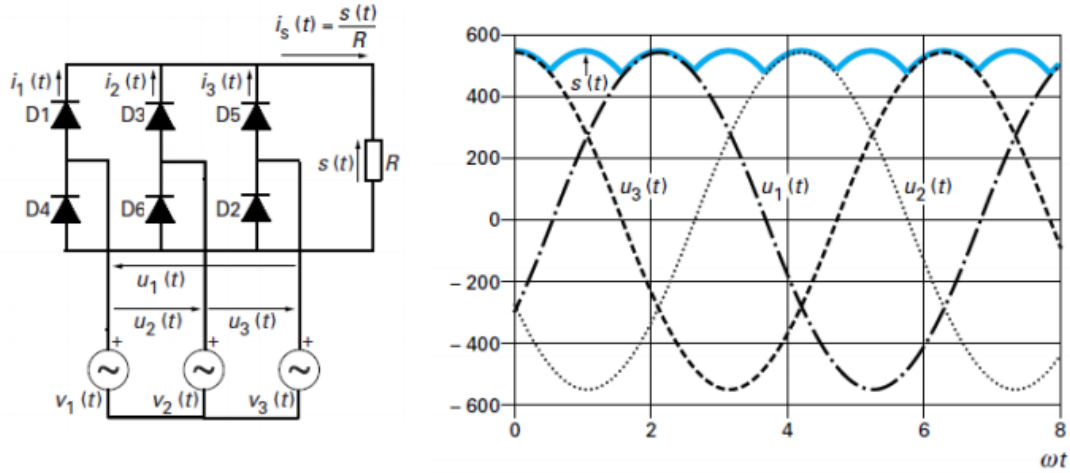


Figure 6.6: Three-phase passive rectifier [6]

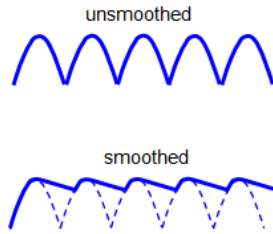


Figure 6.7: Influence of the capacitor [6]

Thus we can control the electromagnetic torque by controlling the current. The output tension of the generator is directly proportional to the rotation speed. Then, the only mean to control the current is to vary the resistance saw at the generator output.

To make this control, we use a boost and a fixed load. The boost is a DC-DC power converter that steps up by a factor  $k$  the voltage from its input to its output. The equation that rules the converter is:

$$\frac{V_{out}}{V_{in}} = \frac{1}{1 - \theta} = k$$

With  $\theta$  the duty cycle. The converter possesses a switch that is controlled with an high frequency binary signal. When the switch receives a 0, the circuit is open (Off) and when it receives a 1, it is closed (On). The duty cycle  $\theta$  is the fraction of the commutation period during which the circuit is On.

As power losses aren't significant, the current at the output is reduced by this same factor  $k$ . The current equation can be deduced:

$$P_{in} = P_{out} \Rightarrow \frac{I_{out}}{I_{in}} = \frac{1}{k}$$

Based on these equations, we can find the relation between input and output resistances:

$$R_{out} = \frac{V_{out}}{I_{out}} = \frac{kV_{in}}{\frac{I_{in}}{k}} = k^2 R_{in} = \left(\frac{1}{1-\theta}\right)^2 R_{in}$$

The load we put at the boost output is fixed. The charge seen at the input is then entirely determined by the converter duty cycle. By varying its value, we will instantly change the boost input current. As the electromagnetic torque is proportional, it will vary in the same fashion. The rotational speed variation is determined by:

$$J \frac{d\omega}{dt} = Q - T_{em}$$

With J the moment of inertia and Q the mechanical torque applied by the wind on the rotor. Thus, a diminution of the duty cycle slow the rotor rotation. On the contrary, imposing an higher duty cycle value increase the rotational speed.

The output voltage of our boost is limited at 50V and the duty cycle range is fixed by the switch at [0.1-0.9]. The factor k range is then [1.11 -10]. Thus the value of the load seen at the input reach as maximum 0.81% of  $R_{out}$  and as minimum 0.01 %.

The fixed load value has to be wisely chosen. On one hand, if we choose a small one, we can arrive in a case where we would be unable to decrease the electromagnetic torque and so increasing the rotational speed. On the other hand, to increase the rotational speed with a high resistance, we have to impose an higher factor k. The output voltage will then increase and reach rapidly the limitation of 50V.

During the tests, we disposed of a large choice of resistances that allowed us to work without limitations.

### 6.2.3 DSpace: PI regulator

To regulate the rotational speed, we use a proportional-integral controller. The PI controller continuously calculate the error between the desired and the actual rotational speed. It controls the rotational speed by regulating the duty cycle of the boost converter. Our PI controller equation is:

$$\theta = K_p(\Omega_s - \Omega) + K_i \frac{1}{s}(\Omega_s - \Omega)$$

with  $K_p$  the proportional constant and  $K_i$  the integral constant.

The proportional term  $K_p(\Omega_s - \Omega)$  produces a  $\theta$  value that is proportional to the rotational speed error. A high proportional constant  $K_p$  will induce a quick rotational speed variation but also a large overshoot. As we want a smooth response, we choose a small value for this constant.

A proportional regulator induces a steady-state error that makes impossible to reach the exact rotational speed. It is why the integral term  $K_i \frac{1}{s}(\Omega_s - \Omega)$  has to be added. The integral constant  $K_i$  accelerates the response at a rotational speed error and suppress the steady-state error. We put a small value to this factor because a high value produces a overshoot.

## 6.3 Methodology

### 6.3.1 Wind velocity measurements

As the wind tunnel at UCL LEFT has a varying wind speed along the radius of the test section, we decided to use the log-Tchebycheff method to measure the wind velocity. It consists in measuring the wind speed along three different diameters of the test section and 6 times for each diameter (see Figure 6.8). Each point is placed along the diameter to minimize the error. The coordinates of those points are in Table 6.3. We also choose to measure the power produced by each rotor at 3 different speeds to capture the  $Re$  influence over the blade aerodynamics. Indeed we know that at very low  $Re$  the performance of airfoils decreases very much (see chapter 3) and the wind velocity has a linear effect on the  $Re$  at the blade:

$$Re_c = \frac{\|\vec{V}_t\|c}{\nu} \simeq \frac{V_0\sqrt{1+\lambda_t^2}c}{\nu}$$

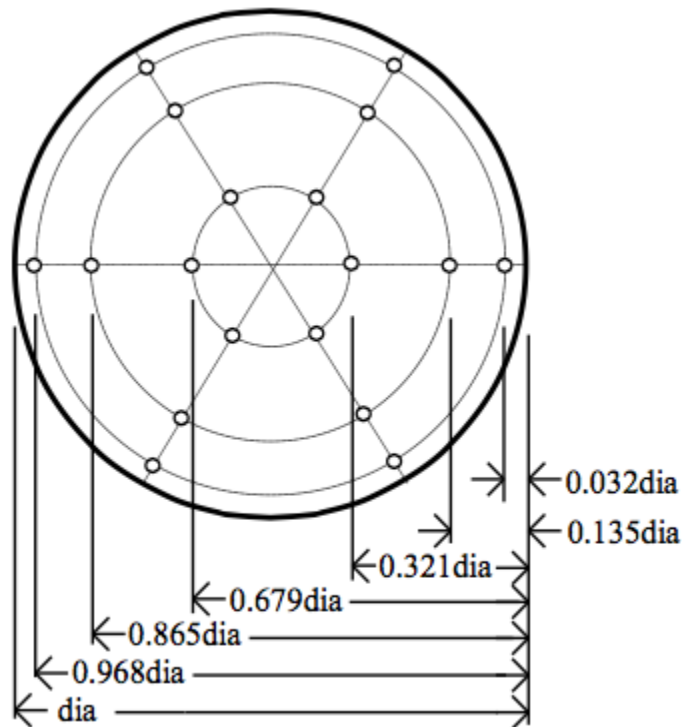


Figure 6.8: log-Tchebycheff method [34]

See [34].

$r/R$	0.032	0.135	0.321	0.679	0.865	0.968
-------	-------	-------	-------	-------	-------	-------

Table 6.3: Position of measuring points for log-Tchebycheff method [34]

### 6.3.2 Hub balancing

During the first test of the two hubs we designed, it appeared that they both suffered from rotating unbalance. We were aware that this problem could happen, especially for the smaller

one because there is only one compression screw on it which makes the hub asymmetrical (see section 5.3.2). For the bigger rotor, the unbalance is due to imperfections in the assembly as its hub is composed by 22 3D printed pieces (a total of 61 pieces is used if we count threaded bars and nuts).

Conscious of the possibility that this problem could occur, we let exceed the threaded rods at the end of the blades. This rod excess is sufficient to put three extra nuts. This free area will be put to good use to place small masses (nuts) to balance the hubs.

With the small hub, we weren't able to exceed a rotational speed of 550 rpm. To balance the hub, we decided to compensate the tightening screw by putting three nuts on each end of the two blades on the other side of the hub. We then retested the hub and it turned out that it was now possible to turn at 850 rpm and even more.

For the other hub, the task was more complex because the assembly should have been perfectly symmetrical, that apparently wasn't the case. We put the hub in rotation at slow rotational speed and made the most of the colour difference between the blades pieces to see where was the unbalance. We then fix nuts at blade ends when it was necessary. After adjustment, the second rotor can also turn at high rotational speed until 800 rpm.

## 6.4 Results

In this section, we give the results obtained during the tests and we analyze them. We measured the power coefficient, the starting velocity and the temperature at generator. The raw data and the measuring instruments can be found in section C.1.

### 6.4.1 Power coefficient

The plots of power coefficients as a function of tip speed ratio are on Figure 6.9, Figure 6.10, Figure 6.11 and Figure 6.12. The power coefficients were measured with both rotors in both wind tunnels.

While comparing the results, the first conclusion we can derive is that there is a big difference between tests made at the Von Karman Institute and those made at the UCL.

As explained in section 6.1, wind speed isn't uniform in the UCL wind tunnel. We developed a method to find the average wind speed but, as the blades ends produce more than the parts near the hub, this method is useless. For the biggest rotor, the results are worse because we reach an unrealistic power coefficient value of near 0.6. This is so close of the Betz limit that we can considerate these results as irrelevant. For this rotor, more than the difficulty of wind speed estimation, the problem is its radius. Indeed it measures 940mm of diameter when the wind tunnel has a 1000mm diameter. As previously seen in section 6.1, it leads to an high blockage effect. We will now concentrate our analysis on the relevant results made at the VKI.

For the first rotor, all the results of efficiency are in table 6.4. We reach the maximum power coefficient with a tip speed ratio of more or less 2.8 for the three wind speeds. This result proves that ideal  $\lambda$  is independent of the wind speeds. The assertion we made in chapter 3 is thus verified. The power coefficient curves at 8 and 10 m/s are very similar but the one at 6 m/s is a bit below. This difference can be explained by a smaller gearhead efficiency for smaller mechanical torque (see section 4.1.4).

The power coefficient we reached is near 0.4 what is an excellent result. Indeed we attained the objective set at the beginning of the project. This rotor is better or equals all the scientific

models presented in the introduction. The maximal efficiency is equal to 0.27. Once again, our prototype outclasses the majority of wind turbines given in the introduction. It equals the  $\mu$ F500, the Rutland 914i and the Superwind 350.

VKI: Rotor 1 efficiency								
$V_0 = 6.04\text{m/s}$			$V_0 = 8\text{m/s}$			$V_0 = 10\text{m/s}$		
$\lambda$	$C_P$	$\eta_{tot}$	$\lambda$	$C_P$	$\eta_{tot}$	$\lambda$	$C_P$	$\eta_{tot}$
0.50	0.02	0.00	0.50	0.02	0.01	0.50	0.02	0.01
0.99	0.05	0.01	0.54	0.05	0.03	1.00	0.06	0.04
1.49	0.08	0.03	1.49	0.10	0.06	1.50	0.12	0.08
1.99	0.14	0.07	1.98	0.17	0.10	1.97	0.19	0.13
2.00	0.15	0.07	2.47	0.34	0.23	2.46	0.35	0.24
2.24	0.20	0.10	2.68	0.39	0.26	2.71	0.38	0.26
2.49	0.29	0.17	2.78	0.39	0.26	2.76	0.39	0.27
2.74	0.31	0.18	2.88	0.39	0.26	2.85	0.38	0.26
2.80	0.35	0.20	2.95	0.35	0.23	2.95	0.38	0.26
2.85	0.34	0.19	2.97	0.38	0.25	-	-	-
2.91	0.34	0.19	3.07	0.36	0.23	-	-	-
3.01	0.31	0.16	3.16	0.37	0.24	-	-	-
3.49	0.30	0.14	3.18	0.37	0.23	-	-	-

Table 6.4: Efficiency rotor1

For the second rotor, as shown in table 6.5, results are incomplete for the wind speed of 10 m/s. This is due at the fact that the power electronics of our bench wasn't designed for our wind turbine. We weren't allow to have more than 50V at the boost output. Thus we couldn't correctly regulate the charge seen by the generator. As for the precedent rotor, results at 4 m/s are lower than those at 7 m/s. The previous explanation is still valid in this case.

The power coefficient is maximum for a value of tip speed ratio similar for both wind speeds (around 3.5 at 4 m/s and at 7 m/s). There is a difference between the theoretical and actual optimal tip speed ratio. This difference is due to the method used to design the blades. Indeed, the optimal distribution of chord doesn't take the losses into account (see chapter 3 for more details).

We reached here a value of power coefficient around 0.35. It's less than the other rotor. It could be due to the fact that the airfoil FX63-137 was not originally designed for wind turbines, unlike the S834. But it is still a good result. Actually, with such a power coefficient, our rotor is better than two wind turbines created for research. The only one, issue from research, that surpasses it is the  $\mu$ F500. The average maximum efficiency has a value of 0.23 during a large range of tip speed ratio: [3.36-3.9]. This rotor has an efficiency within the mean of commercial wind turbines. Nevertheless it is better than both wind turbines with 3D-printed rotor ([39] and [25] reach 20% of efficiency).

As shown in section 3.4, the power coefficient predicted by the BEM method is 0.47 for both rotors. There is a big difference between our theoretical and tests results. This big difference is due to the oversimplification of the BEM method and the surestimation of the gearbox efficiency.

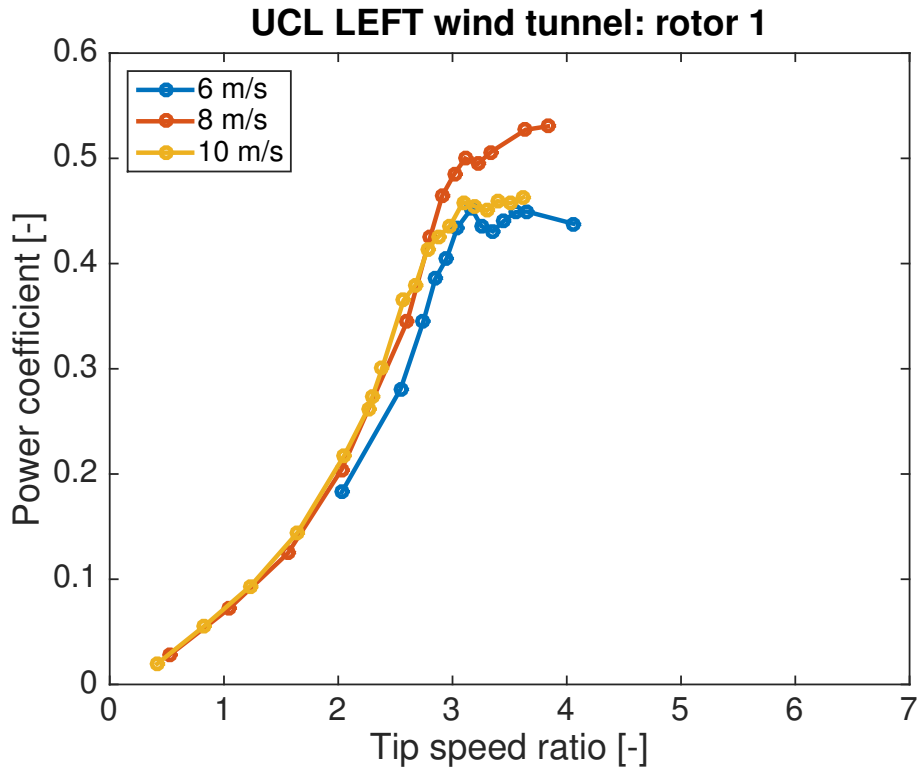


Figure 6.9: Power coefficient of rotor 1 at UCL LEFT

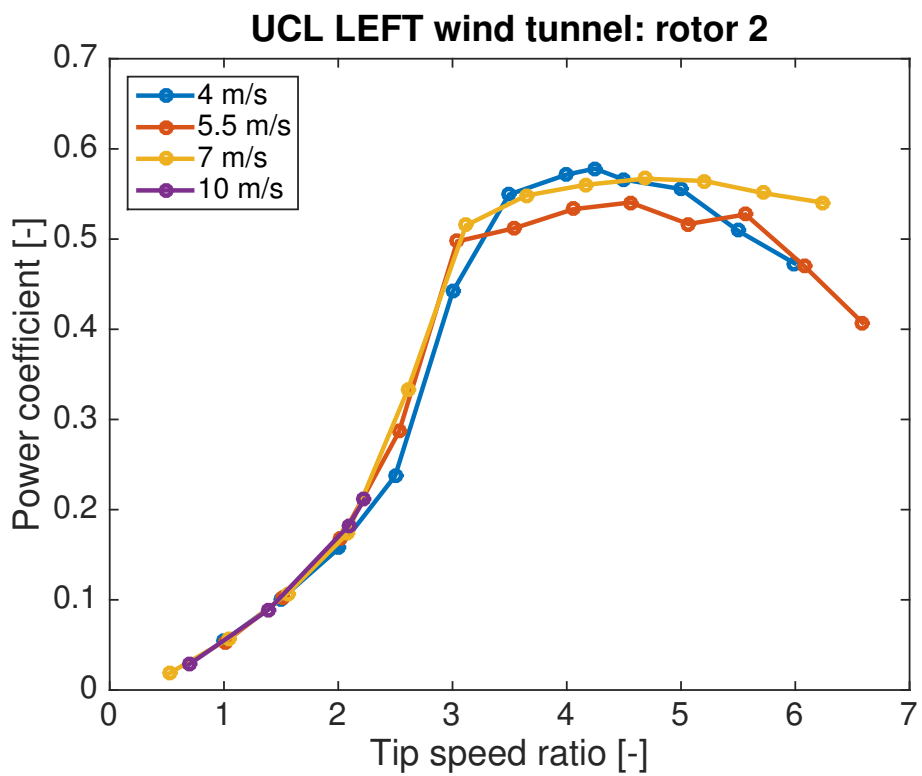


Figure 6.10: Power coefficient of rotor 2 at UCL LEFT

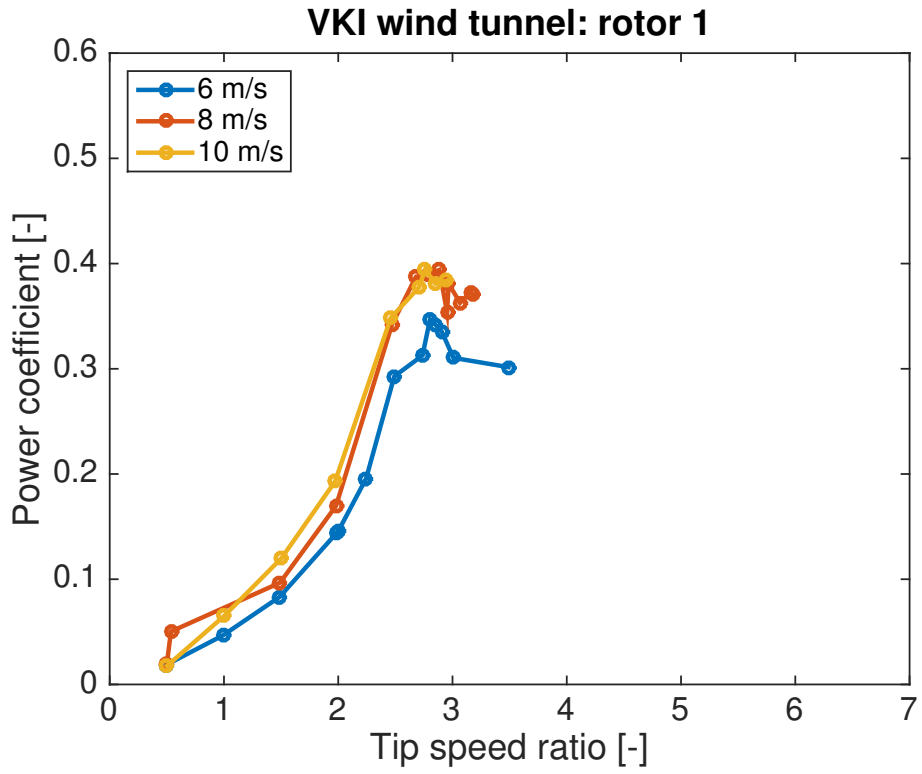


Figure 6.11: Power coefficient of rotor 1 at VKI

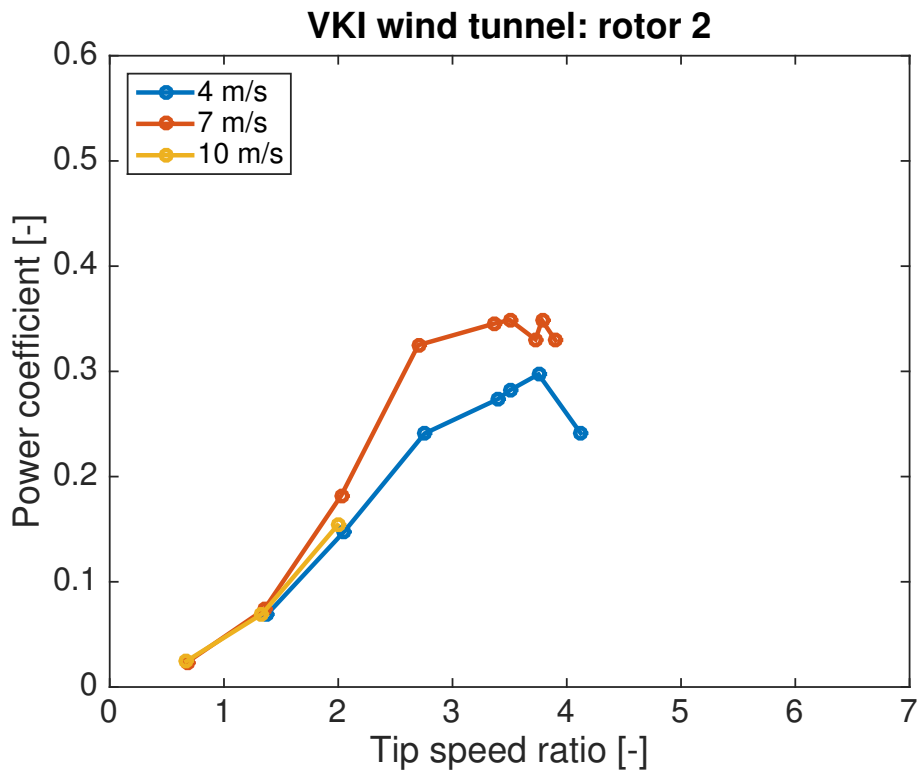


Figure 6.12: Power coefficient of rotor 2 at VKI

VKI: Efficiency rotor2								
$V_0 = 4\text{m/s}$			$V_0 = 7\text{m/s}$			$V_0 = 10\text{m/s}$		
$\lambda$	$C_P$	$\eta_{tot}$	$\lambda$	$C_P$	$\eta_{tot}$	$\lambda$	$C_P$	$\eta_{tot}$
1.38	0.07	0.03	0.67	0.02	0.01	0.67	0.02	0.01
2.05	0.15	0.07	1.35	0.07	0.04	1.33	0.07	0.04
2.76	0.24	0.13	2.02	0.18	0.12	1.99	0.15	0.09
3.40	0.27	0.14	2.70	0.32	0.20	-	-	-
3.51	0.28	0.15	3.36	0.35	0.23	-	-	-
3.75	0.30	0.15	3.50	0.35	0.23	-	-	-
4.12	0.24	0.10	3.73	0.33	0.22	-	-	-
-	-	-	3.78	0.35	0.23	-	-	-
-	-	-	3.90	0.33	0.22	-	-	-

Table 6.5: Efficiency rotor2

### 6.4.2 Cut-in wind speed

We measured with both rotors and in both wind tunnels the starting wind speed. To find it, we worked at no load (without connection between the generator and the power electronics). We then increased the wind speed until the beginning of the rotor rotation. In this configuration, the only torque the rotor has to overcome is the sum of dry frictions of the gearhead and the generator. As we don't have complete documentation about the gearhead, we can't find the theoretical value of this torque.

All the results can be found in table 6.6. We can see a big difference between results at the Von Karman Institute and those made at the UCL. This difference can be explained by the configurations of both wind tunnels (see section 6.1). As the wind turbine is constant all over the rotor area for the VKI wind tunnel, we will take the results obtained there as the real values for our wind turbine.

For the first rotor, we can explain the lower value measured at the UCL by the fact that our calculus of the wind speed is based on a average. Indeed, in the points used to do this average, we use the wind velocity of peripheral points that won't influence the rotor. All the wind speeds measured to make the approximation can be found in section C.4. We can observe that the peripheral values are the smallest and decrease the real wind speed average that arrives at the rotor.

For the second rotor, the value measured at the UCL is bigger than the one at the Von Karman Institute. This difference can be explained by the fact that our second rotor has more or less the same area that the wind tunnel used at the UCL. A blockage phenomenon will occur and lower the real wind speed at the beginning of the second rotor (see section 6.1).

The part that influences the most the cut-in wind speed is the beginning of the blades. Indeed, while the rotor is at rest, the value of the attack angle is  $90^\circ$  at the blades end (see section 6.1). Therefore, no lift force is produced there. On the contrary, the parts near the hub are the most twisted and then produce the torque to start the wind turbine.

The first rotor has a circular blade foot. Thus the blade root won't produce any torque. It is why this rotor has a bigger cut-in speed than the majority of others wind turbines. The other rotor is quite its opposite. The blades roots were studied to allow a quick start of the wind turbine. They fit closely the hub base and have a twist rather important. This permits to reach a very low cut-in speed of 1.5 m/s. This is a best result that all the others wind turbines analysed.

	Rotor 1	Rotor 2
$V_{start}$ [m/s] (VKI)	3.3	1.5
$V_{start}$ [m/s] (UCL LEFT)	2.8	2.14

Table 6.6: Starting wind speed

### 6.4.3 Generator temperature

To measure the effect of the Venturi form nacelle, we made two tests: one with the Venturi and one without. We measure temperatures of the gearhead and of the housing generator under the same conditions. We put a wind speed of 10 m/s and worked at nominal current. Indeed the main losses part come from Joule losses. The other part is aerodynamic losses. It is why we worked at relatively high rotational speed: 450 rpm. The thermal time constant of the generator, 1050 s, is given in the datasheet. We so knew how much time we have to wait to take our temperature measures under our experiment conditions.

The device we used to determine the temperature is a non-contact IR infrared thermometer gun: a SainSonic DT-8380. This thermometer allows us to measure accurate temperatures instantly without having to contact the object being measured. It works by capturing and measuring the infrared energy emitted from objects. The operating range goes from  $-50^{\circ}\text{C}$  to  $380^{\circ}\text{C}$  and has an accuracy of  $\pm 1.5^{\circ}\text{C}$ . It is sufficient to make us an idea about the Venturi efficiency. If we had wanted to obtain a better accuracy, we would have used thermocouples. The tests results can be found in table 6.7.

	$T_{gen}$ [ $^{\circ}\text{C}$ ]	$T_{red}$ [ $^{\circ}\text{C}$ ]
Without Venturi inlet	85	75
With Venturi inlet	62,5	60

Table 6.7: Results of temperature tests

As it can be noticed, the Venturi reduces significantly the temperature at the surface of both, generator and gearhead. Nevertheless the Venturi effect is better for the generator (temperature reduction of  $22.5^{\circ}\text{C}$ ) than for the gearhead (temperature reduction of  $15^{\circ}\text{C}$ ). On one hand, this difference come from the fact that head cooling flux is proportional to the temperature difference that is higher for the generator. On the other hand, the gearhead is placed directly after the hub that avoids the Venturi to work correctly at the gearhead beginning.

With the generator thermal resistance given in the data ( $R_{w-h} = 1.2 \text{ K/W}$ ), we can calculate the windings temperature. As we measured the housing temperature, the only thermal resistance we need is the winding-housing resistance (for more informations about generator head transfer, see section 4.1.3). The other parameter we need is the thermal losses. As we know the current and the rotational speed, we can easily find them. Let's first calculate the value of the losses power:

$$P_l = R_{pp} \cdot I^2 + (a + b \cdot \omega^2) \cdot \omega = 4.63 + 0.25 = 4.88W$$

With  $R_{pp}$  the terminal phase to phase resistance of the generator. a and b are the coefficients found in section 4.1.3 that allow us to find the mechanical losses torque. The thermal circuit equation is the following:

$$R_{th} \cdot P_l = \Delta T$$

Where  $R_{th}$  is the thermal resistance of the circuit and  $\Delta T$  the difference of temperature. Based on this equation, we now calculate the windings temperature for both case:

$$T_{w-i} = R_{w-h} \cdot P_l + T_{h-i} = 90.86^{\circ}\text{C}$$

$$T_{w-V} = R_{w-h} \cdot P_l + T_{h-V} = 68.36^{\circ}\text{C}$$

Where  $T_{w-i}$  is the windings temperature in the initial case,  $T_{h-i}$  is the housing temperature in the initial case,  $T_{w-V}$  is the windings temperature with the Venturi,  $T_{h-V}$  is the housing temperature with the Venturi. In both cases, the windings temperature is far below  $125^{\circ}\text{C}$ , the maximum permissible temperature. But, as the temperature limits the maximum current in the wires, the Venturi is useful and will allow to lightly increase the maximum performances of our wind turbine.



# Chapter 7

## Conclusion and perspectives

### 7.1 Achievements

The goal of our master's thesis was to design and build a small wind turbine by 3D printing in order to prove the reliability of this manufacturing method but also to make the design available to anyone. Additionally, it was specified that the wind turbine should be as efficient as commercially-sold models by taking advantage of the 3D printing capabilities. Indeed, an energy transition needs to take place in the world and research in renewables energies is crucial. The main application of small wind turbines is the local production of power in rural areas unconnected to the national grid, which is the case in large regions of Africa.

The main achievements of this study are:

- the utilization of a improved version of the Blade Element Momentum method.
- the creation of a functional 3D-printed horizontal axis wind turbine with two different set of blades.
- the design of a test bench including power electronics and software control.
- the test of the prototype in two different wind tunnels: one 1m diameter open-circuit wind tunnel at our university and one 3m-diameter closed-circuit at the von Karman Institute (the biggest subsonic wind tunnel in Belgium).

Our objective of performance is met: our first set of blades reached a power coefficient of 0.39 and the second 0.35. The first rotor has better characteristics than the majority of other small wind turbines while the second is average.

We also developed several theoretical concepts:

- We determined the specifications of our wind turbine. To find them we based our analysis on the limitations of the 3D printers we had at our disposal and the wind characteristics.
- We studied the thermal characteristic and the mechanical efficiency of the assembly gearhead-motor used in our prototype.
- Based on electrical arguments, we chose the more adapted generator for a potential second prototype. For this one, we explained how to characterize it in terms of torque, windings and magnets. Furthermore, we developed a *matlab* simulation based on a thermal model that allows to approximate the temperature in each generator component.
- The design of all the wind turbine pieces as well as the assembly between them was derived from what was previously developed. We designed several solutions for each part, among

others by developing *SolidWorks* simulations. Finally, the most appropriate solution was chosen.

## 7.2 Futur prospects

This master's thesis is very broad and uses a lot different branches of engineering. As a consequence, many parts of the study could be improved.

First, we only outlined the design of the ad-hoc generator. We chose its main characteristics but a complete study of the magnetic field is needed to assess its performances and decide if it is well adapted to the rotors we designed. It is also necessary to design specific parts to assemble the generator stator, generator rotor, nacelle and tower but most of them can be inspired from what is already made. Bearings must also be chosen.

About the aerodynamics, more airfoils could be tested thanks to the rapidity of 3D printing. Moreover, small additions could be made to the blades: wingtips to limit the strength of the tip vortex, turbulators to fix the transition point of the boundary layer on the blade, etc.

From a electronics point of view, another boost adapted at the generator could be developed. It will have to allow an easy use of the test bench and to reach all operating points of the wind turbine. To make the wind turbine autonomous, electronics could be designed and be placed in the nacelle or at the tower base. It would regulate the rotational speed to work at the correct tip speed ratio. It could be composed of sensors that will permit to measure wind speed, pressure or temperature.

To conclude, we can say that we reached the objectives of our thesis. Our wind turbine is fully operational and achieves the performance goals. We also developed a basis that can be used in prolongation of this master's thesis. 3D-printing offers lots of other perspectives and the home-made generator would make the wind-turbine entirely home-made.

# Bibliography

- [1] *200W, 5 blades small wind turbine and generator*. URL: [http://i00.i.aliimg.com/img/pb/776/104/014/1014104776\\_287.jpg](http://i00.i.aliimg.com/img/pb/776/104/014/1014104776_287.jpg) (visited on 05/06/2016).
- [2] *600W small wind generator for home*. URL: [http://www.alibaba.com/product-detail/600w-small-wind-generator-for-home\\_60149306967.html](http://www.alibaba.com/product-detail/600w-small-wind-generator-for-home_60149306967.html) (visited on 30/05/2016).
- [3] *Aeromax Lakota 900*. URL: <http://oxinssco.ir/sama-portal/index.php?FileBrowser/Download/id/lakota-900.pdf> (visited on 05/06/2016).
- [4] *Airfoil tools: XFOIL simulation data*. URL: <http://airfoiltools.com/> (visited on 04/06/2016).
- [5] Danish wind turbine association, ed. *Distribution de Weibull*. 5th May 2003. URL: [http://www.motiva.fi/myllarin\\_tuulivoima/windpower%20web/fr/tour/wres/weibull/index.htm](http://www.motiva.fi/myllarin_tuulivoima/windpower%20web/fr/tour/wres/weibull/index.htm) (visited on 02/06/2016).
- [6] Marc Bekemans. ‘Electronique de puissance: slides’. 2014.
- [7] Theodore L. Bergman et al. *Fundamentals of heat and mass transfer*. 2012.
- [8] GIORGIO BERTOTTI. ‘General Properties of Power Losses in Soft Ferromagnetic Materials’. In: *IEEE TRANSACTIONS ON MAGNETICS*, ().
- [9] Marshall L. Buhl et al. *A new empirical relationship between thrust coefficient and induction factor for the turbulent windmill state*. National Renewable Energy Laboratory Golden, CO, 2005.
- [10] Tony Burton et al. *Wind energy handbook*. John Wiley & Sons, 2001.
- [11] H. Cease et al. ‘Measurement of mechanical properties of three epoxy adhesives at cryogenic temperatures for CCD construction’. In: (6th Nov. 2006).
- [12] TY Chen and LR Liou. ‘Blockage corrections in wind tunnel tests of small horizontal-axis wind turbines’. In: *Experimental Thermal and Fluid Science* 35.3 (2011), pp. 565–569.
- [13] *Global Wind Report 2015: annual market update*. Global Wind Energy Council, 2016.
- [14] *DC motor EC 40 brushless, 120 Watt*. Maxon Motor ag. May 2013.
- [15] learning engineering, ed. *Brushless DC Motor, How it works*. URL: <http://www.learnengineering.org/2014/10/Brushless-DC-motor.html>.
- [16] Ian Gibson, David W Rosen, Brent Stucker et al. *Additive manufacturing technologies*. Springer, 2010.
- [17] P. Giguere and Michael S. Selig. ‘New airfoils for small horizontal axis wind turbines’. In: *Journal of solar energy engineering* 120.2 (1998), pp. 108–114.
- [18] Hermann Glauert. *The analysis of experimental results in the windmill brake and vortex ring states of an airscrew*. HM Stationery Office, 1926.
- [19] Hermann Glauert. *The elements of aerofoil and airscrew theory*. Cambridge University Press, 1983.
- [20] FAG OEM und Handel AG. *Roulement FAG: Roulement à billes, Roulements à rouleaux, Paliers, Accessoires*. 1995.
- [21] Claude Hazard, André Ricordeau and Claude Corbet. *Méthode active de dessin technique*. 2003.
- [22] Hiroyuki Hirahara et al. ‘Testing basic performance of a very small wind turbine designed for multi-purposes’. In: *Renewable energy* 30.8 (2005), pp. 1279–1297.

- [23] von Karman Institute, ed. *3-meter diameter wind tunnel L-1A*. 2016. URL: <https://www.vki.ac.be/index.php/research-consulting-mainmenu-107/facilities-other-menu-148/low-speed-wt-other-menu-151/57-3-meter-diameter-wind-tunnel-l-1a> (visited on 24/05/2016).
- [24] Ravi Anant Kishore, Thibaud Coudron and Shashank Priya. ‘Small-scale wind energy portable turbine (SWEPT)’. In: *Journal of Wind Engineering and Industrial Aerodynamics* 116 (2013), pp. 21–31.
- [25] Ravi Anant Kishore and Shashank Priya. ‘Design and experimental verification of a high efficiency small wind energy portable turbine (SWEPT)’. In: *Journal of Wind Engineering and Industrial Aerodynamics* 118 (2013), pp. 12–19.
- [26] Buyung Kosasih and Andrea Tondelli. ‘Experimental study of shrouded micro-wind turbine’. In: *Procedia Engineering* 49 (2012), pp. 92–98.
- [27] Andreas Krings et al. ‘Measurement and Modeling of Iron Losses in Electrical Machines’. In: *Laboratory of Electrical Energy Conversion (E2C), Royal Institute of Technology (KTH)* ().
- [28] NIST Physical Measurement Laboratory, ed. *Blockage and wall effects on air speed calibrations*. 2014. URL: [http://www.nist.gov/pml/div685/grp02/wall\\_and\\_blockage\\_effects.cfm](http://www.nist.gov/pml/div685/grp02/wall_and_blockage_effects.cfm) (visited on 04/06/2016).
- [29] B. D. McGranahan and M. S. Selig. *Wind tunnel aerodynamic tests of six airfoils for use on small wind turbines*. Golden, CO: National Renewable Energy Laboratory, 2004.
- [30] Institut Royal Météorologique, ed. *Normales mensuelles à Uccle*. URL: [http://www.meteo.be/meteo/view/fr/360955-Normales+mensuelles.html#ppt\\_5238274](http://www.meteo.be/meteo/view/fr/360955-Normales+mensuelles.html#ppt_5238274) (visited on 05/06/2016).
- [31] MAXON motor. *Maxon Program 2016/17*. 2016.
- [32] Janne Nerg, Marko Rilla and Juha Pyrhonen. ‘Thermal analysis of radial-flux electrical machines with a high power density’. In: *Industrial Electronics, IEEE Transactions on* 55.10 (2008), pp. 3543–3554.
- [33] S. Andrew Ning. ‘A simple solution method for the blade element momentum equations with guaranteed convergence’. In: *Wind Energy* 17.9 (2014), pp. 1327–1345.
- [34] TSI Airflow Note. ‘Traversing a Duct to Determine Average Air Velocity’. In: *TI-106* (2014).
- [35] Pragasen Pillay and Ramu Krishnan. ‘Application Characteristics of Permanent Magnet Synchronous and Brushless dc Motors for Servo Drives’. In: *IEEE* ().
- [36] Polymaker. *PolyMax PLA Technical Data Sheet*. URL: [http://www.polymaker.com/wp-content/uploads/2015/06/PolyMax-PLA\\_TDS-v1.pdf](http://www.polymaker.com/wp-content/uploads/2015/06/PolyMax-PLA_TDS-v1.pdf) (visited on 05/06/2016).
- [37] Ayman M. EL-Refaie. ‘Fractional-Slot Concentrated-Windings Synchronous Permanent Magnet Machines: Opportunities and Challenges’. In: (1st Sept. 2009).
- [38] Thomas Reichert, Thomas Nussbaumer and Johann W. Kolar. ‘Torque scaling laws for interior and exterior rotor permanent magnet machines’. In: *A A 3* (2009), p. 1.
- [39] *Reprap Windturbine*. URL: <http://www.reprap-windturbine.com/index.php?id=10&L=1> (visited on 05/06/2016).
- [40] *Rutland 504 e-furl Windcharger*. URL: <http://www.marlec.co.uk/product/12v-rutland-504-e-furl-windcharger/> (visited on 05/06/2016).
- [41] *Rutland 914i Windcharger*. URL: <http://www.marlec.co.uk/product/rutland-914i/> (visited on 04/06/2016).
- [42] Michael S. Selig et al. *Summary of Low-Speed Airfoil Data - Vol. 1*. Virginia Beach, VA: SoarTech Publications, 1995. 292 pp. ISBN: 978-0-9646747-1-4.
- [43] Michael S. Selig et al. *Summary of Low-Speed Airfoil Data - Vol. 2*. Virginia Beach, VA.: SoarTech Publications, May 1996. ISBN: 978-0-9646747-2-1.
- [44] Michael S. Selig et al. *Summary of Low-Speed Airfoil Data - Vol. 3*. Virginia Beach, VA: SoarTech Publications, Dec. 1997. ISBN: 978-0-9646747-3-8.

- [45] *Skystream 3.7*. URL: <http://www.xzeres.com/wind-turbine-products/xzeres-skystream-3-7wind-turbine/> (visited on 10/06/2016).
- [46] Dan M. Somers. ‘The S833, S834, and S835 Airfoils’. In: *National Renewable Energy Laboratory, NREL/SR-500-36340, Boulder, CO* (2005).
- [47] Stratasys. *ABSplus-P430 Production grade thermoplastic for 3D printers: datasheet*. 2015. URL: [http://usglobalimages.stratasys.com/Main/Files/Material\\_Spec\\_Sheets/MSS\\_FDM\\_ABSplusP430.pdf](http://usglobalimages.stratasys.com/Main/Files/Material_Spec_Sheets/MSS_FDM_ABSplusP430.pdf) (visited on 05/06/2016).
- [48] *Superwind 350*. URL: <http://www.superwind.com/swe/index.htm> (visited on 10/06/2016).
- [49] University College Dublin. *HiWinds: High Resolution Forecasts for Wind Energy Applications*. URL: <http://mathsci.ucd.ie/~hiwinds/why-frame2.html> (visited on 10/06/2016).
- [50] Nicolas Van Naemen. ‘Nouvelles technologies de fabrication additive pour le prototypage rapide de dispositifs mécatroniques’. MA thesis. Université Catholique de Louvain, 2015.
- [51] Larry A. Viterna and Robert D. Corrigan. ‘Fixed pitch rotor performance of large horizontal axis wind turbines’. In: *DOE/NASA Workshop on Large Horizontal Axis Wind Turbines* (Sept. 1982).
- [52] J. Anthoine (von Karman Institute), D. Olivari and D. Portugaels. ‘Wind-tunnel blockage effect on drag coefficient of circular cylinders’. In: *Wind and Structures* 12.6 (Nov. 2009), pp. 541–551. DOI: 10.12989/was.2009.12.6.541.
- [53] Wikipedia. URL: [https://en.wikipedia.org/wiki/Fused\\_deposition\\_modeling](https://en.wikipedia.org/wiki/Fused_deposition_modeling) (visited on 30/05/2016).
- [54] Wikipedia. *Nature of laminar separation bubble on a turbine blade*. 27th May 2013. URL: [https://en.wikipedia.org/wiki/File:Nature\\_of\\_laminar\\_separation\\_bubble\\_on\\_a\\_turbine\\_blade.gif](https://en.wikipedia.org/wiki/File:Nature_of_laminar_separation_bubble_on_a_turbine_blade.gif) (visited on 04/06/2016).
- [55] G.A. Williamson et al. *Summary of Low-Speed Airfoil Data - Vol. 5*. 2012. URL: [http://m-selig.ae.illinois.edu/uiuc\\_lsat/Low-Speed-Airfoil-Data-V5.pdf](http://m-selig.ae.illinois.edu/uiuc_lsat/Low-Speed-Airfoil-Data-V5.pdf).
- [56] *Wind Power Generator, generator*. URL: [http://www.alibaba.com/product-detail/200w-5-blades-small-wind-turbine\\_60062028793.html](http://www.alibaba.com/product-detail/200w-5-blades-small-wind-turbine_60062028793.html) (visited on 30/05/2016).
- [57] David Wood. *Small wind turbines*. Springer, 2011.



# Appendices



# Appendix A

## Prototype design

### A.1 Nacelle and duct assembly

The duct allows us to potentially beat the Betz limit but it makes the design more complex. The duct has to turn with the nacelle because it has to be always in front of the wind.

We considered two different designs (figure A.1 and figure A.2). In the first case, the duct is printed with the blades end. Duct parts are bolted together. In the second case, there is no contact between the duct and the blades. The duct is maintained in position by the nacelle thanks to support bars.

For the second proposition, we considered two different fixation types. The difference between them is the way to attach the support bars to the nacelle. In one, the bar end is a part of the nacelle. In the other one, the bar end is superimposed at the nacelle surface. In both cases, support bars are bolted at the nacelle.

A comparative table between all the propositions is present in table A.1.

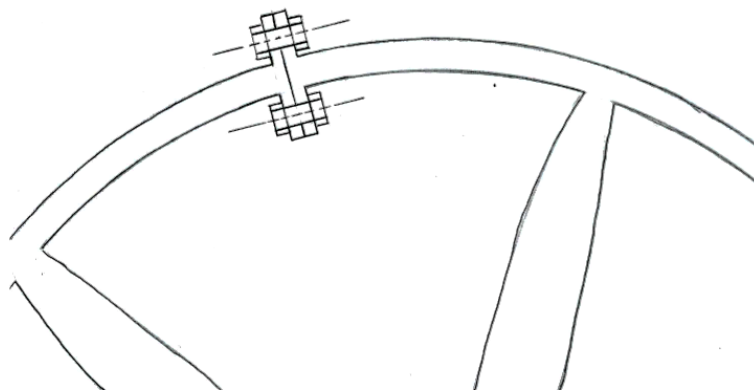


Figure A.1: Duct proposition #1

As we use the Up! Mini to print all the pieces, it turns out that it is unrealistic to print a duct. The printing area of the Up! Mini is too small for such a huge piece. For example, if we create a wind turbine with a 350 mm radius, we would need to print more or less 18 pieces. Moreover these pieces has to be bolted together. The assembly wouldn't be exactly symmetrical due to imperfections of 3D printing and differences in bolted assemblies.

	Pros	Cons
Proposition #1	<ul style="list-style-type: none"> <li>• Less to print</li> <li>• Easy to design</li> </ul>	<ul style="list-style-type: none"> <li>• Additive mass at the blades end</li> <li>• Radial stresses more important</li> </ul>
Proposition #2	<ul style="list-style-type: none"> <li>• Maintain nacelle aerodynamics design</li> <li>• No contact between duct and blades (no additive mass and radial stresses)</li> </ul>	<ul style="list-style-type: none"> <li>• More to print</li> <li>• Gap between duct and blades (dependent on support bar rigidity)</li> <li>• Nacelle shape without duct</li> </ul>
Proposition #3	<ul style="list-style-type: none"> <li>• Nacelle shape without duct aerodynamical</li> <li>• No contact between duct and blades (no additive mass and radial stresses)</li> </ul>	<ul style="list-style-type: none"> <li>• Nacelle aerodynamical shape disrupted by the fixation</li> <li>• Gap between duct and blades (dependent on support bar rigidity)</li> <li>• More to print</li> </ul>

Table A.1: Comparison of duct designs

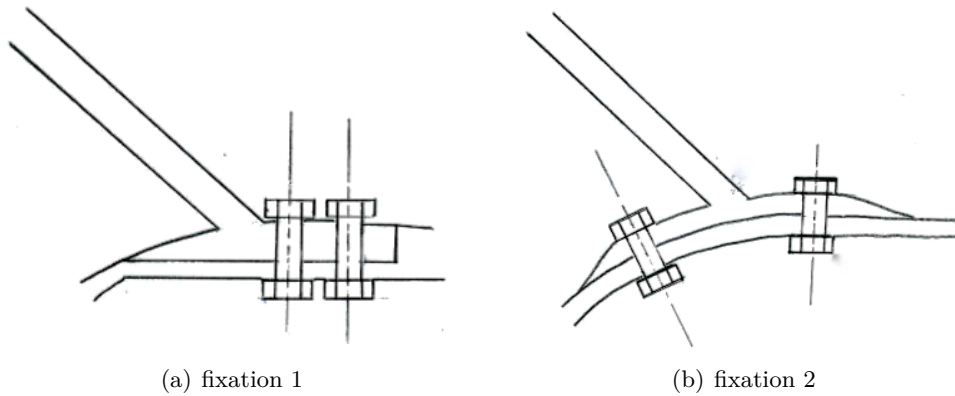


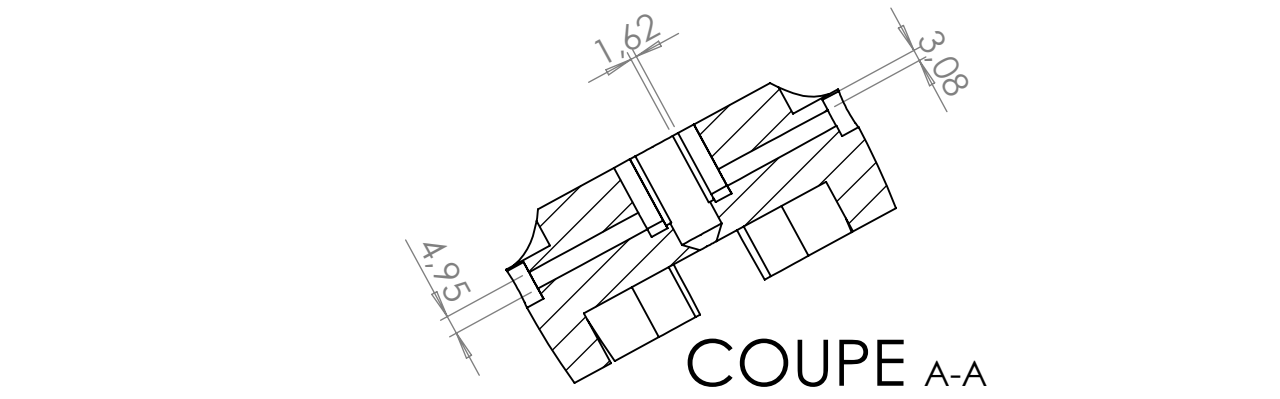
Figure A.2: Duct proposition #2

If we use the first proposition, it introduces rotating unbalance that would be difficult to compensate.

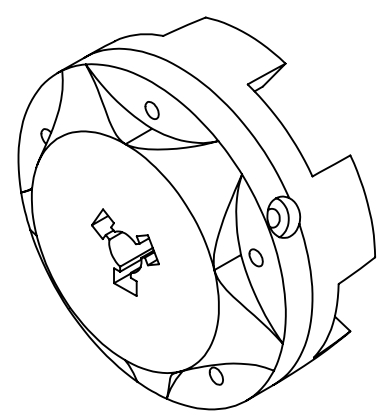
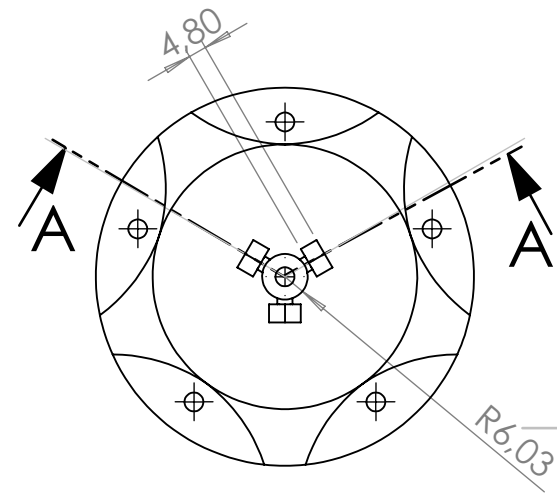
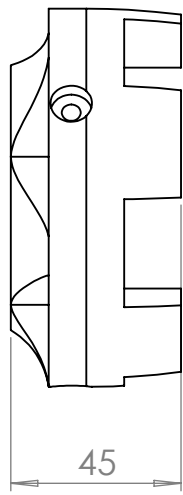
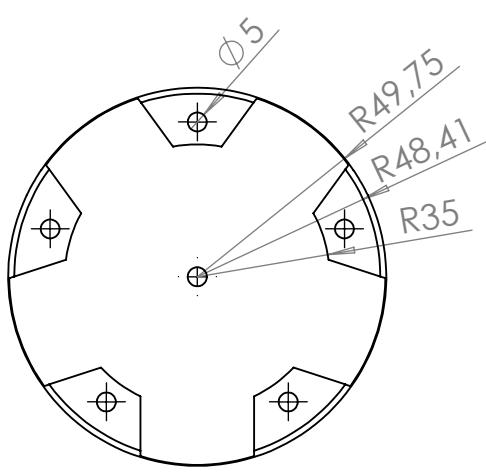
If we use the second one, the support bars, an assembly of several pieces, will bend under the total duct mass. So we would have to increase the gap between the blades and the duct. It would result that the duct won't be so effective.

## **Appendix B**

# **Technical drawings**



COUPE A-A



NAMES - AUTHORS		DATE	TITRE:
IGOT Pierrick		05/06/16	Technical Drawing piece
SNYERS Charles		Unités mm	
MATERIAL:		No. DE PLAN	150
ABS		Axis	
MASS: 79.85g	SCALE: 1:2		A4

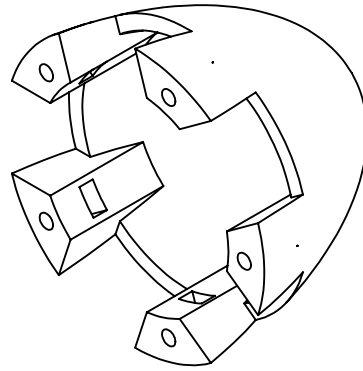
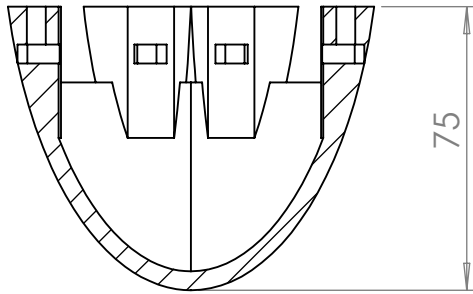
4 3 2 1

F

F

E

E

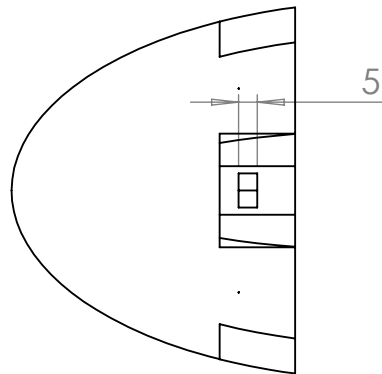
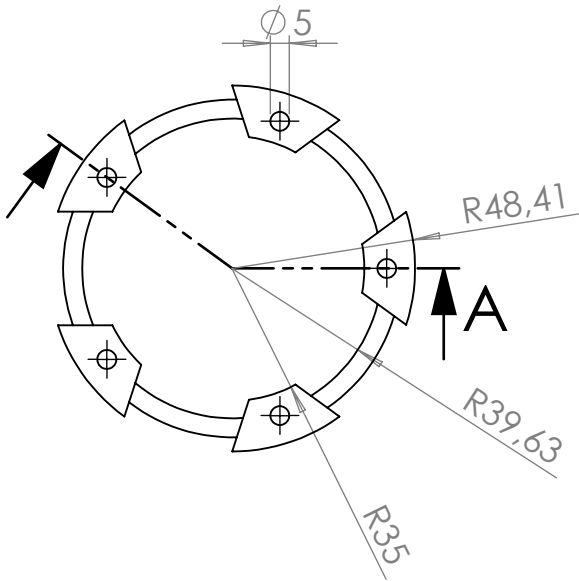


COUPE A-A

D

D

A



C

C

B

B

A

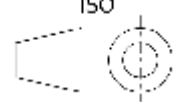
A

NAMES - AUTHORS	DATE	TITRE:
IGOT Pierrick	05/06/16	Technical Drawing piece
SNYERS Charles		
	Unités	
	mm	

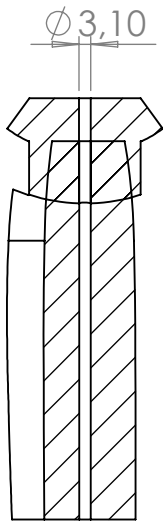
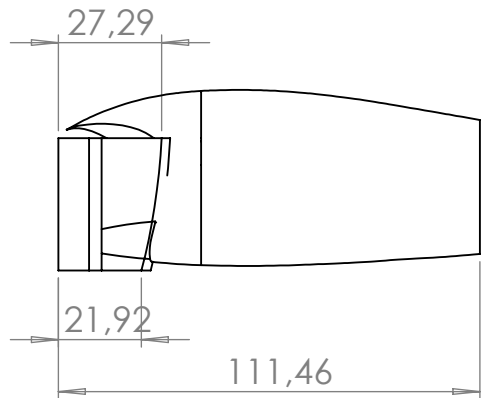
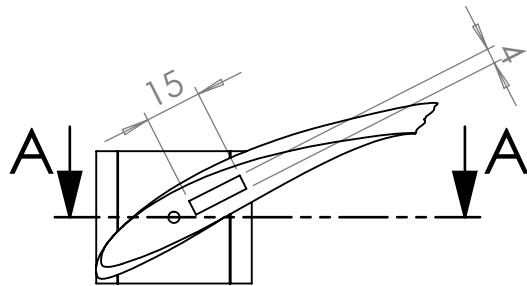
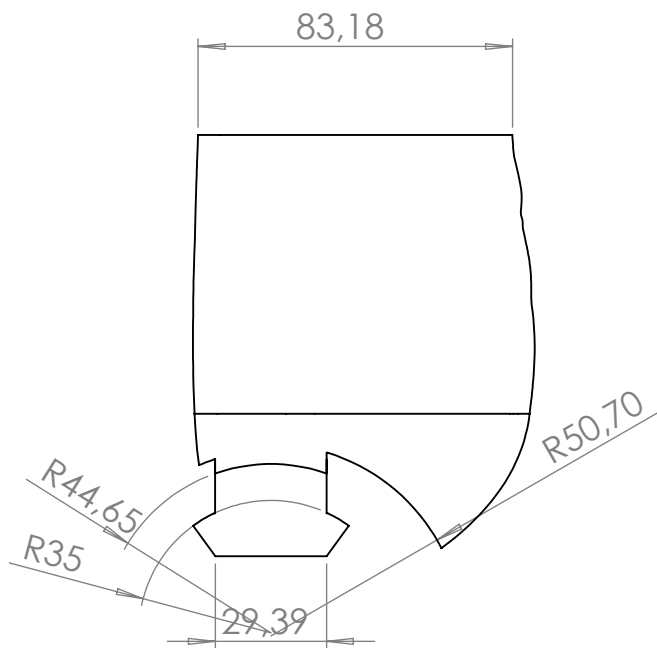
MATERIAL:	No. DE PLAN
ABS	Hub

MASS: 79.85g	SCALE: 1:2	A4
--------------	------------	----

150
-----

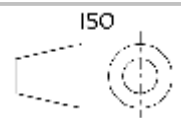


4 3 2 1



COUPE A-A

NAMES - AUTHORS	DATE	TITRE:
IGOT Pierrick	05/06/16	Technical Drawing piece
SNYERS Charles		
	Unités	
	mm	
MATERIAL:	ABS	No. DE PLAN
		PALE part 1
MASS: 79.85g	SCALE: 1:2	A4



4 3 2 1

F

F

E

E

D

D

C

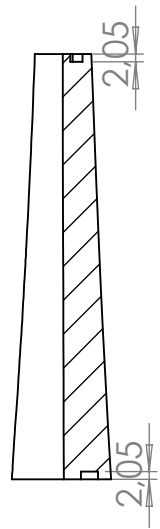
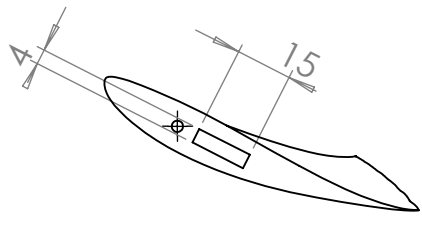
C

B

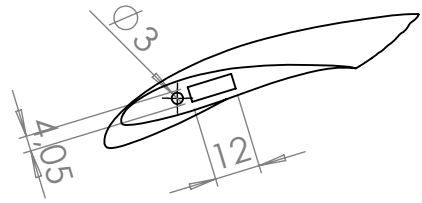
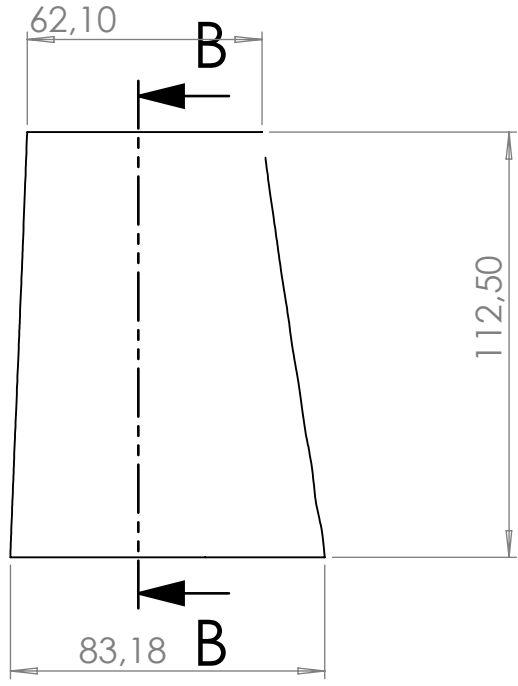
B

A

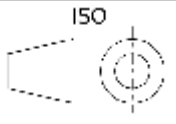
A



COUPE B-B



NAMES - AUTHORS	DATE	TITRE:
IGOT Pierrick	05/06/16	Technical Drawing piece
SNYERS Charles		
	Unités	
	mm	
MATERIAL:		No. DE PLAN
ABS		Blade part2
MASS: 79.85g	SCALE:1:2	A4



4 3 2 1

4 3 2 1

F

F

E

E

D

D

C

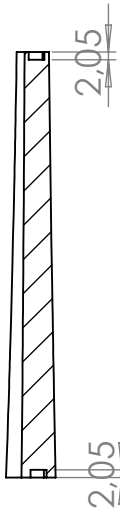
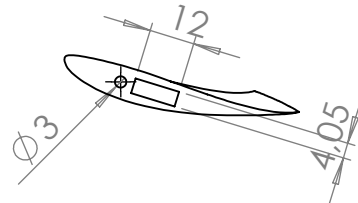
C

B

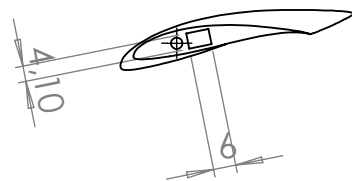
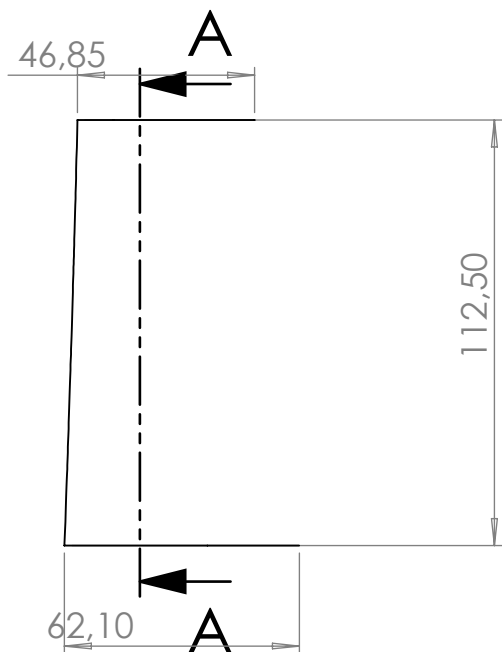
B

A

A



COUPE A-A



NAMES - AUTHORS	DATE	TITRE:
IGOT Pierrick	05/06/16	Technical Drawing piece
SNYERS Charles		
	Unités	No. DE PLAN
	mm	
MATERIAL:	ABS	BLADE Part3
MASS: 79.85g	SCALE:1:2	
	A4	150

4 3 2 1

4 3 2 1

F

F

E

E

D

D

C

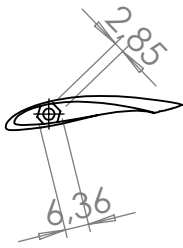
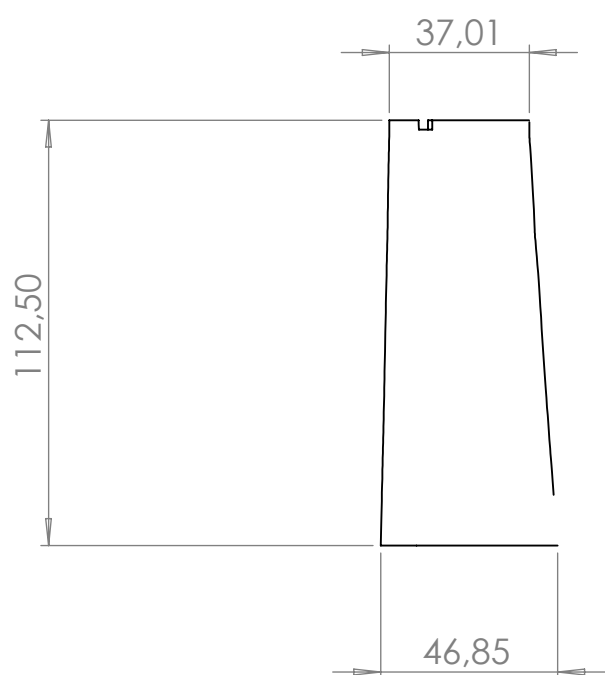
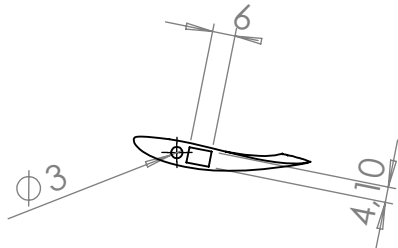
C

B

B

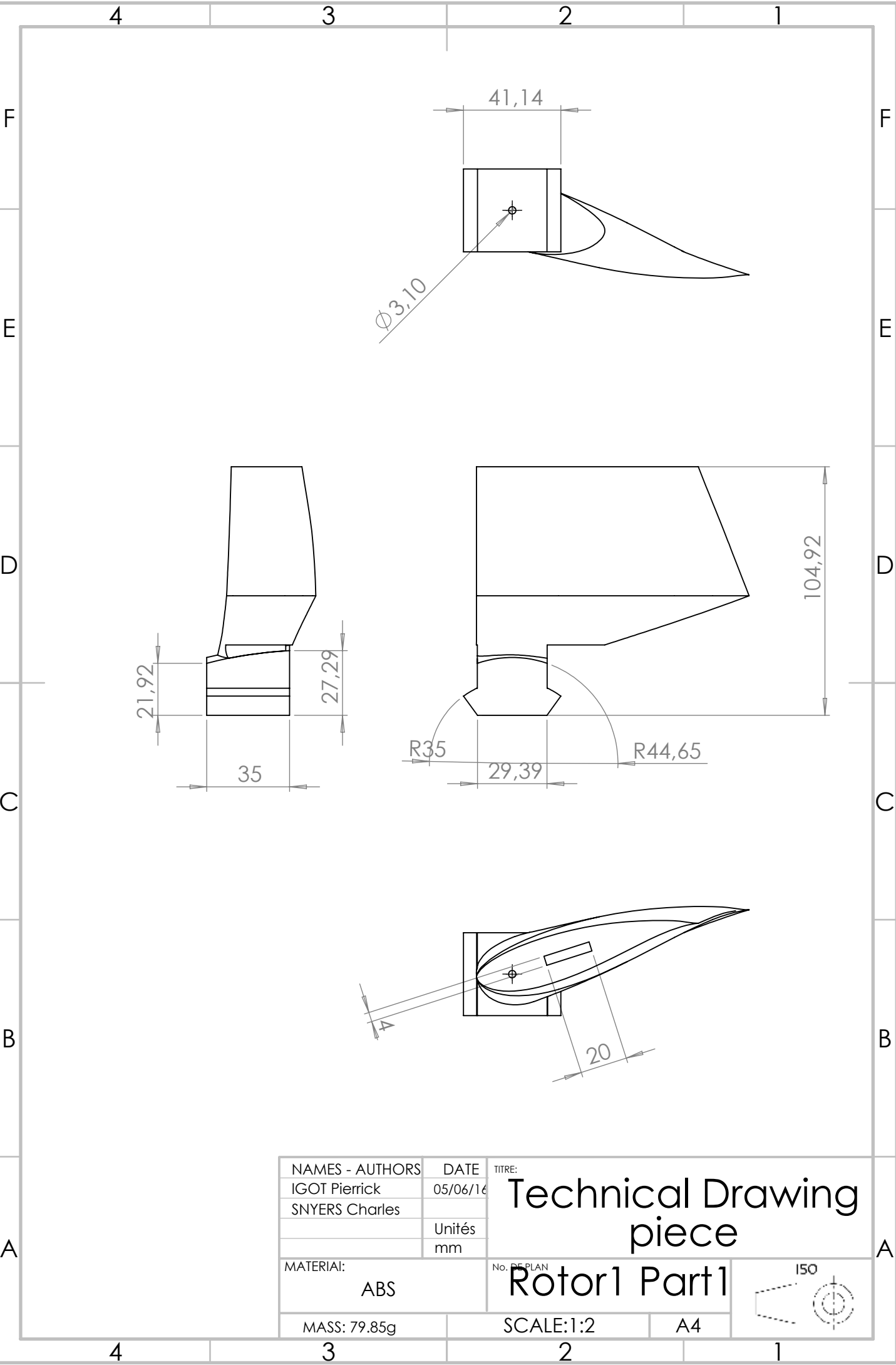
A

A



NAMES - AUTHORS		DATE	TITRE:
IGOT Pierrick		05/06/16	Technical Drawing piece
SNYERS Charles			
		Unités	No. DE PLAN <b>BLADE part4</b>
		mm	
MATERIAI:		150	
ABS			
MASS: 79.85g	SCALE:1:2		A4

4 3 2 1



NAMES - AUTHORS	DATE	TITRE:
IGOT Pierrick	05/06/16	Technical Drawing piece
SNYERS Charles		
	Unités	
	mm	

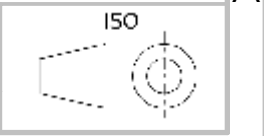
MATERIAL: ABS

No. DE PLAN  
**Rotor1 Part1**

MASS: 79.85g

SCALE: 1:2

A4



A

A

B

B

C

C

D

D

E

E

F

F

4

3

2

1

4

3

2

1

4 3 2 1

F

F

E

E

D

D

C

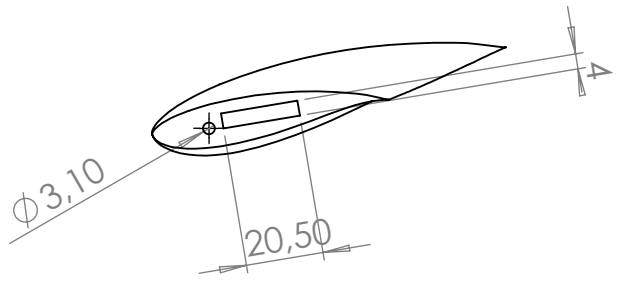
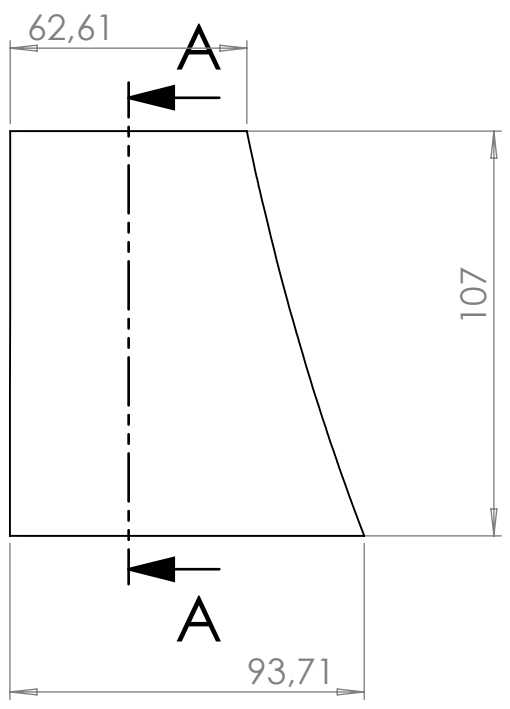
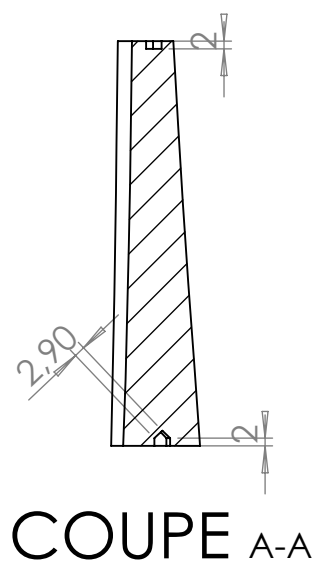
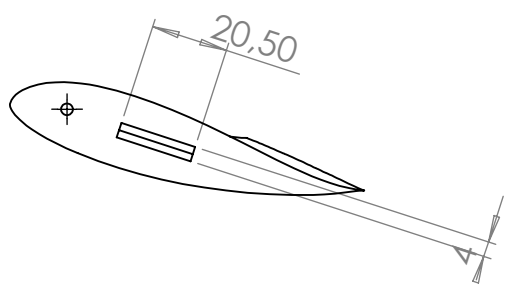
C

B

B

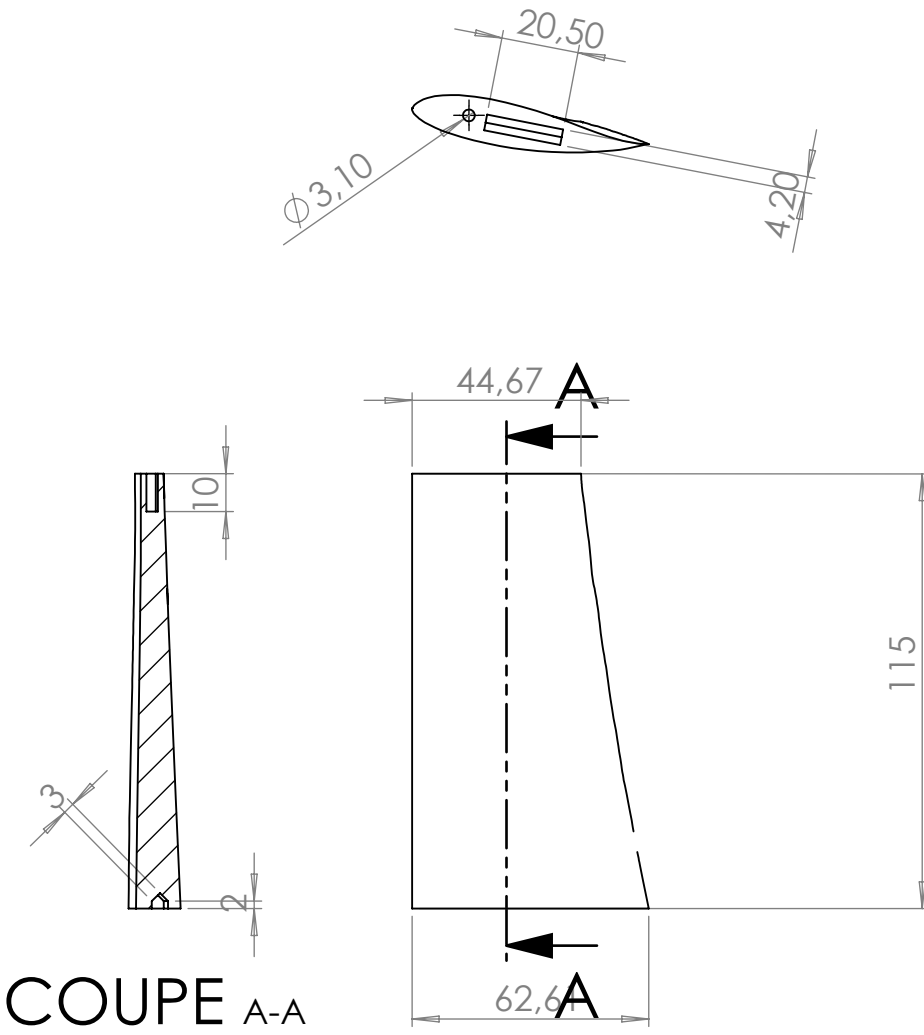
A

A



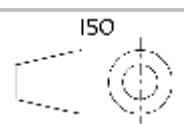
NAMES - AUTHORS	DATE	TITRE:
IGOT Pierrick	05/06/16	Technical Drawing piece
SNYERS Charles		
	Unités	No. DE PLAN
	mm	
MATERIAL:	ABS	Rotor1 Part2
MASS: 79.85g		
	SCALE:1:2	A4
		150

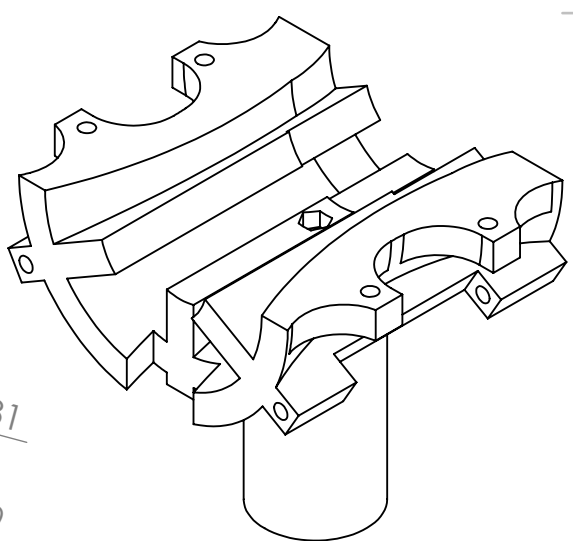
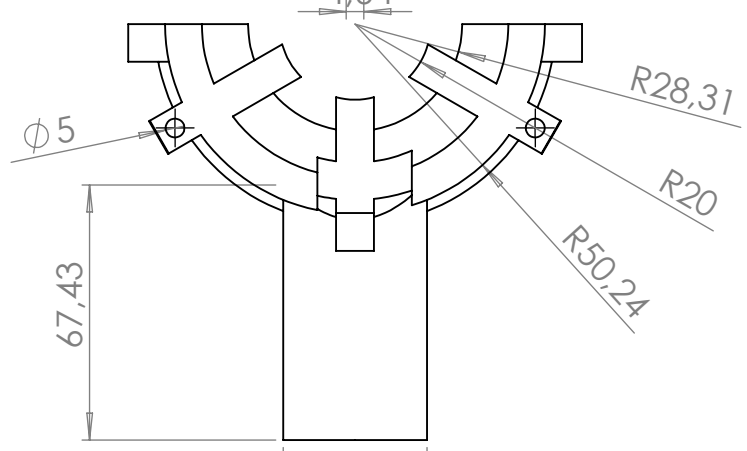
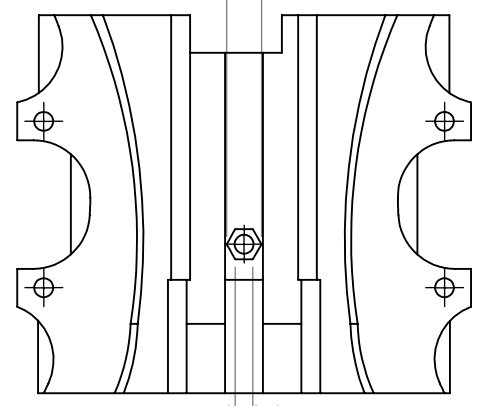
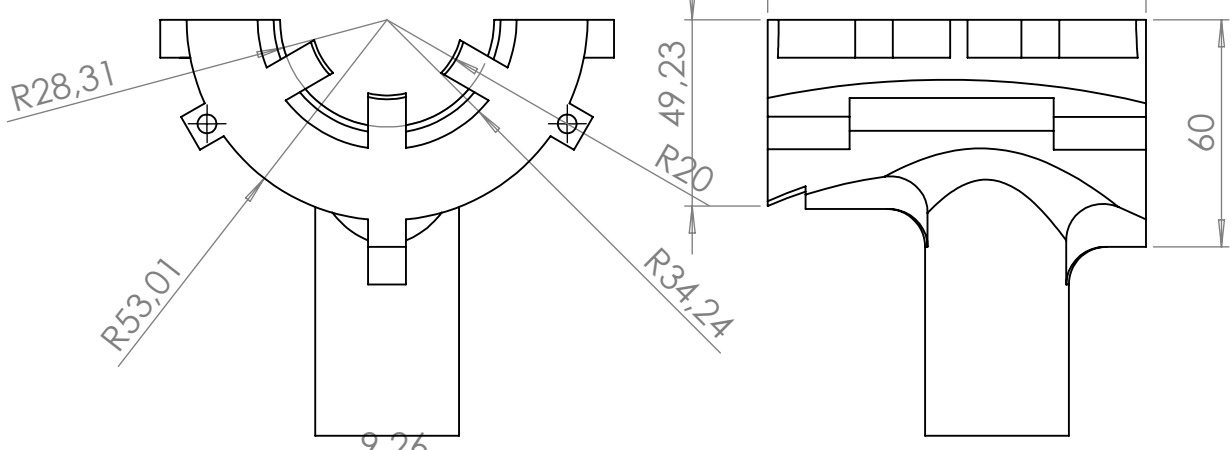
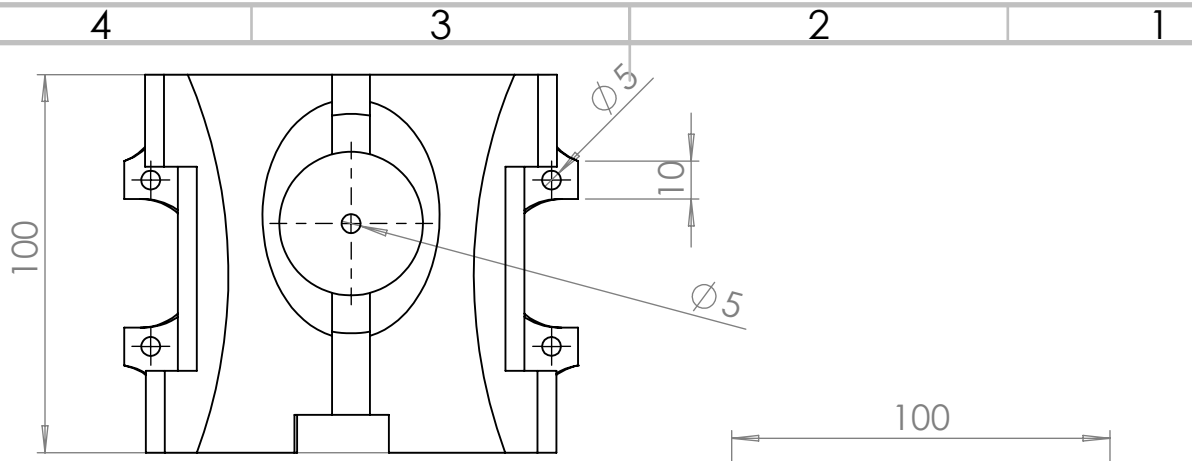
4 3 2 1



COUPE A-A

NAMES - AUTHORS	DATE	TITRE:
IGOT Pierrick	05/06/16	Technical Drawing piece
SNYERS Charles		
	Unités	No. DE PLAN
	mm	
MATERIAL:	ABS	Rotor1 Part3
MASS: 79.85g	SCALE: 1:2	A4





Ø 38

NAMES - AUTHORS	DATE	TITRE:
IGOT Pierrick	05/06/16	Technical Drawing piece
SNYERS Charles		
	Unités	
	mm	

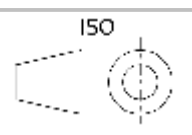
MATERIAI:  
ABS

No. DE PLAN  
Nacel Down

MASS: 79.85g

SCALE: 1:2

A4

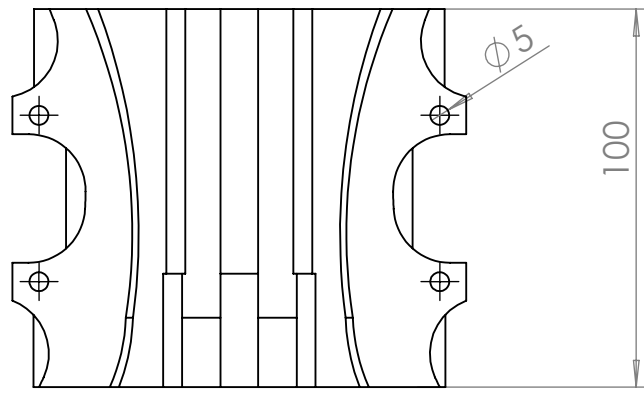


4 3 2 1

4 3 2 1

F

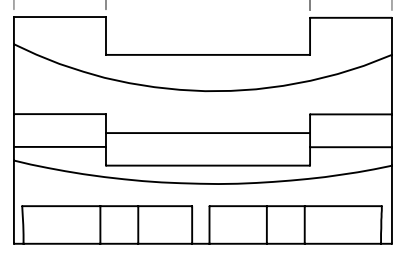
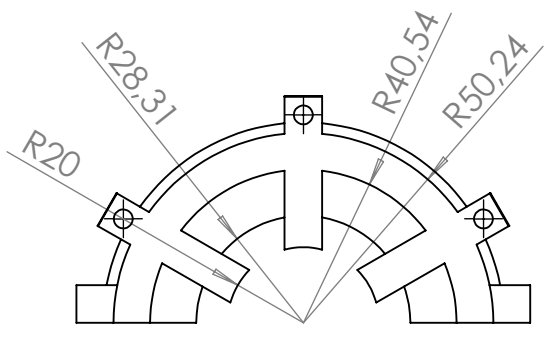
F



100  
24,40 53,95 21,65

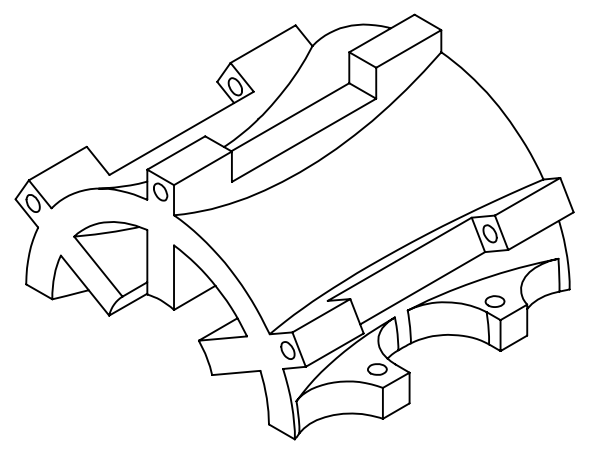
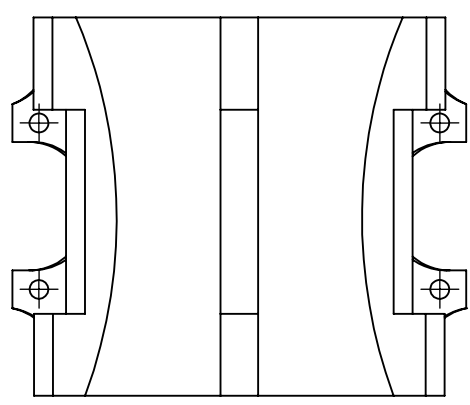
E

E



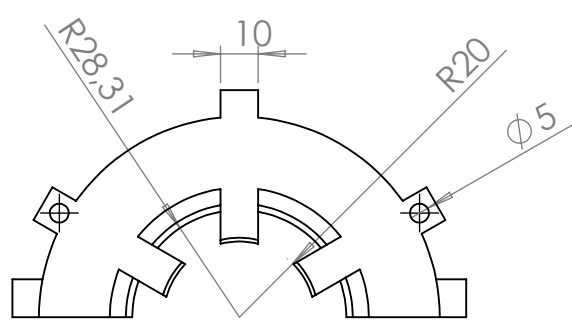
D

D



C

C



B

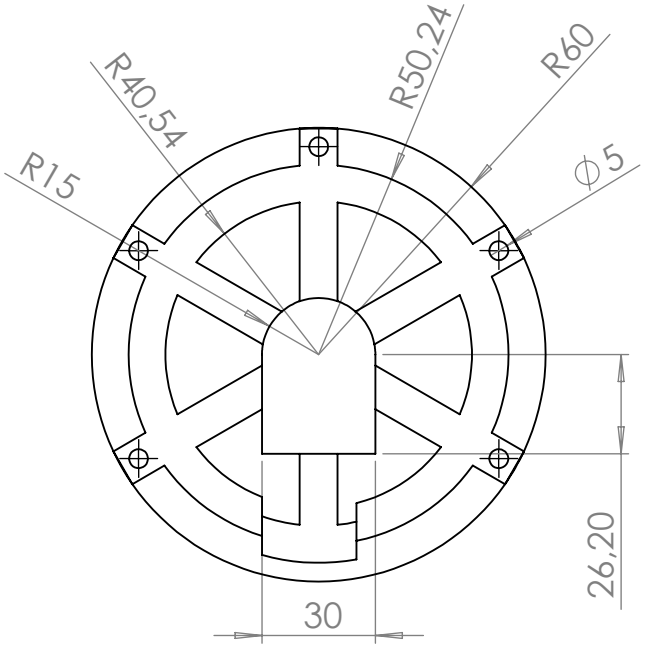
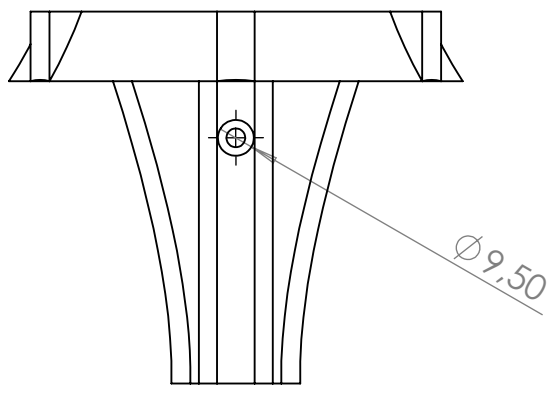
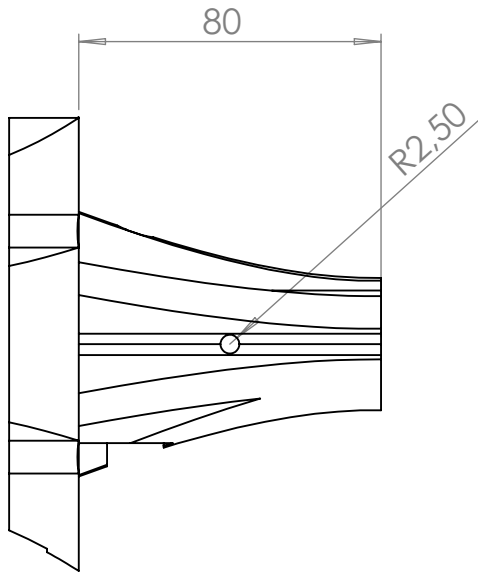
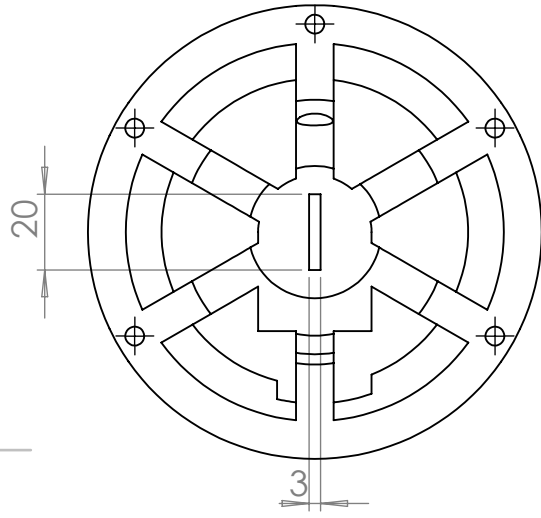
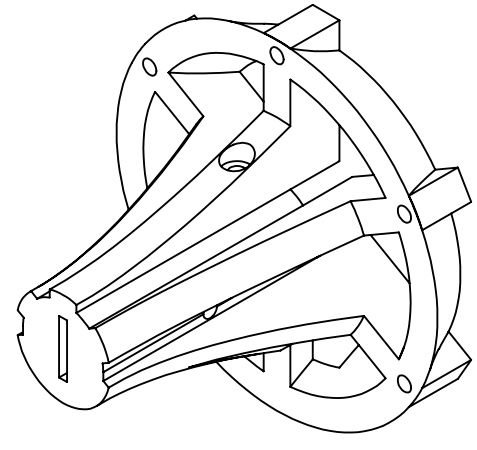
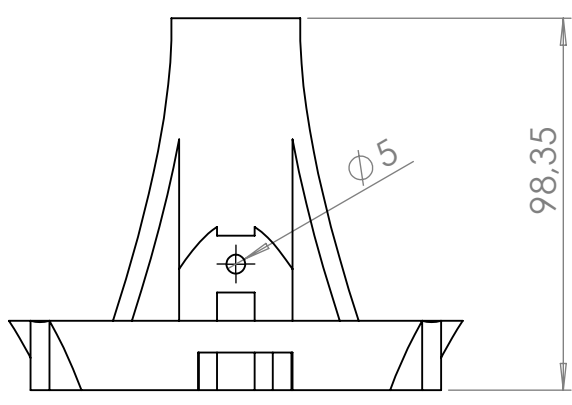
B

A

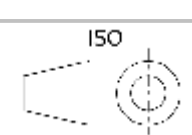
A

NAMES - AUTHORS		DATE	TITRE: <b>Technical Drawing piece</b>
IGOT Pierrick SNYERS Charles		05/06/16	
		Unités mm	
MATERIAI: <b>ABS</b>		No. DE PLAN	150 
MASS: 79.85g		SCALE:1:2	

4 3 2 1



NAMES - AUTHORS		DATE	TITRE:
IGOT Pierrick		05/06/16	
SNYERS Charles			Technical Drawing piece
		Unités mm	
MATERIAL:		No. DE PLAN	
ABS		Part Tail fin	
MASS: 79.85g		SCALE: 1:2	A4



4 3 2 1

F

F

E

E

D

D

C

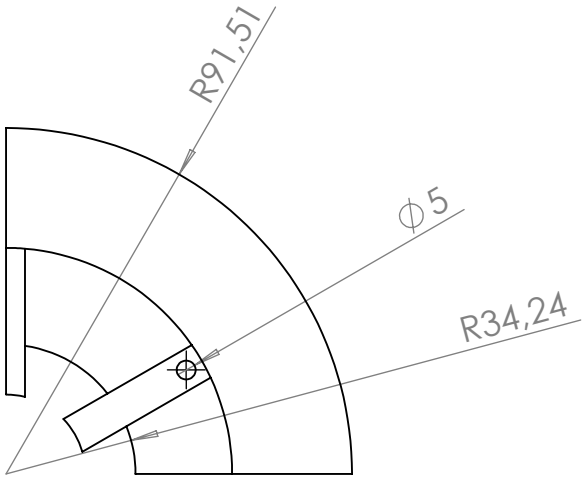
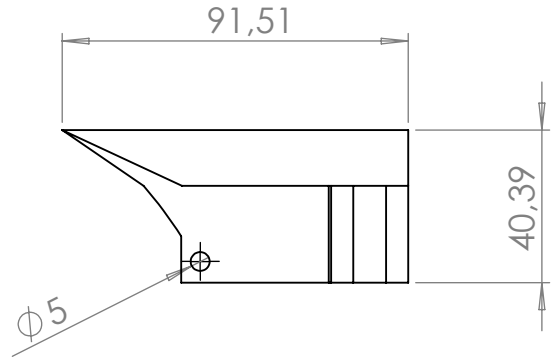
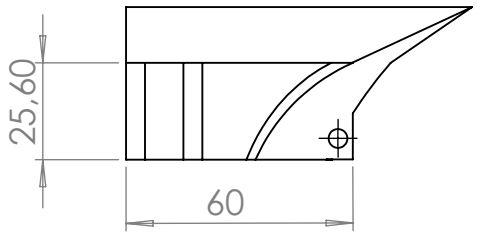
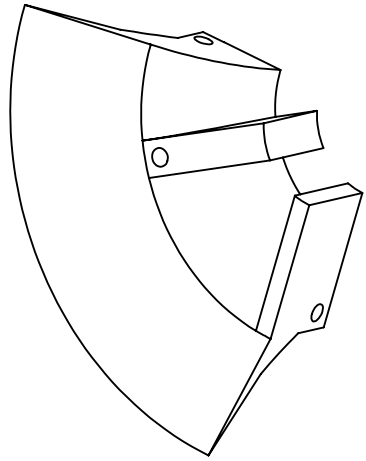
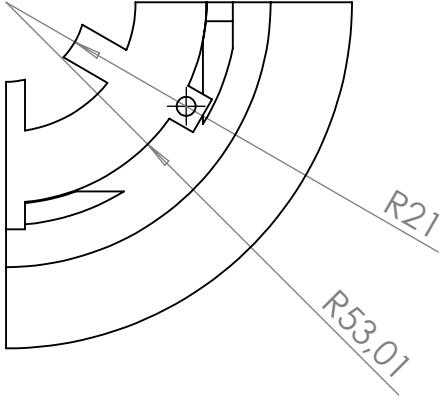
C

B

B

A

A



NAMES - AUTHORS		DATE	TITRE: <b>Technical Drawing piece</b>
IGOT Pierrick		05/06/16	
SNYERS Charles			
		Unités	No. DE PLAN <b>Venturi 1</b>
		mm	
MATERIAI: <b>ABS</b>		150	
MASS: 79.85g	SCALE:1:2		A4

4 3 2 1

4 3 2 1

F

F

E

E

D

D

C

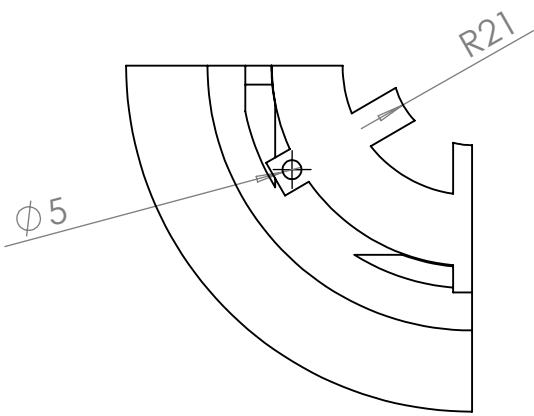
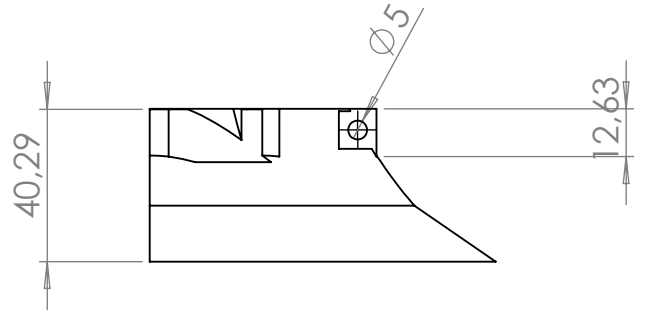
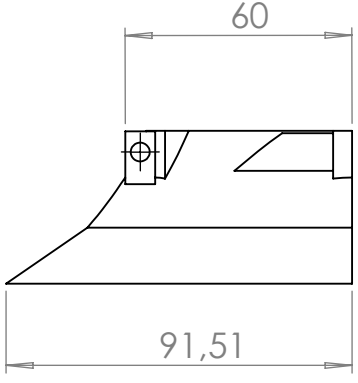
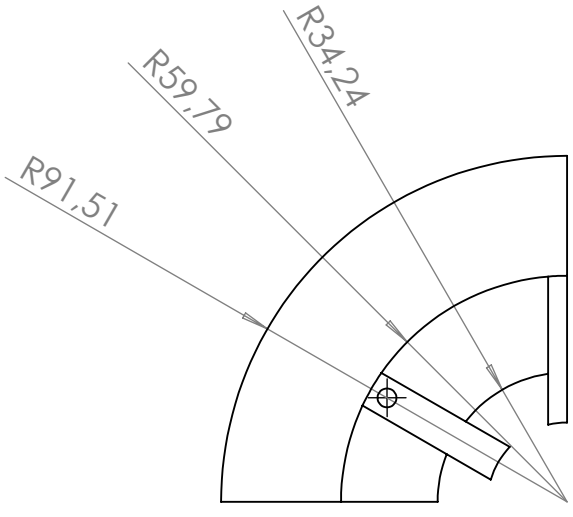
C

B

B

A

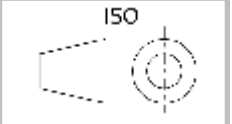
A



NAMES - AUTHORS	DATE	TITRE:
IGOT Pierrick	05/06/16	Technical Drawing piece
SNYERS Charles	Unités mm	

MATERIAI:  
ABS

No. DE PLAN  
Venturi2



MASS: 79.85g

SCALE: 1:2

A4

4 3 2 1



# Appendix C

## Tests

### C.1 Measuring instruments

	Measuring instrument	Range	Accuracy	Resolution
Wind speed (VKI)	Differential pressure sensor AMSYS 5812	0 - 5.17 mbar	$\pm 1.5 \%$	0.05 %
Wind speed (UCL LEFT)	TSI VelociCalc 8384	0 - 50 m/s	$\pm 0.15$ m/s or 3% of reading	0.01 m/s
Rotational speed	Incremental encoder CUI AMT-10	0 - 15000 rpm	$0.25^\circ$	0.2 %
Current	Current probe Tektronix TCP305A with amplifier TCPA300	0 - 25 A	$\pm 1\%$	-
Voltage	Multimeter LX64	0 - 1000 V	$\pm 0.5\%$	+ 1 digit
Temperature	SainSonic SS5380 Non-Contact IR Thermometer Gun	-50 - 280°C	$\pm 1.5^\circ\text{C}$	$0.1^\circ\text{C}$

Table C.1: Measuring instruments

### C.2 Results at the von Karman Institute

VKI: rotor 1, $V_0 = 6.04\text{m/s}$					
$\lambda$	$\Omega$ [rpm]	$U_{in}$ [V]	$I_{in}$ [A]	$P_{elec}$ [W]	$C_P$ [-]
0.50	82.50	2.10	0.09	0.18	0.02
0.99	164.50	7.10	0.10	0.71	0.05
1.49	247.00	12.30	0.12	1.54	0.08
1.99	331.00	17.15	0.19	3.26	0.14
2.00	332.00	17.20	0.19	3.27	0.15
2.24	373.00	19.50	0.25	4.88	0.20
2.49	414.00	21.70	0.38	8.25	0.29
2.74	455.00	24.30	0.35	8.63	0.31

2.80	466.00	24.60	0.40	9.84	0.35
2.85	474.00	25.15	0.38	9.56	0.34
2.91	483.00	25.60	0.36	9.22	0.34
3.01	500.00	26.90	0.30	8.07	0.31
3.49	580.00	32.20	0.21	6.76	0.30
VKI: rotor 1, $V_0 = 8\text{m/s}$					
$\lambda$	$\Omega$ [rpm]	$U_{in}$ [V]	$I_{in}$ [A]	$P_{elec}$ [W]	$C_P$ [-]
0.50	110.00	3.70	0.26	0.96	0.02
0.54	118.00	10.60	0.35	3.71	0.05
1.49	328.00	15.00	0.42	6.30	0.10
1.98	436.00	22.00	0.54	11.88	0.17
2.47	544.00	28.86	0.90	25.97	0.34
2.68	590.00	31.00	0.95	29.45	0.39
2.78	613.00	32.00	0.92	29.44	0.39
2.88	635.00	32.80	0.90	29.52	0.39
2.95	650.00	36.00	0.72	25.92	0.35
2.97	653.00	34.40	0.82	28.21	0.38
3.07	675.00	36.10	0.73	26.35	0.36
3.16	695.00	37.50	0.72	27.00	0.37
3.18	700.00	38.16	0.70	26.71	0.37
VKI: rotor 1, $V_0 = 10\text{m/s}$					
$\lambda$	$\Omega$ [rpm]	$U_{in}$ [V]	$I_{in}$ [A]	$P_{elec}$ [W]	$C_P$ [-]
0.50	138.00	4.10	0.48	1.97	0.02
1.00	275.00	13.50	0.68	9.18	0.06
1.50	414.00	20.70	0.85	17.59	0.12
1.97	543.00	30.30	0.96	29.09	0.19
2.46	677.00	34.00	1.57	53.38	0.35
2.71	745.00	38.50	1.50	57.75	0.38
2.76	760.00	40.40	1.50	60.60	0.39
2.85	784.00	40.50	1.43	57.91	0.38
2.95	812.00	42.40	1.37	58.09	0.38
VKI: rotor 2, $V_0 = 4\text{m/s}$					
$\lambda$	$\Omega$ [rpm]	$U_{in}$ [V]	$I_{in}$ [A]	$P_{elec}$ [W]	$C_P$ [-]
1.38	112.00	3.60	0.18	0.67	0.07
2.05	167.00	7.20	0.27	1.91	0.15
2.76	224.00	10.00	0.34	3.40	0.24
3.40	276.00	13.50	0.28	3.73	0.27
3.51	285.00	13.70	0.28	3.84	0.28
3.75	305.00	16.70	0.24	4.01	0.30
4.12	335.00	17.30	0.15	2.60	0.24
VKI: rotor 2, $V_0 = 7\text{m/s}$					
$\lambda$	$\Omega$ [rpm]	$U_{in}$ [V]	$I_{in}$ [A]	$P_{elec}$ [W]	$C_P$ [-]
0.67	96.00	2.00	0.70	1.40	0.02
1.35	192.00	6.70	0.90	6.03	0.07
2.02	288.00	12.70	1.30	16.51	0.18
2.70	384.00	13.60	2.10	28.56	0.32
3.36	478.00	18.70	1.70	31.79	0.35
3.50	498.00	19.50	1.65	32.18	0.35
3.73	530.00	21.00	1.45	30.45	0.33

3.78	538.00	21.50	1.50	32.25	0.35
3.90	555.00	22.50	1.35	30.38	0.33
VKI: rotor 2, $V_0 = 10\text{m/s}$					
$\lambda$	$\Omega$ [rpm]	$U_{in}$ [V]	$I_{in}$ [A]	$P_{elec}$ [W]	$C_P$ [-]
0.67	136.00	2.50	1.60	4.00	0.02
1.33	271.00	8.07	2.00	16.14	0.07
1.99	405.00	12.90	2.90	37.41	0.15

### C.3 Results at UCL LEFT

UCL LEFT: rotor 1, $V_0 = 6\text{m/s}$					
$\lambda$	$\Omega$ [rpm]	$U_{in}$ [V]	$I_{in}$ [A]	$P_{elec}$ [W]	$C_P$ [-]
2.03	327.00	14.10	0.28	4.02	0.18
2.55	410.00	17.80	0.38	6.68	0.28
2.74	442.00	19.25	0.45	8.57	0.34
2.85	459.00	20.00	0.49	9.80	0.39
2.95	475.00	20.60	0.50	10.30	0.40
3.04	490.00	21.45	0.52	11.15	0.43
3.17	510.00	22.25	0.52	11.57	0.45
3.25	524.00	23.10	0.47	10.86	0.44
3.35	540.00	23.90	0.44	10.52	0.43
3.45	556.00	24.85	0.43	10.69	0.44
3.55	572.00	25.65	0.42	10.77	0.45
3.65	588.00	26.50	0.40	10.60	0.45
4.06	654.00	30.00	0.31	9.30	0.44
UCL LEFT: rotor 1, $V_0 = 8\text{m/s}$					
$\lambda$	$\Omega$ [rpm]	$U_{in}$ [V]	$I_{in}$ [A]	$P_{elec}$ [W]	$C_P$ [-]
0.52	109.00	3.30	0.37	1.22	0.03
1.04	219.00	8.40	0.45	3.78	0.07
1.56	327.00	13.50	0.51	6.88	0.12
2.03	426.00	18.50	0.64	11.91	0.20
2.60	546.00	23.10	0.90	20.88	0.34
2.81	589.00	25.00	1.05	26.25	0.43
2.91	611.00	26.00	1.11	28.81	0.46
3.02	633.00	27.00	1.11	30.05	0.49
3.11	653.00	27.90	1.11	30.91	0.50
3.22	676.00	29.00	1.04	30.30	0.49
3.33	700.00	30.10	1.02	30.85	0.51
3.64	764.00	33.40	0.94	31.56	0.53
3.83	805.00	35.30	0.88	31.17	0.53
UCL LEFT: rotor 1, $V_0 = 10\text{m/s}$					
$\lambda$	$\Omega$ [rpm]	$U_{in}$ [V]	$I_{in}$ [A]	$P_{elec}$ [W]	$C_P$ [-]
0.41	110.00	2.80	0.64	1.80	0.02
0.82	218.00	7.70	0.81	6.24	0.06
1.23	327.00	12.70	0.88	11.21	0.09

1.64	436.00	17.80	1.00	17.80	0.14
2.06	545.00	22.50	1.22	27.45	0.22
2.26	600.00	25.00	1.33	33.25	0.26
2.30	610.00	25.40	1.37	34.80	0.27
2.38	632.00	26.20	1.46	38.25	0.30
2.57	682.00	28.10	1.67	46.81	0.37
2.68	710.00	29.80	1.69	50.36	0.38
2.78	738.00	30.90	1.78	55.00	0.41
2.88	763.00	32.10	1.76	56.50	0.43
2.98	790.00	33.40	1.73	57.78	0.44
3.09	820.00	34.70	1.75	60.73	0.46
3.19	845.00	35.90	1.67	59.95	0.45
3.30	875.00	37.30	1.58	58.93	0.45
3.39	900.00	38.40	1.56	59.90	0.46
3.51	930.00	39.70	1.49	59.15	0.46
3.62	960.00	41.00	1.45	59.45	0.46
UCL LEFT: rotor 2, $V_0 = 4\text{m/s}$					
$\lambda$	$\Omega$ [rpm]	$U_{in}$ [V]	$I_{in}$ [A]	$P_{elec}$ [W]	$C_P$ [-]
1.00	81.00	2.14	0.24	0.52	0.05
1.50	122.00	4.01	0.30	1.20	0.10
2.01	163.00	5.90	0.35	2.06	0.16
2.50	203.00	7.69	0.44	3.38	0.24
3.00	244.00	9.12	0.76	6.93	0.44
3.49	284.00	11.02	0.80	8.82	0.55
4.00	325.00	13.03	0.70	9.12	0.57
4.25	345.00	14.10	0.65	9.17	0.58
4.50	366.00	15.20	0.58	8.82	0.57
5.00	406.00	17.38	0.48	8.34	0.56
5.50	447.00	19.59	0.36	7.05	0.51
5.99	487.00	21.90	0.27	5.91	0.47
UCL LEFT: rotor 2, $V_0 = 5.5\text{m/s}$					
$\lambda$	$\Omega$ [rpm]	$U_{in}$ [V]	$I_{in}$ [A]	$P_{elec}$ [W]	$C_P$ [-]
1.02	112.00	3.00	0.56	1.68	0.05
1.52	167.00	5.47	0.68	3.72	0.10
2.02	223.00	7.90	0.82	6.48	0.17
2.53	279.00	10.00	1.15	11.50	0.29
3.04	335.00	11.80	1.71	20.18	0.50
3.54	390.00	14.80	1.45	21.46	0.51
4.06	447.00	17.80	1.27	22.61	0.53
4.56	502.00	20.80	1.10	22.88	0.54
5.07	558.00	23.80	0.90	21.42	0.52
5.56	613.00	26.80	0.80	21.44	0.53
6.08	670.00	29.80	0.60	17.88	0.47
6.59	726.00	33.00	0.42	13.86	0.41
UCL LEFT: rotor 2, $V_0 = 7\text{m/s}$					
$\lambda$	$\Omega$ [rpm]	$U_{in}$ [V]	$I_{in}$ [A]	$P_{elec}$ [W]	$C_P$ [-]
0.52	71.00	0.85	0.76	0.64	0.02
1.04	142.00	3.93	0.92	3.62	0.06
1.56	213.00	7.00	1.10	7.70	0.11

2.08	284.50	10.00	1.31	13.10	0.17
2.61	356.00	12.20	2.06	25.13	0.33
3.12	426.00	14.25	2.72	38.76	0.52
3.64	498.00	17.85	2.42	43.20	0.55
4.16	569.00	21.70	2.09	45.35	0.56
4.68	640.00	25.30	1.83	46.30	0.57
5.20	711.00	29.10	1.58	45.98	0.56
5.72	782.00	33.00	1.34	44.22	0.55
6.24	853.00	36.80	1.15	42.32	0.54
UCL LEFT: rotor 2, $V_0 = 10\text{m/s}$					
$\lambda$	$\Omega$ [rpm]	$U_{in}$ [V]	$I_{in}$ [A]	$P_{elec}$ [W]	$C_P$ [-]
0.69	136.00	2.14	1.70	3.64	0.03
1.39	273.00	7.49	2.30	17.23	0.09
2.09	409.00	12.40	3.04	37.70	0.18
2.23	436.00	13.00	3.34	43.42	0.21

## C.4 Wind speed measurements

UCL LEFT: rotor 1, $V_{init}$ m/s		
<b>Diagonal 1</b>	<b>Diagonal 2</b>	<b>Diagonal 3</b>
2.27	2.65	2.73
2.72	3	2.84
2.68	2.69	2.97
3	2.95	3.05
2.9	3.05	3.2
2.45	2.6	2.95
UCL LEFT: rotor 1, $V_0 \approx 6\text{m/s}$		
<b>Diagonal 1</b>	<b>Diagonal 2</b>	<b>Diagonal 3</b>
5.1	5.7	5.5
5.9	6.6	6.1
5.8	6.1	5.7
6.6	5.95	6.3
6.3	5.75	6.3
5.15	5	5.5
UCL LEFT: rotor 1, $V_0 \approx 8\text{m/s}$		
<b>Diagonal 1</b>	<b>Diagonal 2</b>	<b>Diagonal 3</b>
6.3	6.85	7.7
7.65	7.95	8.15
7.95	7.7	7.75
8.05	7.75	8.35
7.95	8.2	8.1
6.55	7.1	7.25
UCL LEFT: rotor 1, $V_0 \approx 10\text{m/s}$		
<b>Diagonal 1</b>	<b>Diagonal 2</b>	<b>Diagonal 3</b>
8.55	8.7	9.25

9.7	9.4	10.15
9.95	9.6	9.85
10.4	9.7	10.2
10.35	10.1	10.6
8.95	8.7	9.3
UCL LEFT: rotor 2, $V_{init}$ m/s		
<b>Diagonal 1</b>	<b>Diagonal 2</b>	<b>Diagonal 3</b>
2.15	2	2
2.3	2.15	2.3
2.15	2.25	2.05
2.36	2.1	2.24
2.22	2.25	2.44
1.75	1.9	2.02
UCL LEFT: rotor 2, $V_0 \approx 4\text{m/s}$		
<b>Diagonal 1</b>	<b>Diagonal 2</b>	<b>Diagonal 3</b>
3.21	3.47	3.67
3.72	3.82	4.27
3.68	3.55	3.87
4.19	4.03	3.72
4.2	4.33	4.28
3.92	3.43	3.55
UCL LEFT: rotor 2, $V_0 \approx 5.5\text{m/s}$		
<b>Diagonal 1</b>	<b>Diagonal 2</b>	<b>Diagonal 3</b>
4.9	5.25	5.05
5.75	5.75	5.65
5.55	5.3	5.35
5.8	5.4	6
5.15	5.65	6.05
4.7	4.8	5.5
UCL LEFT: rotor 2, $V_0 \approx 7\text{m/s}$		
<b>Diagonal 1</b>	<b>Diagonal 2</b>	<b>Diagonal 3</b>
6.6	6.15	6.9
7.3	7.3	7.1
6.6	7.15	6.3
6.65	6.65	6.4
6.85	6.5	7.25
6.3	6.35	6.7
UCL LEFT: rotor 2, $V_0 \approx 10\text{m/s}$		
<b>Diagonal 1</b>	<b>Diagonal 2</b>	<b>Diagonal 3</b>
8.55	8.7	9.25
9.7	9.4	10.15
9.95	9.6	9.85
10.4	9.7	10.2
10.35	10.1	10.6
8.95	8.7	9.3

